FATIGUE BEHAVIOR OF COPPER ZINC ALUMINUM SHAPE MEMORY ALLOYS

by

Ameendraraj Subramaniam

A Thesis
Submitted to the Faculty of Graduate Studies
in Partial Fulfillment for the Degree of

MASTER OF SCIENCE

Department of Civil Engineering
University of Manitoba
Winnipeg, Manitoba

FATIGUE BEHAVIOR OF COPPER ZINC ALUMINUM SHAPE MEMORY ALLOYS

BY

AMEENDRARAJ SUBRAMANIAM

A Thesis submitted to the Faculty of Graduate Studies of the University of Manitoba in partial fulfillment of the requirements of the degree of

MASTER OF SCIENCE

Abstract

Copper Zinc Aluminum (CuZnAl) shape memory alloys (SMA) are receiving wide attention in recent years due to applications in smart (adaptive) structures. A stress-induced phase transition occurs in SMAs that causes inelastic deformation and gives rise to an energy-absorbing capacity. Due to this inelastic deformation associated with SMA, CuZnAl shape memory alloys should be capable of having high fatigue lives. The energy-absorbing capacity and possible high fatigue lives makes CuZnAl a promising material in the elimination of vibration induced fatigue failures in structures. In order to use CuZnAl in structural applications, a thorough study of its mechanical properties is required. In this thesis, the mechanical and fatigue properties of both austenitic ($M_s = -7.3°C$) and martensitic ($M_s = 42°C$) CuZnAl have been studied at room temperature through a mechanical testing program. The energy-absorbing capacity of superelastic, austenitic CuZnAl is also measured.

Tensile, strain cycling, and low- and high-cycle fatigue tests were conducted at room temperature on austenitic and martensitic CuZnAl alloys. The mechanical properties obtained include the Young's modulus, ultimate stress and ultimate strain. The strain cycling tests were conducted to study the superelastic behavior of austenitic CuZnAl and to quantify the associated energy-absorbing capacity. The energy dissipation associated with superelastic CuZnAl alloy was quantified by measuring the area enclosed within the hysteresis curves obtained from the strain cycling tests. The CuZnAl alloys were subjected to fully reversed, cyclic, strain controlled low-cycle fatigue (LCF) tests. The fatigue life of the CuZnAl alloys were determined in terms of total strain and plastic strain. LCF test data showed that the Coffin-Manson law and Basquin relationships are obeyed. The tests indicate that the behavior of CuZnAl in the low-cycle fatigue regime is comparable to that of steel within the strain range studied. The energy dissipation due to plastic deformation was quantified by measuring the area within the LCF test hysteresis curves. Stress controlled, fully reversed, axial, high-cycle fatigue (HCF) tests were conducted for the first time on CuZnAl. Stress-Life (S-N) curves for the CuZnAl alloys were obtained from the HCF test data. The martensitic CuZnAl alloy showed better HCF properties than the austenitic

CuZnAl. The fatigue strength of austenitic and martensitic CuZnAl at $N = 10^6$ were determined to be 153 and 167 MPa respectively. In the high-cycle fatigue regime the CuZnAl alloys show poor fatigue properties compared to steel and aluminum.

In conclusion, a comparative testing program involving CuZnAl and commonly used metals are recommended. Further studies should be carried out in the area of fatigue and damping of CuZnAl embedded composites to quantify the behavior of such systems. Any further tests on CuZnAl should be conducted using ASTM recommended standard diameter specimens to avoid the problems associated with testing small diameter specimens.

Acknowledgements

I would like to thank Manitoba Hydro for the financial assistance granted to conduct this project. This study would not have been possible without the help of the following individuals whom I would like to acknowledge.

Dr. N. Rajapakse, my advisor, for initiating this project, his constant encouragement, advice, continuous guidance and support throughout the course of the project.

Dr. D. Polyzois for initiating this project and for his helpful advice throughout the course of this thesis and for being on the examining committee.

Mr. Ben Yue, of the Transmission and Civil Department of Manitoba Hydro, for being Manitoba Hydro's representative for this project.

Dr. M. Chaturvedi, of the Mechanical and Industrial engineering department at the University of Manitoba, for allowing me to use the facilities in the Metallurgical and Materials laboratory to conduct all the experiments.

Dr. R. Jayaraman, of the Mechanical and Industrial engineering department at the University of Manitoba, for being on the examining committee.

Mr. Don Mardis and Mr. Jon Van Dorp, of the Metallurgical and Materials laboratory at the University of Manitoba, for their invaluable technical assistance in all phases of the mechanical testing program.

Mr. Irwin Penner, of the Mechanical engineering department at the University of Manitoba, for machining all the test specimens.

Mr. Scott Sparrow and Mr. Moray McVey, of the Structures laboratory at the University of Manitoba, for their technical assistance.

I would like to thank my parents for their continuous support and encouragement throughout the course of my education, and my brothers and sister for their patience, encouragement and understanding during this thesis. I would like to extend my gratitude to my fiance, Sareli, for her understanding, encouragement, help and patience, which was instrumental in completing my graduate studies.

Table of Contents

List of Tables

List of Figures

List of Symbols

A_f	Austenite finish temperature
A_s	Austenite start temperature
b	Fatigue strength exponent
β	Beta or parent phase of the alloy (austenitic)
c	Fatigue ductility exponent
CuZnAl	Copper Zinc Aluminum
D	Specific damping capacity of a material
D_s	Specific damping capacity of a member or specimen
DSC	Differential scanning calorimetry
$\Delta\varepsilon_e$	Elastic strain range
$\frac{\Delta\varepsilon_e}{2}$	Elastic strain amplitude
$\frac{\Delta\varepsilon_p}{2}$	Plastic strain amplitude
$\left(\frac{\Delta\varepsilon_p}{2}\right)_{0.5N_f}$	Plastic strain amplitude at half life
$\Delta\varepsilon_t$	Total strain range
$\frac{\Delta\varepsilon_t}{2}$	Total strain amplitude
$\Delta\sigma$	Stress range, $(\sigma_{max} + \lvert\sigma_{min}\rvert)$

$\left(\frac{\Delta\sigma}{2}\right)_{0.5N_f}$	Cyclic stress at half life
E	Young's Modulus
e_f	Ultimate strain
$\dot{\varepsilon}$	Strain rate, s^{-1}
ε_a	Cyclic strain amplitude / total axial strain amplitude
ε_f	True strain at fracture
ε_f'	Fatigue ductility coefficient
ε_{max}	Tensile peak total strain
ε_{min}	Compressive peak total strain
HCF	High-cycle fatigue
$H\Delta\varepsilon_t/2$	Degree of cyclic hardening at a particular strain amplitude
K'	Cyclic strength coefficient
LCF	Low-cycle fatigue
M_f	Martensite finish temperature
M_s	Martensite start temperature
N_f	Number of cycles to failure
NiTi	Nickel titanium
n'	Cyclic work hardening exponent
η	Loss-coefficient for a material

η_s	Loss-coefficient for a specimen or member
SIM	Stress-induced martensite
SMA	Shape memory alloys
SME	Shape memory effect
S_u	Ultimate tensile strength
S_{ys}	Yield strength
σ_a	Stress amplitude
σ_f	True fracture strength
σ_f'	Fatigue strength coefficient
σ_{max}	Tensile peak stress
σ_{min}	Compressive peak stress
σ^{M-P}	Stress at which reversion of martensite to austenite occurs
σ^{P-M}	Stress to induce martensite
TMD	Tuned mass dampers
U	Unit strain energy of a material
U_s	Unit strain energy of a specimen or member

1 Introduction

1.1 General

Fatigue and vibration failures continue to plague civil engineering structures. Transmission lines and supporting towers are exposed to wind and develop sustained motions. These sustained motions cause costly damage to conductors and other mechanical and structural subsystems. Wind induced vibrations of tower members have caused the fatigue failure of connecting members (Goel, 1994).

Many structural components in engineered structures are subjected to static and dynamic loading. Static loads, in the form of dead loads, are relatively harmless to a structure as they are anticipated and can be taken into consideration in the design. Dynamic loads, in the form of wind induced vibrations or in the form of earthquakes, are the more critical type of loads experienced by structures. The variability of naturally occurring dynamic loads are critical because their severity is unpredictable. In the construction industry, steel is the material of choice in building structures such as transmission towers. These structures have stood and continue to stand and serve their function rather well. However, over time, with continued exposure to dynamic loading (particularly wind), fatigue sets in and a member of the structure fails. Failure of the single member eventually leads to the failure of the entire structure. Fatigue failure of structures are expensive and dangerous. In terms of service life, steel subjected to cyclic loading fails in fatigue after a certain number of cycles.

A new class of materials known as Shape Memory Alloys (SMA) have been developed to have a very high damping capacity and favorable fatigue properties when compared to conventional metals and alloys. SMA through their unusual mechanical properties can sustain over 15% "elastic" strain (Pops, 1970). These large reversible deformations occur as a result of reversible transformations that occur within the crystal structure of these alloys when unloaded. In principle, these alloys should be capable of repeated

deformation to large strains, resulting in infinite fatigue lives. Employing SMA in structures could possibly reduce fatigue and vibration related problems in structures thereby increasing the service life of these structures.

Owing to the unique properties associated with the shape recovery effect and the material phase changes, shape memory alloys have been exploited in actuator and sensor applications. Shape memory alloy hybrid composite materials have demonstrated varying success in applications such as vibration and shape control, creep resistance in structures and strain sensing (Paine and Rogers, 1994a). By embedding shape memory alloys in composites, the impact damage resistance of the composites have been improved by making use of the superelastic characteristics of shape memory alloys (Paine and Rogers, 1994b). Shape memory alloys have also been exploited for their inherent damping properties which are several times higher than steel (Paine and Rogers, 1994a). The most common means of vibration control in tall structures are by employing tuned mass dampers (TMDs) and tendon control. It has been successfully shown that employing shape memory alloy wires in tendon control in a cantilevered beam can reduce vibrations by 3 orders of magnitude (Shahin et al., 1994).

Shape memory alloys are also receiving wide attention in aerospace engineering applications. For example, the interest in establishing space stations come with its problems: difficulty of assembling the space structure and vibration induced from manned activities and docking of space vehicles. Studies are underway to employ the shape memory effect of shape memory alloys in creating connectors to ensure that minimum time and effort is required in assembly of space structures. It has also been suggested to use the high damping capacity of shape memory alloys to damp out the vibrations in space structures (Schetky, 1990). Structures in earthquake prone areas are protected from the damaging vibrations of earthquakes by base isolation. Base isolation involves uncoupling the building from the horizontal vibrations while simultaneously supporting the weight of the structure (Jalihal et al., 1994). Dampers are used to absorb the energy (horizontal vibrations) during the earthquake. The problem with base isolation is that it is passive in nature. By being passive the amount of damping available in case of an earthquake is fixed. However, base isolation can be made active by using shape memory alloys as the damper. By

being active the amount of damping made available at a given time can be controlled. As a result, if designed properly, the damping mechanism can ensure that the strength or deformation capacity of the structure will not be surpassed by earthquake induced vibrations. In this application the shape memory alloy shows its versatility by serving as a controller as well as a material with a high damping capacity.

1.2 Shape Memory Alloys

Shape memory alloys (SMA) are a family of metallic alloys with the remarkable ability to switch from one cystallographic structure to another through a change in temperature or applied stress. This change enables the alloy to assume a particular shape at one temperature (or stress level) and a different shape at another temperature (or stress level). The two crystallographic structures attainable by shape memory alloys are the low temperature/high stress martensite phase and the high temperature/low stress austenite phase. The austenitic phase is also referred to as the beta (β) or parent phase of the alloy. The temperatures, at which the transformation from one phase to the other occur, are referred to as transformation temperatures. SMA by their nature have properties that are of interest to engineers and scientists. They are the shape memory effect (SME) and superelasticity (or pseudoelasticity). Alloys exhibiting SME and superelasticity also possess high damping capacity which is related to these effects.

The shape memory effect had been noted as early as 1938, when Alden B. Greninger of Havard University and V.G. Mooradian of the Massachusettes Institute of Technology showed that the martensite phase in brass (an alloy of copper and zinc) could be made to form and disappear with a change in temperature. At about the same time G.V. Kurdyumov, a Russian metallurgist, studied the phase relations in brass between the high temperature β phase and the martensite formed by rapid cooling. Later Thomas A. Read and his associates at the University of Illinois investigated the shape memory effect in gold-cadmium alloys and demonstrated the forces that could be developed by phase transitions. It was in 1962 that the phenomenon came to worldwide attention with the announcement of shape memory in an alloy of nickel and titanium. In the seventies, a family of SMA was developed based on copper, zinc and aluminum (Schetky, 1979). In the follow-

ing years the shape memory effect has been observed in many binary and ternary alloy systems. These include AgCd, AuCd, CuAlNi, CuAuZn, CuSn, CuZn, CuZnAl, CuZnGa, CuZnSi, CuZnSn, InTl, NiAl, FePt, FePd, MnCu and NiTi. Of these, only NiTi, CuZnAl and CuAlNi have gained wide acceptance in applications due to their better mechanical properties. However, NiTi is by far the most widely used. CuZnAl has not enjoyed the same success as NiTi due to insufficient experimental work. This may have been because initial studies indicated that CuZnAl had weak fatigue properties.

However, CuZnAl is an attractive SMA for engineering applications compared to other SMA for two reasons. CuZnAl is cheaper and easier to machine than most other SMA. It is widely agreed that NiTi has better fatigue and strength properties than CuZnAl, however NiTi costs about $150/lb which makes it six times more expensive than CuZnAl (Graesser et al., 1991). CuZnAl is easily machined whereas NiTi is extremely hard and abrasive in machining operations thus requiring tools not commonly employed in machine shops. Of all SMA, CuZnAl also has the highest damping capacity. The use of CuZnAl in engineering applications requires extensive experimental investigation of its mechanical properties under a variety of conditions.

The uniqueness of shape memory alloys lies in their ability to switch from one crystalline structure to another by a diffusionless transformation. The interchangeable crystalline forms are austenite and martensite. The reason the alloy attains a particular phase at a given temperature is because the alloy continuously tries to attain thermodynamic equilibrium. As such, the alloy tries to attain the phase which makes it thermodynamically stable at a given temperature. Each shape memory alloy has four inherent temperatures indicating the temperature when a particular phase begins to form and finishes. These are known as the transformation temperatures. These transformation temperatures (see Figure 1.1) are M_f - martensite finish, M_s - martensite start, A_f - austenite finish and A_s - austenite start temperatures ($M_f < M_s < A_s < A_f$). The current phase of the alloy is determined by the temperature of the alloy in relation to its transformation temperatures. The transformation temperatures depend on the composition of the alloy.

A typical transformation curve is shown in Fig. 1.1 with the martensite fraction

plotted against the temperature. If a SMA alloy specimen is heated above its A_f temperature, it exists completely in its austenitic phase. Upon cooling below the M_s temperature of the alloy, the austenite gradually begins to transform into martensite. The transformation completes only after cooling below the M_f temperature. Until cooling occurs below M_f, some fraction of austenite will remain in the sample as shown in Figure 1.1. The transformation from austenite to martensite is referred to as the forward transformation.

If the alloy, in its martensitic phase, is heated from a temperature below its M_f temperature, the martensite begins to transform into austenite at the A_s temperature. The transformation is complete when the alloy is heated to a temperature above its A_f temperature. This transformation from martensite to austenite is referred to as the reverse transformation. During the heating process, at a temperature between the A_s and A_f temperatures, some fraction of martensite is retained in the sample.

There are several means of measuring the transformation temperatures of SMA alloys. The two most common methods of measuring the transformation temperatures are by electrical resistivity and differential scanning calorimetry (DSC) measurements. The transformation temperatures exhibited by shape memory alloys are highly dependent on their composition. Little change in their composition will result in large changes in their transformation temperatures. Figure 1.2 shows the M_s temperatures as a function of the composition of CuZnAl shape memory alloys. The advantage of being able to change the transformation temperature by changing the composition is that the material can be tailored to attain the desired phase at the application temperature. The different phases possess different properties. For example, in general, shape memory alloys in the martensitic phase are much softer than the austenitic phase whereas the martensitic phase has higher damping properties than the austenitic phase.

1.3 The Shape Memory Effect

In a simple example of the shape memory effect, a wire of shape memory alloy is

bent at room temperature in the form of a clover leaf (Schetky, 1979). Then the wire is heated until its crystal structure assumes the high-temperature configuration called the beta or parent phase (austenitic phase). Next the wire is rapidly cooled so that the atoms in the metal rearrange themselves into the crystal form of martensite (martensitic phase). One can now bend or twist the wire into any other form. It must be noted that in order to achieve 100 percent recovery of shape the deformation of the wire must be limited to an internal strain of between 3 and 9 percent, depending on the alloy the wire is made of. If the wire is later heated to a temperature above that at which the martensite reverts to the parent phase, there is an orderly shift of large groups of atoms which in turn restores the original maple leaf form.

A schematic showing the crystallographic processes which occur to give rise to the shape memory effect is shown in Figure 1.3. The SMA specimen in the austenitic phase, when cooled to a sufficiently low temperature, transforms into martensite. This form of martensite is known as twinned martensite because of the zigzag pattern the atoms assume. Even though a complete transformation has occurred the specimen does not experience any shape change. This is because the twinned martensite occupies whatever space was previously occupied by austenite. For this reason the martensite formed is referred to as self-accommodating martensite (Funakubo, 1984). When an external force is applied to the sample in the twinned martensite phase, the atoms shift into another form of martensite which is referred to as deformed martensite and the sample assumes a deformed shape. The deformed martensite begins to forms as it has a favorable disposition to the applied stress. Upon heating the alloy above its A_f temperature, an orderly shifting of atoms occur and the austenitic phase is attained. By this transformation into austenite the strain that was existing in the deformed martensite is completely recovered and the specimen attains its original shape.

The shape memory effect described above is a temperature driven effect. In the shape memory effect, if the recovery of shape is restrained, a proportional force is produced. The generated force can be used to do work or to grip another object. Alloys exhibiting the shape memory effect are employed in many applications in fields such as medicine and aerospace.

An example of an application in aerospace was the development of SMA couplings for hydraulic-fluid lines in the F-14 jet fighter built by the Grumman Aerospace Corporation. The task at hand was to find a method to join hydraulic lines that were exposed to very cold temperatures (Schetky, 1979). In these applications a TiNiFe alloy with a transformation temperature of $-150°C$ was fabricated as a tube featuring an inner diameter, which was 4% smaller than the nominal outer diameter of the pipe which had to be joined. During the joining process the coupling was maintained at a low temperature by using liquid nitrogen. A tapered plug of suitable dimensions was then forced into the coupling in order to increase the diameter of the coupling by approximately 8%. The two pipes to be joined were then inserted at the two ends of the coupling. As the coupling's temperature rose to the room temperature it had a tendency to shrink in order to return to its inner diameter, in this case, to the dimension before the forced expansion. The ends of the two pipes are therefore held together simply, in service, with a high level of reliability. Thousands of such couplings have been employed in nuclear submarines, warships, and pipes on the ocean floor. The couplings are employed without leaking or reliability problems (Gandhi and Thompson, 1992).

The advantages of using these couplings are that they can be employed to temperatures as low as the transformation temperature of the alloy. By choosing an alloy that has a martensite transformation temperature in the cryogenic region, the coupling can be employed in very cold environments as in the case of the hydraulic fluid lines close to the exterior skin of the F-14 fighter jet. In contrast to welding, high temperatures are not involved in the assembly process. Therefore, there is minimal temperature-induced damage to the surrounding parts.

1.4 Superelasticity in Shape Memory Alloys

A stress driven effect known as superelasticity is the phenomenon of interest in this study. Superelasticity in SMA is a phenomenon whereby large strains induced by loading a SMA specimen are recovered by unloading the SMA specimen. Superelasticity (or pseudoelasticity) occurs in SMA by two mechanisms. The first is a result of reversible martensite formation upon loading a specimen in its parent phase and its reversion back to the

parent phase upon unloading. This mechanism is further explained in section 1.4.1. Superelasticity also occurs by reorientation of the martensite crystal structure, of a SMA alloy in its martensitic phase, when it is loaded and then achieving its original orientation when unloaded. This phenomenon is explained in more detail in section 1.4.2. Through both these mechanisms, large strains are recoverable.

1.4.1 Superelasticity by Reversible Martensite Formation

Superelasticity by reversible martensite transformation occurs in SMA in the austenitic phase in which martensite formed during loading becomes unstable upon unloading. In this case, the transformation strain obtained during loading is recovered on unloading when the martensite formed during loading reverts back to the parent (austenitic) phase. The term stress induced martensite (SIM) is used to refer to the martensite formed during loading. Superelasticity by reversible martensite formation will be better explained below in the context of a tension test involving a tensile test specimen made of a SMA (Krishnan et al., 1974).

A tensile specimen made of a SMA was tested at a constant temperature, T_1, slightly above its A_f temperature but below a critical temperature, T_c. This critical temperature is important because above this temperature, slip occurs at the microstructure level and superelasticity is not realized in the SMA. At temperature T_1, the sample is in the austenitic phase. Also, at this temperature, martensite can be subjected to a stress induced transformation. On stressing the specimen in a test frame, a stress-strain curve, as shown in Figure 1.4, is obtained. As a specimen is loaded it will deform elastically up to a certain stress level, $\sigma_{T_1}^{P-M}$, denoted by point B. The section AB represents purely elastic deformation of the parent phase. At the stress level $\sigma_{T_1}^{P-M}$, the first martensite plates begin to appear. They appear as a result of a transformation of the austenite crystals into martensite crystals with the application of stress (stress induced martensite). With continued application of stress the specimen continues to elongate with no apparent increase in stress level. Hence the specimen will seem to yield plastically (segment BC). This is not yielding

as in the conventional sense. What is happening is that more martensite crystals continue to form at this stress level. The stress level is referred to as the stress required to induce martensite transformation at temperature T_1 ($\sigma_{T_1}^{P-M}$). At point C, the transformation of austenite to martensite is complete. If the loading is continued beyond point C, the martensite crystals will deform plastically as shown by segment CD of the curve. At point D, the plastic yield stress, σ_y^M, of the martensite is reached and further loading will lead to fracture. However, if the specimen is unloaded at point C', before yielding of the martensite crystals occur, the martensite crystals will revert back to austenite and the specimen will recover the strain, thereby contracting to its original dimension. The strain recovery occurs in three stages. Stage $C'F$ represents elastic unloading of the martensite crystals. Reverse martensitic transformation begins at point F where the stress level, $\sigma_{T_1}^{M-P}$, is reached. The martensite crystals continue to revert to austenite up to point G. It is interesting to note that the first martensite crystals to form are the last to revert back to austenite. Finally, the segment GH represents the elastic unloading of the austenite crystals. The strain represented by segment AH is the residual strain. Usually no residual strain results. However if any plastic deformation occurs during loading or unloading a residual strain will result.

Accompanying the transformation from austenite to martensite is the dissipation of heat. A portion of the strain energy is dissipated in the form of heat resulting in a large hysteresis, depending on the shape memory alloy investigated, between the loading and unloading curves. The area enclosed by the stress-strain curve is a measure of the energy dissipated per cycle. This energy dissipation per loading-unloading cycle can be used to damp out vibrations. The frequency of loading and unloading has to be at a rate sufficient to allow the material to dissipate all the heat generated per cycle. If the rate of loading does not allow the material to dissipate heat at the required rate, there will be a buildup of heat. This heat will prevent the material from forming stress-induced martensite in subsequent loading cycles, leading to a degradation of the superelastic property.

1.4.2 Superelasticity by Martensite Reorientation

The superelastic property also occurs in SMA in the martensitic phase. In SMA alloys loaded at a temperature below its M_f temperature, the original martensitic crystal structure rearranges itself to accommodate the resulting strain without causing any permanent deformation to the crystal structure. Upon unloading, there is a rearrangement of the martensite plates to the original structural configuration. In this case, the strain obtained during loading is recovered on unloading when the new martensitic structure rearranges itself to attain the original martensitic structure of the alloy. A stress-strain curve similar to that shown in Figure 1.4 is obtained on loading and unloading a tensile specimen of a SMA alloy which is in its martensitic phase. However, the segments of the stress-strain curve represent different phenomena compared to the superelasticity by stress induced martensite.

The segment AB of the stress-strain curve in Figure 1.4 represents the elastic loading of the martensite crystals. The stress level at point B represents the stress necessary to initiate reorientation of the martensite crystals into another form of martensite. This reorientation of the martensite is responsible for the accommodation of the increased strain. Segment BC represents the continued reorientation of the martensite crystals with the application of stress. Once again loading beyond point C will lead to the elastic deformation of the martensite crystals with the new orientation. Loading beyond point D will cause plastic yielding of the martensite with the new orientation. However, if the specimen is once again unloaded at point C', the martensite reverts to its original orientation and the strain is recovered. Segment $C'F$ represents the elastic unloading of the newly oriented martensite. At the stress level represented by point F the martensite crystals begin to revert to their original orientation. This process continues up to point G, at which all the martensite have assumed their original orientation. Once again segment GH represents the elastic unloading of the martensite with the original orientation.

As with superelasticity by SIM, superelasticity by martensite reorientation results in a stress-strain curve with hysteresis. The space enclosed by the loading and unloading curves are representative of the energy dissipated.

1.5 Martensitic Transformations in Ferrous Alloys

The shape memory effect and pseudoelasticity occur in materials that experience thermoelastic martensitic transformations. Ferrous alloys are capable of martensitic transformations, but not thermoelastic martensitic transformations. As a result, ferrous alloys do not exhibit the shape memory effect or pseudoelasticity by SIM. A difference between SMA and ferrous alloys is in the degree of supercooling required for martensitic transformations. The degree of supercooling in martensitic transformations in ferrous alloys can be as much as $200°C$, but in SMA it is only $5 - 30°C$ (Funakubo, 1984).

In steels, the high temperature austenitic phase is softer than the low temperature martensitic phase. As a result, steels is used in the martensitic phase. The martensitic transformation is the cornerstone of the heat treatment and tempering processes applied to ferrous alloys to arrive at structural materials with desired properties such as high strength and ductility. In the heat treatment process, the steel is heated to temperatures above A_f to convert the microstructure to the high-temperature austenitic phase. Immediate quenching to temperatures below the M_f assures that all the austenite reverts to the high strength martensite. After quenching, steel will generally harden due to the newly formed martensitic microstructure. Further heat treatment applications are available to ensure that the structural component has the desired final properties.

The martensitic transformations occurring in ferrous alloys are accompanied by fairly large (about 4%) volume changes, and there is a plastic deformation in the parent phase. Hence, the interface energy and the energy needed for plastic deformation are not small enough to be neglected and consequently thermoelastic martensitic transformations do not occur in ferrous alloys.

1.6 Literature Review

The literature review concentrates on studies involving mechanical and fatigue behavior of CuZnAl alloys. There are numerous studies on the mechanical and fatigue properties of NiTi and CuAlNi (Melton et al., 1979a, Sakamoto et al., 1982). There are also numerous studies focussing on theoretical modelling of shape memory alloy behavior (Dye, 1990, Barrett, 1995, Ford et al., 1996). A summary of the existing work on the mechanical and fatigue behavior of CuZnAl is given below.

CuZnAl was first investigated in a study by Pops et al. (Pops & Ridley, 1970) to see if pseudoelasticity could be developed in alloy systems based on the CuZn β phase including CuZnAl. Tensile samples were deformed at temperatures between the M_s temperature and ambient. Elastic behavior was observed at low stress levels and it was found that plastic flow does not occur at the point of deviation from linearity in the stress-strain curves. It was observed that when the tensile sample was unloaded beyond the point of linearity, the stress dropped quite rapidly producing a hysteresis loop. Strains were predominantly elastic, since the sample returned to almost its original shape. Elastic strains larger than 6 percent were measured in some specimens. The stress where deviation from linearity on the stress-strain curve occurs was shown to correspond to the onset of martensitic transformation and was found to vary with the test temperature. It was concluded that superelasticity should be possible in other systems based upon the CuZn β – phase.

Delaey et al. (1978) studied the fatigue properties of pseudoelastic and martensitic CuZnAl alloys. Flat specimens having gauge dimensions of 33 mm x 6 mm x 1 mm were tested in pulsating tension from zero stress to a maximum stress designated $2\sigma_a$. The $2\sigma_a$-N_f curves were shown to follow a Basquin type of relation. The martensitic alloy was shown to have better fatigue properties than the pseudoelastic (austenitic) alloy in the range above $N_f = 10^2$. Electron microscopic examinations of the pseudoelastic samples revealed that dislocation and twinning of the microstructure were involved in the cycle deformation mechanism. It was concluded that this dislocation and twinning of the micro-

structure introduces local stress concentrations and may render the material more prone to failure.

Melton and Mercier (1979b) studied the effect of martensite start temperature, M_s, on the fatigue life of CuZnAl alloys and compared their behavior with that of NiTi. Round hour-glass fatigue specimens with a central diameter of 3 mm were subject to rotating bending fatigue tests at room temperature at a frequency of 46 Hz. Tests were carried out on CuZnAl alloys having M_s temperatures of +47, -10, -57 and $-118°C$. The stress for fracture in around 10^5 cycles was found to be very low, less than 30 MPa. The martensitic alloy showed the longest fatigue life for a given stress while the austenitic alloy ($M_s = -10°C$) showed the most pseudoelastic strain and also the poorest fatigue properties. Results indicate that there is a decrease in the number of cycles to failure for a given stress as M_s is decreased for CuZnAl alloys. This behavior is the reverse of the behavior found for NiTi. It was concluded that CuZnAl shows better fatigue properties in the martensitic condition whereas pseudoelastic deformation leads to earlier cracking at the grain boundaries (intergranular cracking). Intergranular cracking results from strain incompatibilities across the grain boundaries.

Janssen et al. (1979) performed load controlled fatigue tests on β (austenitic) and martensitic CuZnAl alloys of different composition and treatments. The samples were subjected to sinusoidal loading from zero stress to σ_M in a frequency range from 1 to 10 Hz. It was shown that in β and martensitic CuZnAl alloys, high reversible strains are obtained due to reorientation or reversion of the thermoelastic martensite. However, during fatigue testing at constant stress levels, initially rapid strain hardening occurred, even in the fine grained alloys with a well developed texture. This indicates that during martensite reorientation or reversion, some structural damage occurs which leads to residual deformation. This damage is as a result of dislocations, fine twins, intersecting martensite plates and retained martensite for both martensite and austenite samples of CuZnAl. A CuZnAl alloy with an austenitic structure was shown to have an ultimate tensile strength of 900 MPa and a reversible strain of 0.6% after 10^6 cycles at a constant stress level. The

same alloy was cycled successfully between zero stress and a stress level of σ_M = 425 MPa to 10^6 cycles without failure. These remarkable properties of this particular specimen were attributed not only to the strengthening provided by the presence of Al_2O_3 particles, but the grain size refinement and well developed texture. It was concluded that grain size and texture influence strength and fatigue life in austenitic and martensitic CuZnAl alloys.

A thorough review of the existing literature revealed that there has been only little attention focussed on the experimental investigation of CuZnAl compared to NiTi shape memory alloy. The preceding studies show that axial fatigue experiments of CuZnAl were conducted only in tension because small diameter samples were used in the test programs. In practice, stress reversal is encountered and therefore data from reversed axial fatigue tests of CuZnAl is important. In all of the past studies, only small samples were used in the test programs. The influence of small samples on test results cannot be neglected. Quality control on smaller samples is easier and this ensures good mechanical properties. However, with larger sample the quality control is harder to achieve and thus the mechanical properties tend to be lower in the larger samples. In civil engineering applications, large sized materials are used and therefore tests must be performed on larger samples to obtain accurate measures of their mechanical properties. Martensitic CuZnAl is attributed as having better fatigue properties than austenitic CuZnAl. The poor fatigue properties of austenitic CuZnAl has been attributed to the pseudoelastic deformation, which leads to intergranular cracking. The fatigue behavior of austenitic CuZnAl alloy can be improved by grain size refinement and strengthening by the addition of other compounds.

1.7 Objective and Scope of the Present Research

Vibration problems experienced by structures may be alleviated through the use of advanced materials with good damping properties. CuZnAl is a member of a family of alloys known as shape memory alloys (SMA), reported to have a high damping capacity. CuZnAl has the potential to be exploited in a variety of applications which require high damping properties. To be used as a damping material by itself or in a hybrid composite

material, the mechanical and fatigue behavior of CuZnAl is essential. However, experimental data on the mechanical and fatigue behavior of CuZnAl is lacking and insufficient. Existing data come from tests carried out on small samples which have not been subjected to stress reversal. Availability of experimental data on quantifying the working stresses and fatigue behavior of CuZnAl is an important step towards its use in a variety of applications. The aim of this thesis was to increase the mechanical property database of CuZnAl alloy through a comprehensive experimental program involving relatively large size specimens. The experiments conducted included tension tests, strain cycling tests, low- and high-cycle fatigue tests. The mechanical properties investigated include the ultimate strength, Young's modulus, ultimate strain and the fatigue behavior of CuZnAl alloys. In addition, the damping capacity of CuZnAl due to superelasticity and plastic deformation were quantified.

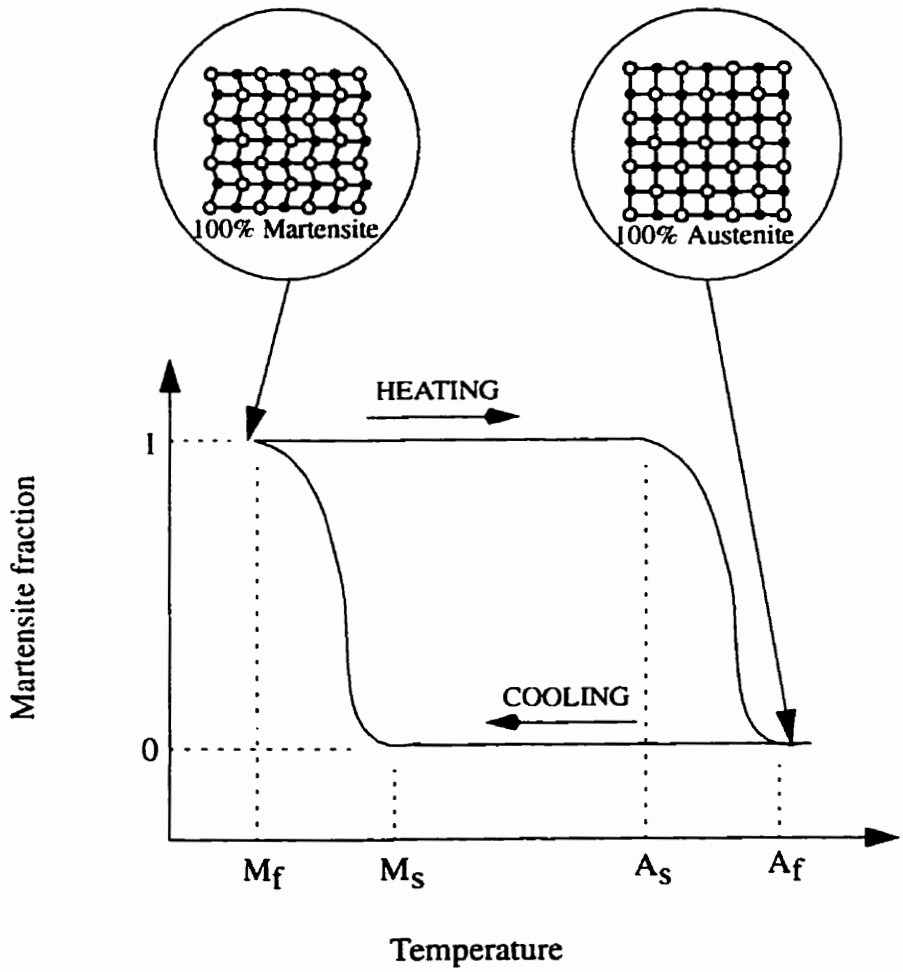

Figure 1.1: Transformation curve of a SMA

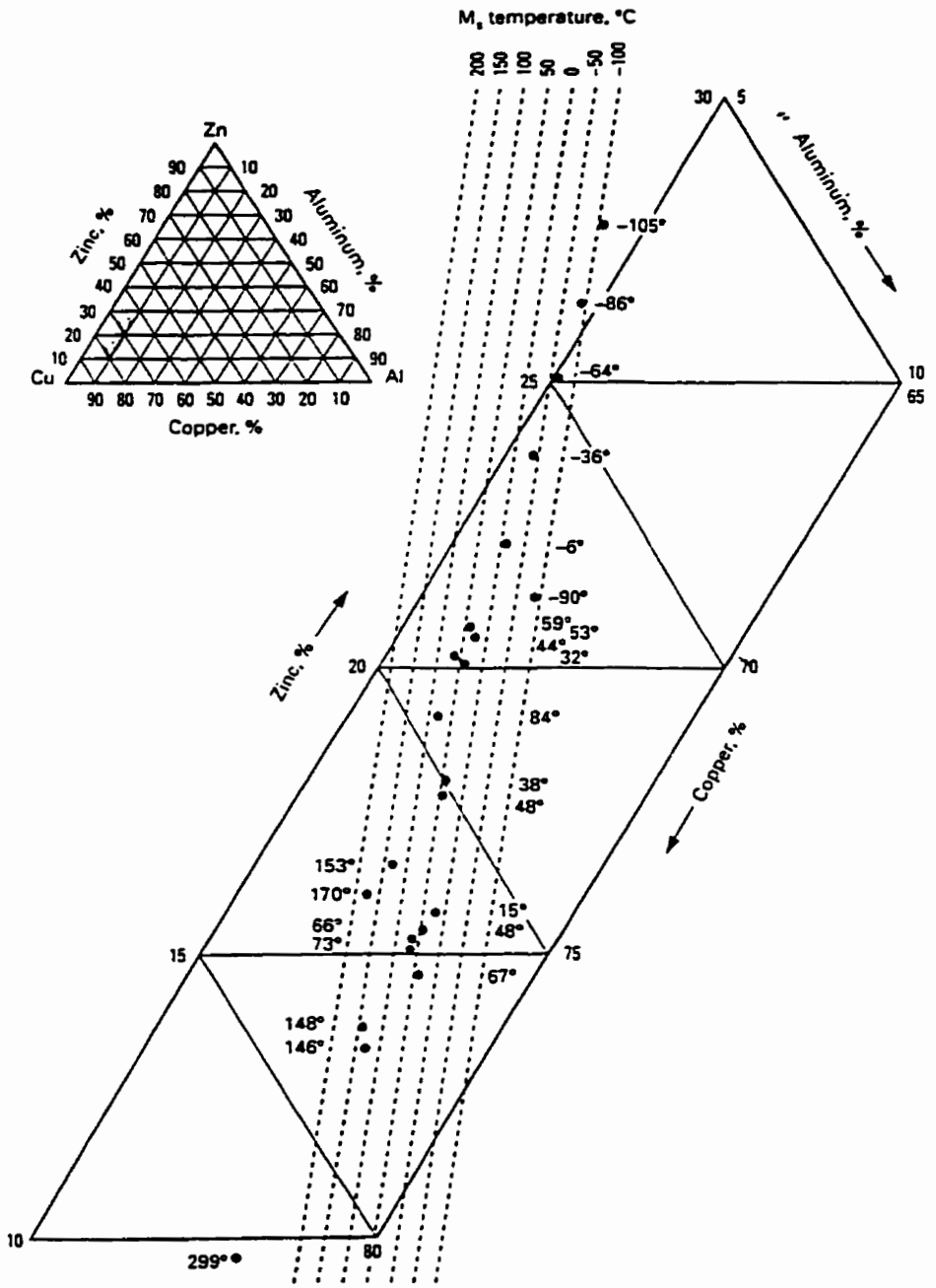

Figure 1.2: M_s temperature as a function of the composition of CuZnAl (After Wu et al., 1991)

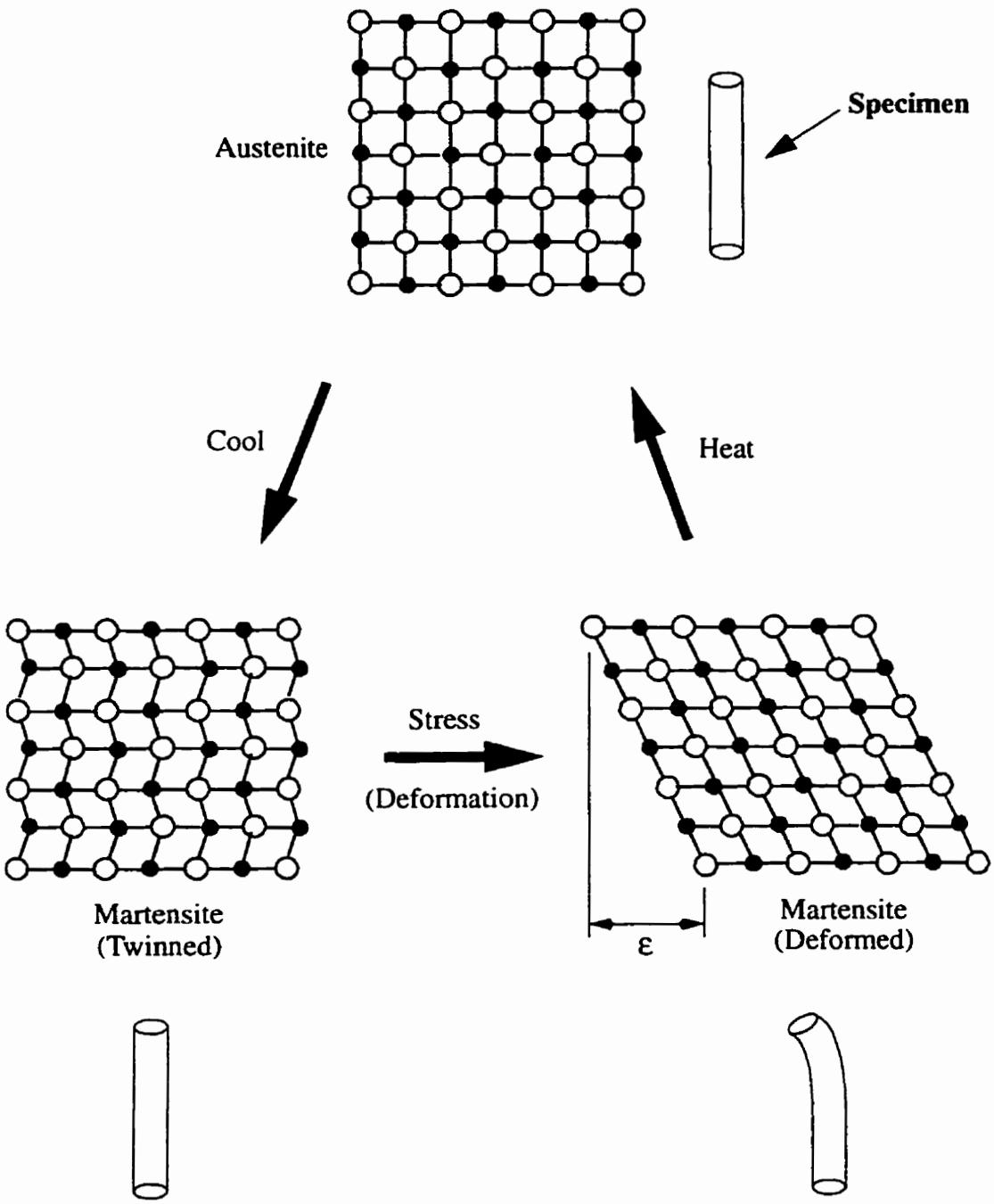

Figure 1.3: Schematic of the Shape Memory Effect (After Dye, 1992)

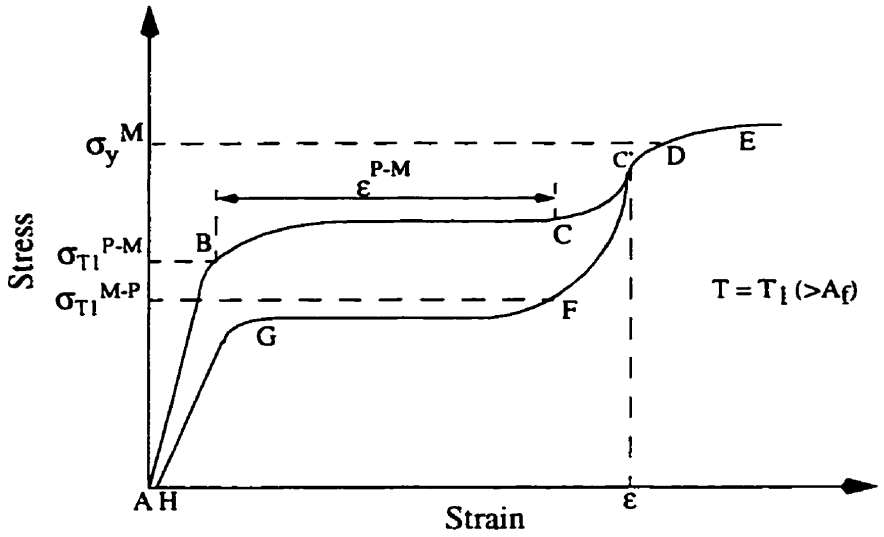

Figure 1.4: Typical stress-strain curve showing superelastic behavior. (After Krishnan et al., 1974)

2 Experimental Program

2.1 Description of Materials

CuZnAl in the austenitic phase at room temperature and CuZnAl in the martensitic phase at room temperature were studied in this work. For the purposes of this thesis, the two types of CuZnAl alloys will be referred to as austenitic CuZnAl alloy and martensitic CuZnAl alloy. The austenitic CuZnAl alloy was purchased from the Memry Corporation, Conneticut. The martensitic CuZnAl alloy was donated by the Memry Corporation. The Memry Corporation did not provide data on the superelastic and mechanical properties of the two CuZnAl alloys.

Austenitic CuZnAl alloy was supplied in the finished state in the form of 6 mm (0.236 in.) diameter straightened rods. Each rod was 1.5 ft. in length. Memry Corporation had subjected this batch of material to the following heat treatment: $500°C$ for 30 minutes, followed by $800°C$ for 15 minutes and water quenched thereafter. The heat treatment was required to stabilize the transformation temperatures of the alloy. The chemical composition of the austenitic CuZnAl, determined by Cambridge Materials Testing Limited of Cambridge, Ontario, is given in Table 2.1. The transformation temperature of the austenitic CuZnAl as specified by the supplier is given in Table 2.2. The microstructure of the austenitic alloy at room temperature is shown in Figure 2.1.

The martensitic CuZnAl alloy was received as a 6 mm (0.236 in.) diameter coiled rod with a total length of about 14 feet. The supplier had not carried the heat treatment to completion on this material. As a result, the final heat treatment of the martensitic CuZnAl was done at the Metallurgical Laboratories of the University of Manitoba. The 6 mm coiled rod was cut into pieces, 11 inches in length. Each piece was swagged to a diameter of 5.84 mm (0.230 in.). The swagging was carried out to straighten the coiled rod. The swagging process successfully straightened the rods with a small loss in diameter. The heat treatment had to be carried out in a small oven. Hence it was decided to machine the

martensitic CuZnAl into test specimens before heat treatment so that the specimens would fit in the oven. The specimens were heat treated as follows: $800°C$ for 30 minutes under constraint followed by water quenching. During the heat treatment the specimens had to be constrained to prevent them from reverting to the original shape. For this purpose, a form, shown in Figure 2.2, was made out of stainless steel. The form consisted of a stainless steel block split into top and bottom halves with five holes drilled along the joint between the two halves. The two halves were held in place during the heat treatment by means of four screws on each of the four corners of the rectangular form. The form could hold five specimens at a time. Figure 2.3 shows the form ready to be removed from the oven following the heat treatment process. Following the heat treatment, the specimens were annealed at $100°C$ for 24 hours. The aging process is performed to obtain stable transformation temperatures. The chemical composition of the material, determined by Cambridge Materials Testing Limited of Cambridge, Ontrario, is given in Table 2.1. Following the heat treatment and annealing, a sample of the martensitic CuZnAl was sent to the Memry Corporation to obtain the transformation temperatures. The transformation temperatures of the martensitic CuZnAl, as determined by the Memry Corporation, is given in Table 2.2. The microstructure of the martensitic CuZnAl at room temperature is shown in Figure 2.4.

2.2 Test Specimen Design and Preparation

Test specimens for the different tests were designed according to ASTM specifications. The standards followed were the ASTM E 3M (ASTM E8M, 1990), ASTM E606 (ASTM E606, 1990) and ASTM E466 (ASTM E466, 1990) for tensile, low-cycle fatigue (LCF) and high-cycle fatigue (HCF) tests respectively. Given the small diameter of the CuZnAl alloy rods, specimens were made so as to have the maximum test section diameter while still conforming to the ASTM Standard requirements for small sized specimens. Drawings of the specimens are shown in Figure 2.5 with dimensions given in Table 2.3. A photograph showing the actual test specimens is shown in Figure 2.6, where the specimens are, from left to right, LCF, HCF and tension test specimens.

The specimens were made by cutting the CuZnAl rods into the approximate length of the test specimens. Following this, the ends of each specimen were threaded. The specimens were then mounted on a lathe and the test section reduced to the required diameter using a roughing tool. Finally the fillet radius was incorporated into each specimen using a radius tool to make a smooth transition from the grip section to the test section of each specimen. The radius of the transition zone was selected to minimize any stress concentrations that might occur in the transition zone. During the machining process an oil based lubricant was employed to minimize any damage to the test specimen. However, surface strain hardening of the specimen could still occur.

The fatigue samples were polished in a five stage process. A lathe was employed in the polishing process to ensure uniformity. The samples were longitudinally polished using 320, 400 and finally 600 grit paper in that order. This was followed by polishing using 6 micron diamond paste. A final polish was done using 1 micron diamond paste. At the end of each stage of polishing, the fatigue specimens were cleaned and observed under a microscope (x30 magnification) to ensure a uniform polish. A polishing cloth, with kerosene as the suspension medium, was used while polishing with diamond paste. Although only the HCF test specimens required a polish, both LCF and HCF test specimens were polished. This is because failure in HCF is controlled by the propagation of cracks from the specimen surface. The aim of polishing the HCF samples was to eliminate surface cracks before testing was begun. In LCF, the failure mechanism is governed by plastic strain and not by the presence of surface cracks.

For the LCF and HCF tests, an alignment fixture was made to reduce the effect of eccentric loading on the specimens resulting from any misalignment of the top and bottom grips of the test frame or any loss of parallelism in the machined test specimen. The alignment fixture, made of stainless steel, is shown in Figure 2.7. It consists of a solid circular disk with six threaded bolt holes drilled around the perimeter on top of which lies another circular disk. The top circular disk has six holes drilled around the perimeter to attach it to the bottom disk. The top disk has two circular cavities of different diameters built into it. The upper cavity has the smaller diameter. A gripping fixture which is placed between the two disks is made so that it can be moved around within the cavities of the upper disk to

reduce misalignment and the resulting eccentric loading on the specimens. Once the specimen is attached to the gripping fixture the two circular disks are securely fastened together.

2.3 Tests Conducted

All tests were conducted at room temperature ($22°C$). This ensured that the austenitic CuZnAl ($A_f = 7.3°C$) remained austenitic and the martensitic CuZnAl ($M_f = 18°C$, $M_s = 42°C$) remained martensitic respectively before each test. Though room temperature is higher than the M_f temperature, the martensitic samples were in the martensitic phase because the samples were cooled to a temperature below M_f after the heat treatment.

2.3.1 Standard Tension Tests

The tension test was performed to obtain basic design information on the strength of CuZnAl alloys. A screw-type Instron machine was used for the tensile tests. An extensometer, connected to a strain amplifier, was used to measure the strains. The data was recorded using a personal computer. This static machine was used because it had a load cell that could be calibrated to different loads. This was ideal, as the load cell capacity could be changed to be sensitive enough to measure the small loads required by the small diameter test specimens. Also, at the point of specimen failure, the amount of sudden movement the extensometer would be subjected to at the point of specimen failure is much smaller than if a servohydraulic test machine was used. Figure 2.8 shows the tension test setup. The tension test specimen was subjected to a continually increasing uniaxial load, while simultaneous measurements of the elongation of the specimen were made. The stress on the specimen at a given time in the test was obtained by dividing the uniaxial load by the original cross-sectional area of the specimen. From the applied stress and the corresponding strain measurements obtained during the test, a stress-strain curve was plotted.

From the stress-strain curve, the following material properties were determined:

1) tensile strength, or ultimate tensile strength, s_u, and

2) ultimate strain, e_f.

The modulus of elasticity of the CuZnAl was measured during the low-cycle fatigue tests because the low-cycle fatigue machine had an accurate means of determining the modulus of elasticity.

For a more detailed description of the tensile test and a full list of material properties which can be obtained from a tension test, the reader is referred to the ASM Handbook on Mechanical Testing (1992). Seven CuZnAl specimens were tested. The tension test samples were loaded at a user specified, constant strain rate. Four austenitic CuZnAl tensile specimens were tested at three different strain rates. This was done to see if the tensile behavior of the alloy was strain rate dependent. Three martensitic CuZnAl tensile specimens were tested at a constant strain rate. The samples and the strain rates at which they were tested are shown in Table 2.4.

2.3.2 Stress and Strain Cycling Tests

Strain cycling experiments were conducted to observe the superelastic behavior of SMA. It is the occurrence of superelasticity in shape memory alloys that implies they have higher fatigue lives. The strain cycling experiments involved loading tension test specimens to pre-determined strain levels and unloading. The experiments were conducted at a strain rate of $1.0 \times 10^{-4}\, s^{-1}$. The load and strain data were collected using a data acquisition system. The austenitic CuZnAl samples ASC1 and ASC2 were subjected to strain cycling only. Each of the specimens were cycled repeatedly to the predetermined strain value and unloaded. The specimens and the strain cycling program to which each were subjected are identified in Table 2.5. Three martensitic CuZnAl alloy specimens, MSC1, MSC2 and MSC3, were subjected to stress cycling. The tests involved straining the specimens to a predetermined strain value followed by unloading. In the subsequent cycles, the

specimens were stressed to the maximum stress level reached in the first cycle.The initial strains to which the three samples were strained along with the total number of stress cycles they were subjected to are given in Table 2.6. Only the prescribed number of cycles were carried out as this was an investigative study.

2.3.3 Low-Cycle Fatigue (LCF) Tests

The fatigue behavior of metals is important in the design of components subjected to cyclic loading. The magnitude of nominal stress on a cyclically loaded component is measured by determining the amount by which the applied stress is greater or less than the fatigue strength of the material of which the component is made. The LCF regime is characterized by stresses greater than the fatigue strength of the material while the high-cycle fatigue regime is characterized by stresses lower than the material fatigue strength. Stresses lower than the fatigue strength of the material results in elastic deformation while stresses greater than the fatigue strength leads to plastic deformation. It has been shown that damage is dependent on plastic deformation or strain (Bannatine et al., 1990). Most engineering structures are designed such that the working loads are well below the fatigue strength of the material and hence the deformation remains elastic. However, there are instances where stress concentrations occur in certain elements causing plastic strains to occur or it happens that a particular type of loading is such that the loads are always higher than the fatigue strength of the material. An example of the latter case is the landing gear in an aircraft. The landing gear has to be replaced after a set number of landings to prevent failure. For application such as this, understanding of the material LCF behavior is important.

In the laboratory, LCF experiments are conducted by subjecting test specimens to controlled cycles of strain. The usual practice is to subject the specimen to a sinusoidal strain cycling program between a maximum and minimum strain level, as shown in Figure 2.9, and the test carried out till specimen failure occurs. The number of cycles at the time of failure is noted. The strain can be separated into elastic and plastic components. The common method of presenting LCF test data is to plot either the plastic strain amplitude,

$\frac{\Delta\varepsilon_p}{2}$, or the total strain amplitude, $\frac{\Delta\varepsilon_t}{2}$, versus the number of reversals to failure, $2N_f$. The number of reversals to failure is equal to twice the number of cycles to failure, N_f. LCF tests can be carried out at very low frequencies (0.1 - 1 Hz.) because the specimens fail in a relatively few number of cycles ($<10^5$) compared to HCF tests. Detailed information on carrying out LCF tests can be found in the Fundamentals of Metal Fatigue Analysis (Bannatine et al., 1990) and, Manual on Low Cycle Fatigue Testing (STP 465, 1969). LCF test information can also be obtained from the ASTM standard E606 (ASTM E606, 1990).

The low-cycle fatigue test program was carried out to investigate the fatigue behavior of both austenitic and martensitic CuZnAl in the plastic range. The tests were conducted at room temperature with the total cyclic strain amplitude, ε_a, as the independent variable. The LCF test specimens were subjected to a strain controlled, sinusoidal waveform between ε_{max} and ε_{min}. The strain amplitudes selected, between 0.3% and 4%, were strains which would produce failure between 1 and 50000 cycles. All LCF tests were carried out at a frequency of 0.5 Hz. The initial loading in tests at strain amplitudes greater than 1.5 percent were begun in compression to eliminate the possibility of developing a locally necked region in the specimen during the first tensile loading cycle (STP 465, 1969). Six austenitic LCF specimens were tested. Specimen buckling occurred when it was attempted to test an austenitic sample at a strain amplitude of 2%. As a result the maximum strain amplitude at which the austenitic samples were tested at was 1%. Ten martensitic LCF specimens were tested. Attempts to test specimens at strain amplitudes of 2, 3 and 4% resulted in the specimens buckling. The buckling was inevitable at such high strain amplitudes due to the slenderness of the LCF specimens. Therefore, the martensitic CuZnAl was also tested successfully to a maximum strain amplitude of only 1%. It was observed that there was a slight rise in the temperature of the specimens after the completion of the LCF tests. However, the temperature was not monitored during the tests.

Fully reversed, total strain controlled LCF tests were conducted in an air atmosphere at room temperature using a servohydraulic Instron testing machine (model 8502)

with a digital control system (model 8500 plus). The test machine was equipped with a 250 kN load cell. Strain measurements were obtained using an Instron extensometer with a range of ±10%. Figure 2.11 shows the LCF experimental setup. The LCF tests were conducted using Instron LCF software which relied on the extensometer for feedback control of strain during the tests. Before the start of each LCF test, the LCF test machine measured the modulus of elasticity of each test specimen by applying a cyclic load at a low frequency. The LCF software monitored the test and collected the test data. The data recorded for each test included the tensile peak stress, σ_{max}, the compressive peak stress, σ_{min}, the stress range, $\Delta\sigma = \sigma_{max} + |\sigma_{min}|$, the tensile peak total strain, ε_{max}, the compressive peak total strain, ε_{min}, the total strain range, $\Delta\varepsilon_t = \varepsilon_{max} + |\varepsilon_{min}|$, and the number of cycles to failure N_f.

2.3.4 High-Cycle Fatigue (HCF) Tests

In the laboratory, HCF experiments were conducted by subjecting test specimens to controlled cycles of stress. The usual practice is to subject the specimen to a sinusoidal stress cycling program between a maximum and minimum stress level, as shown in Figure 2.10, and the test carried out till specimen failure occurs. The number of cycles at the time of failure is noted. The common method of presenting high-cycle fatigue data is to plot a log-log plot of the stress level versus the number of cycles to failure, N. HCF tests have to be carried out at higher frequencies (25-150 Hz.) because specimen failure occurs after a large number of cycles ($10^5 - 10^7$). Detailed information on carrying out high-cycle fatigue tests can be found in the Fundamentals of Metal Fatigue Analysis (Bannatine et al., 1990) and ASTM E466 (ASTM E466, 1990).

The HCF tests were conducted to study the fatigue behavior of CuZnAl (austenitic and martensitic) in the elastic range. The HCF specimens were subjected to a alternating stresses between 150 MPa and 300 MPa inclusive, in a fully reversed load cycle (Stress Ratio, R = -1). A sinusoidal wave form was adopted for the HCF test program. The testing

was carried out at a frequency of 25 Hz. Seven austenitic HCF specimens and 12 martensitic specimens were tested to determine their respective HCF properties. The stress-strain curves of the CuZnAl alloys were recorded at logarithmic intervals during the high-cycle fatigue tests to observe their response to reversal loading and are given in Appendix C. The response of the material as a function of both stress level and the number of cycles could be observed. The HCF tests were stopped at the predetermined number of cycles, an extensometer attached to the specimen, and the test run at a frequency of 0.1 Hz to record the hysteresis loops. The low frequency was chosen in order to protect the extensometer from possible damage at higher frequencies. A data acquisition system, a PC running Labtech Notebook software, was used to record stress and corresponding strain values. Once the data was recorded the testing machine was stopped and the extensometer removed from the specimen. Then the HCF test was restarted. It was observed that there was a slight rise in the temperature of the specimens after the completion of the HCF tests. However, the temperature was not monitored during the tests.

Fully reversed, stress controlled HCF tests were conducted in an air atmosphere at room temperature using a servohydraulic Instron testing machine (model 1332) with a digital control system (model 8500). The test frame was equipped with a 98 kN load cell. Figure 2.12 shows the HCF experimental setup. The stress amplitude σ_a, and the number of cycles to failure N_f, were recorded for each specimen.

2.3.5 Material Damping Properties

The ability of a material to absorb energy is known as damping. Damping is important in structures to control excessive resonance vibrations which may cause high stresses, leading to premature failure. A reduction in resonance induced vibrations by improved damping properties of a structure translates into a reduction in resonance induced fatigue. Damping can also be used in noise control applications such as the control of noise radiation from vibrating surfaces, or the control of noise transmission through a vibrating surface. In these applications the noise is not reduced by sound absorption but by decreasing the amplitude of the vibrating surfaces. Methods used to measure damping include the

stress-strain (or load-deflection) hysteresis loop method, procedures involving a vibrating specimen, lateral deflection of rotating cantilever method and high frequency pulse techniques. The hysteresis loop method provides a direct and easily interpreted measure of damping energy. A hysteresis loop, Figure 2.13, is obtained by subjecting a test specimen to cyclic loading and measuring the stress or load and the corresponding strain or deflection. In this thesis the hysteresis loop method is employed to quantify the energy dissipation of CuZnAl alloys.

The two general types of units used to specify damping properties of structural materials are the absolute and relative damping units. The absolute damping units give a measure of the energy dissipated per cycle in a structural element or test specimen. The relative damping unit is a ratio of the energy dissipated per cycle in a structural element or test specimen to a reference strain energy or elastic energy. The absolute damping energy units are:

D_s = total damping energy dissipated or absorbed by the entire specimen or structural element per cycle of vibration $\left(\frac{N \cdot m}{cycle}\right)$. This quantity is a member property. In other words it depends on the dimensions of the member used. The total damping energy is equal to the area under the load-displacement $(P - X)$ hysteresis loop. D_s can be expressed as:

$$D_s = \oint_0^{\frac{2\pi}{\omega}} P\left(\frac{dX}{dt}\right)dt \tag{2.1}$$

D = specific damping energy is the energy dissipated or absorbed by a macroscopically uniform material per unit volume per cycle of loading $\left(\frac{N \cdot m}{m^3 \cdot cycle}\right)$. This measure of damping is a material property and is independent of the specimen dimensions. The specific damping energy is equal to the area under the stress-strain $(\sigma - \varepsilon)$ hysteresis loop (Figure 2.14). D can be expressed as:

$$D = \oint_0^{\frac{2\pi}{\omega}} \sigma\left(\frac{d\varepsilon}{dt}\right)dt \tag{2.2}$$

The area within the hysteresis loop represents the energy absorbed by the material in one full cycle of deformation, and is directly related to the performance of a potential energy absorbing device made of that material.

The relative damping energy unit is the loss coefficient, η, which is a dimensionless ratio of damping energy and strain energy. Relative energy units are also defined for a specimen and for a particular material type. For a member, the loss coefficient, η_s, is defined as:

$$\eta_s = \frac{D_s}{2\pi U_s} \tag{2.3}$$

For a material, the loss coefficient, η, is defined as:

$$\eta = \frac{D}{2\pi U} \tag{2.4}$$

U_s is the unit strain energy of a specimen at maximum deflection. U is the unit strain energy of a material at maximum strain. The unit strain energy is also determined from the hysteresis loops. For a material, the unit strain energy is the area under the mid-stress curve and the strain axis, Figure 2.15. The "mid-stress" curve is determined by averaging the stresses given by the loading branch and the unloading branch, all at the same strain ε. The unit strain energy of a specimen can be determined in a similar manner using the load-deflection curve. In this thesis, the damping properties measured were D and η. Methods used in the calculation of these damping parameters are given in Appendix D. More information on structural damping can be obtained in Damping of Materials and Members in Structural Mechanics (Lazan, 1968).

Damping in materials occur as a result of some phenomenon that takes place within the material when stress is applied. In CuZnAl alloys there are three possible mech-

anisms which lead to damping. The first is the superelastic effect exhibited as the hysteresis loops during stress cycling of austenitic CuZnAl. The energy applied is dissipated by the formation and annihilation of stress induced martensite which is also accompanied by the generation and dissipation of heat which also helps to reduce the applied stress. The second mechanism is through plastic deformation of the material. The energy applied leads to plastic deformation of the material which creates permanent damage to the material thus leading to the dissipation of the applied energy. Finally, CuZnAl at the martensitic finish temperature, M_f, experiences a damping peak as a result of internal friction within the crystals. This last form of damping was not addressed in this thesis.

One of the objectives of this thesis was to compare the amount of energy dissipation (damping) associated with each of elastic deformation (HCF), inelastic deformation (LCF) and superelasticity. To measure the amount of damping associated with the elastic deformation the hysteresis loops during the HCF tests were recorded. This was done by stopping the HCF tests at previously determined logarithmic intervals, installing a extensometer on the fatigue specimen and cycling the specimen at a frequency of 0.1Hz. The stress-strain data was recorded using a PC based data acquisition system (Labtech Notebook). However this method was not very successful because of the low stress level involved and the fact that the extensometer was not sensitive enough to detect the hysteresis loops. In order to quantify the damping capacity of the CuZnAl alloys due to inelastic (plastic) deformation, the hysteresis curves at the half-life of the LCF test samples were recorded. This LCF hysteresis data was recorded automatically by the Instron LCF test software used in the LCF test program. The damping capacity of austenitic CuZnAl due to superelasticity was measured using the hysteresis curves obtained during the strain controlled cycling of austenitic CuZnAl. Here again the extensometer was attached to the test sample and the stress-strain data was recorded using a PC based data acquisition system.

Material	% Weight of Element				
	Copper	Zinc	Aluminum	Zirconium	Silver
Austenitic CuZnAl	69.5	26.5	3.8	0.09	-
Martensitic CuZnAl	70	25.7	4.05	0.09	0.06

Table 2.1: Chemical composition of the CuZnAl alloys

Material	Transformation Temperatures (^{o}C)			
	M_f	M_s	A_s	A_f
Austenitic CuZnAl	-15.9	-7.3	1.0	7.3
Martensitic CuZnAl	18	42	38	56

Table 2.2: Transformation temperatures of the CuZnAl alloys

Test Type	G_L	D_T	D_G	R	L_{TH}	s	Thread type
Tension	30	4	6	4	10	2	6 x 1
High-cycle fatigue	15	4.2	6	41	15	2	6 x 1
Low-cycle fatigue	12	3.175	6	18	15	2	6 x 1

Table 2.3: Test specimen dimensions (mm.) (see Figure 2.5)

Specimen Name	Strain rate, (s^{-1})
AT1	5.75×10^{-5}
AT3	1.0×10^{-4}
AT4	2.0×10^{-4}
AT2	4.0×10^{-4}
MT1	2.0×10^{-4}
MT2	2.0×10^{-4}
MT3	2.0×10^{-4}

Table 2.4: Tension test specimens and strain rates

Sample	Test Series 1		Test Series 2	
	Strain (%)	Total Cycles	Strain (%)	Total Cycles
ASC1	0.3	5	1.0	2
ASC2	0.5	5	0.8	5

Table 2.5: Strain cycling test program for austenitic CuZnAl

Sample	Initial Strain (%)	Total Cycles
MSC1	0.3	75
MSC2	0.5	25
MSC3	0.8	5

Table 2.6: Stress cycling test program for martensitic CuZnAl

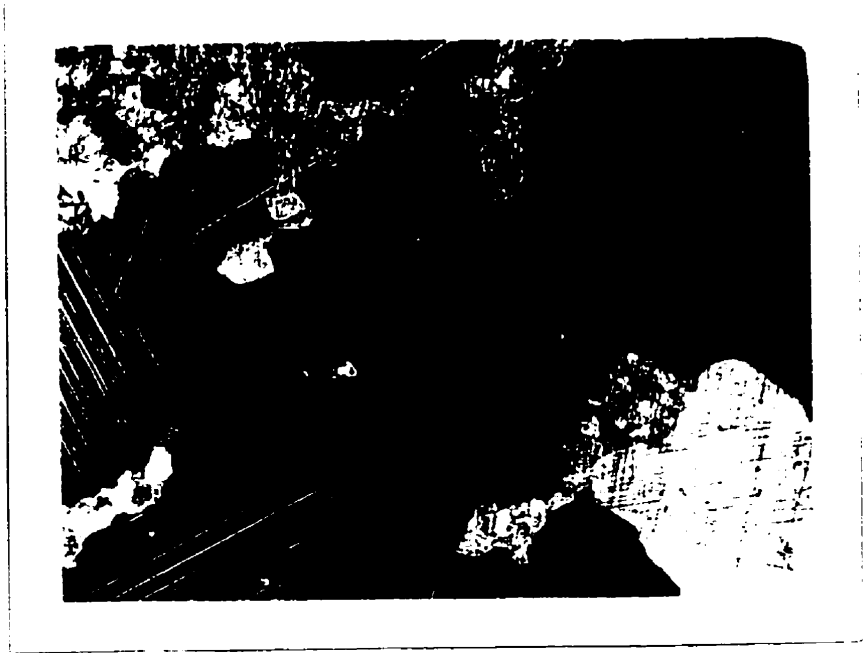

(a) Transverse cross section (x52)

(b) Longitudinal cross section (x52)

Figure 2.1: Microstructure of austenitic CuZnAl

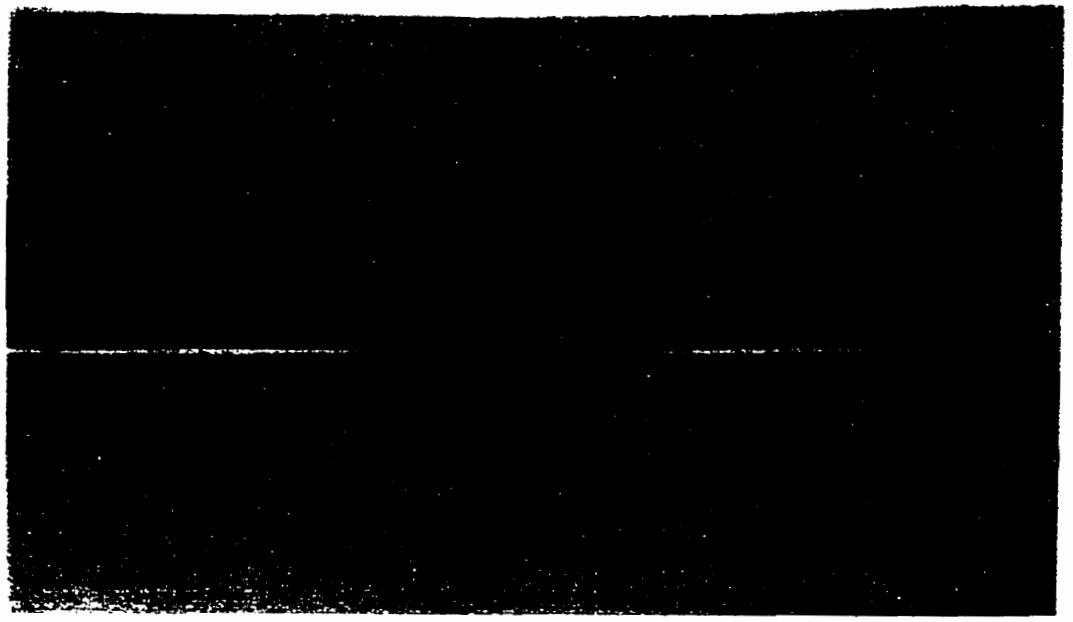

Figure 2.2: Form used in heat treatment

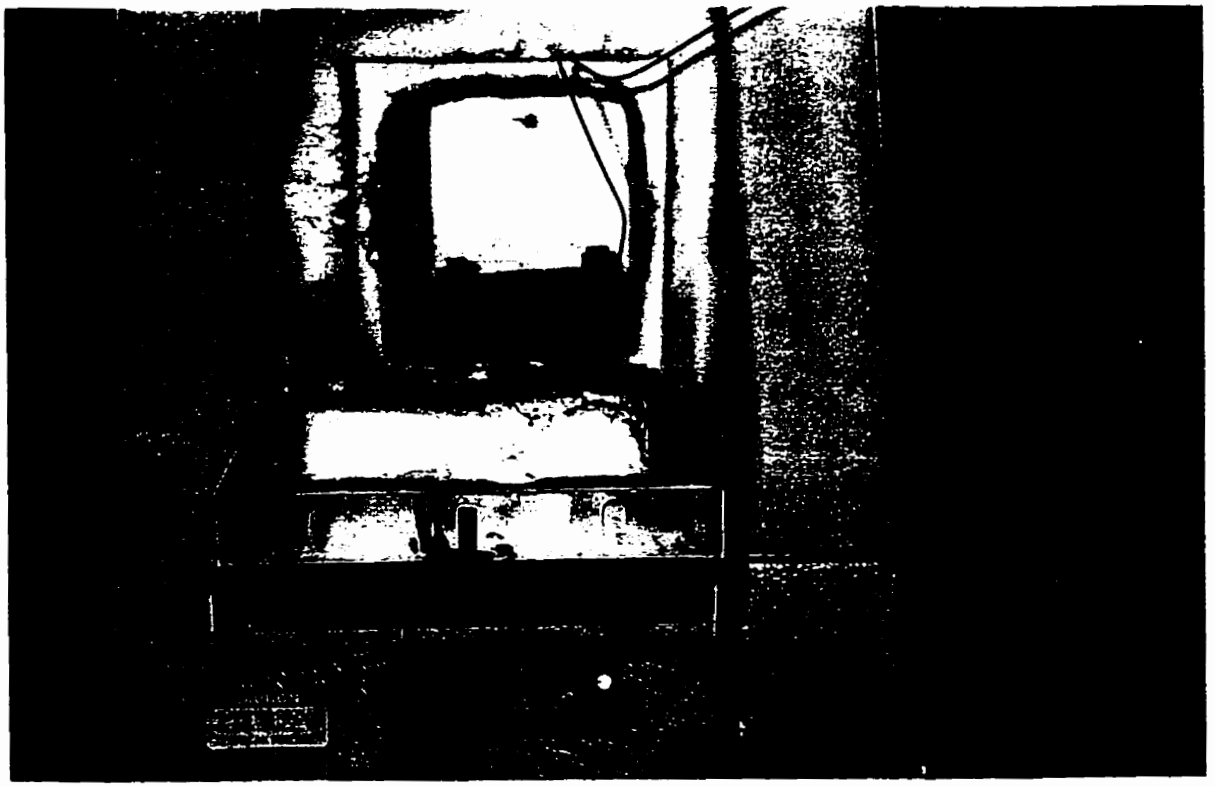

Figure 2.3: Form ready to be taken out of oven following heat treatment

(a) Transverse cross section (x420)

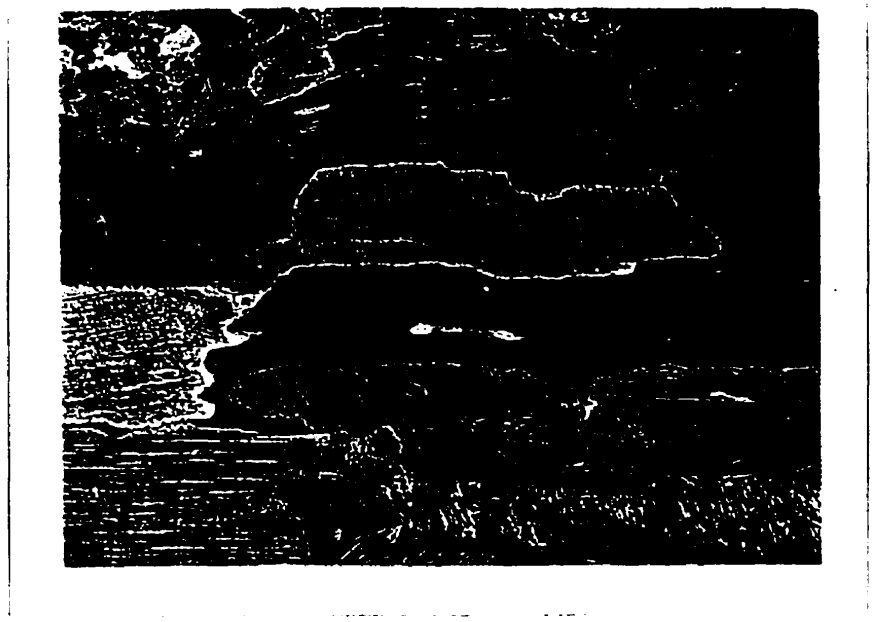

(b) Longitudinal cross section (x52)

Figure 2.4: Microstructure of Martensitic CuZnAl

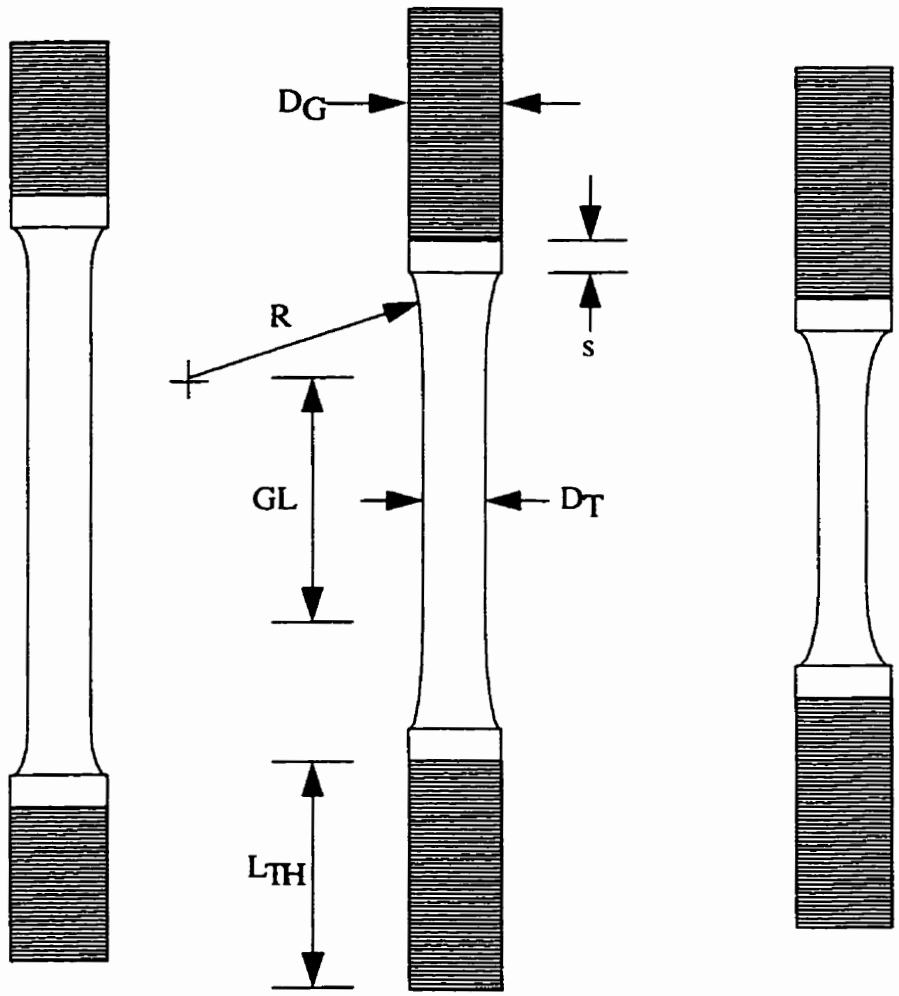

Figure 2.5: Test specimens for (a) tension test, (b) high-cycle fatigue, (c) low-cycle fatigue

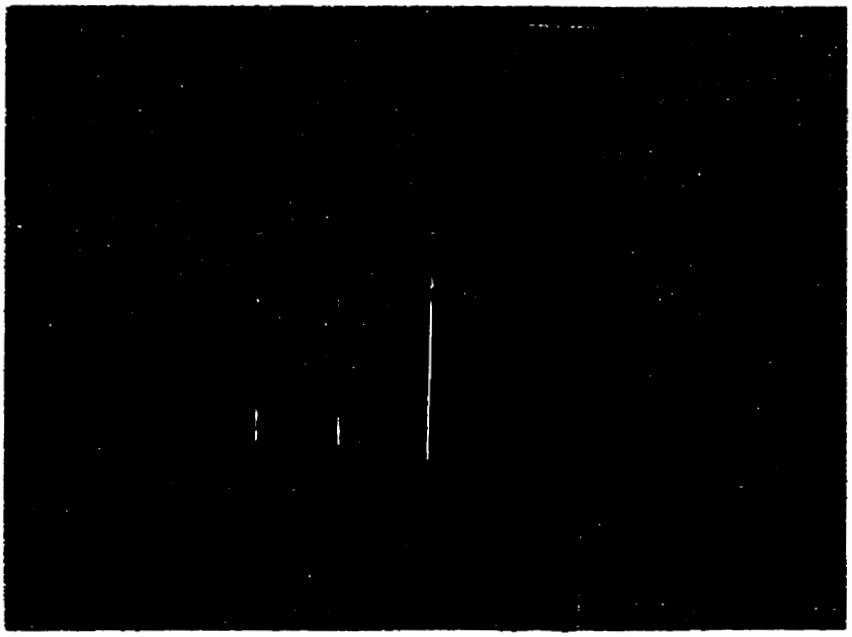

Figure 2.6: Photograph of the test specimens

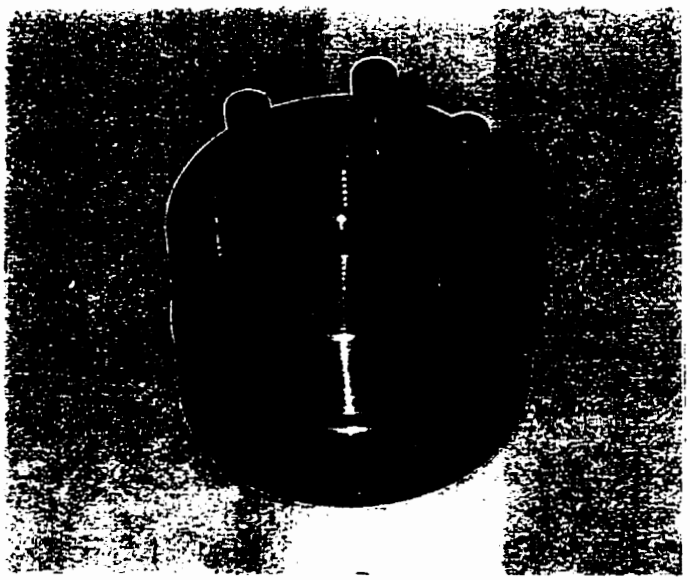

Figure 2.7: Alignment fixture for gripping LCF and HCF test specimens

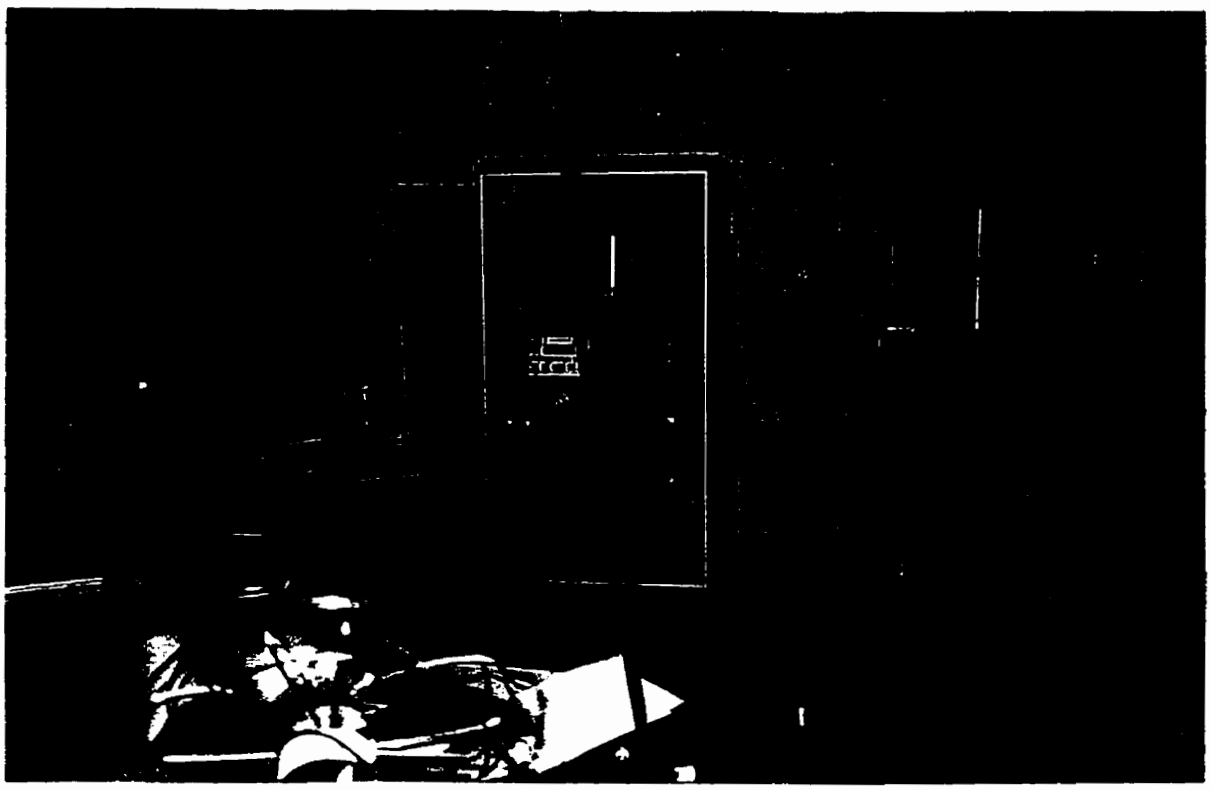

Figure 2.8: Tension and strain cycling test setup

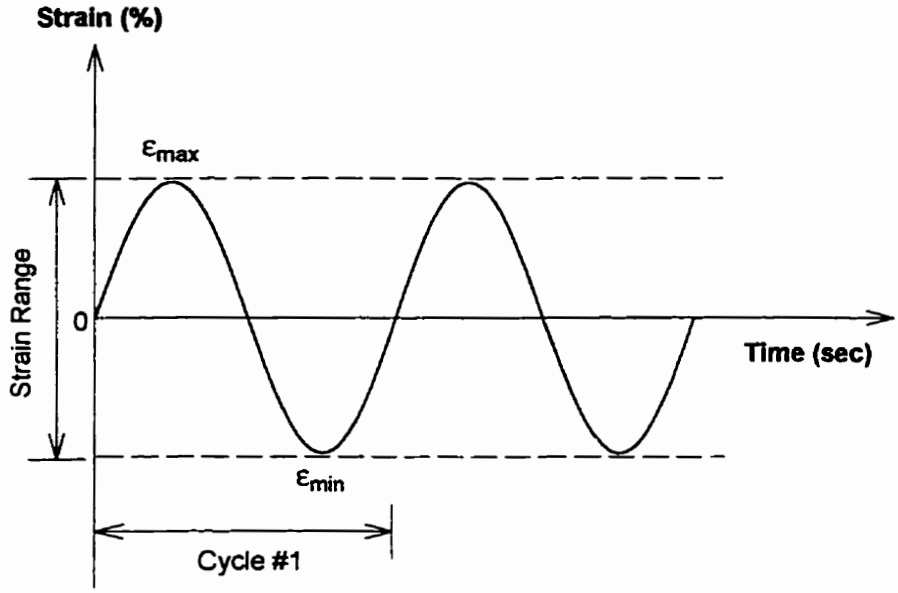

Figure 2.9: Sinusoidal wave form employed in the strain controlled LCF test program

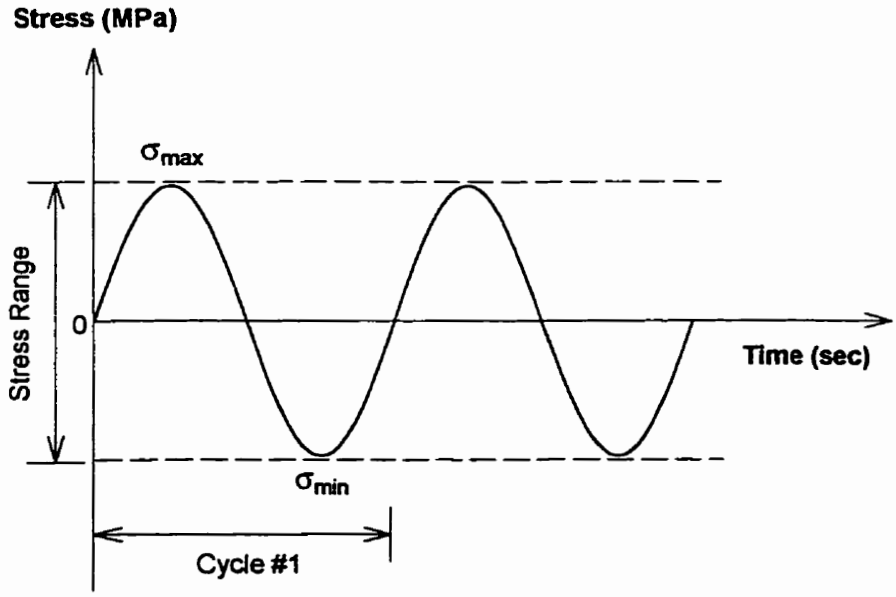

Figure 2.10: Sinusoidal waveform adopted in the stress controlled HCF test program

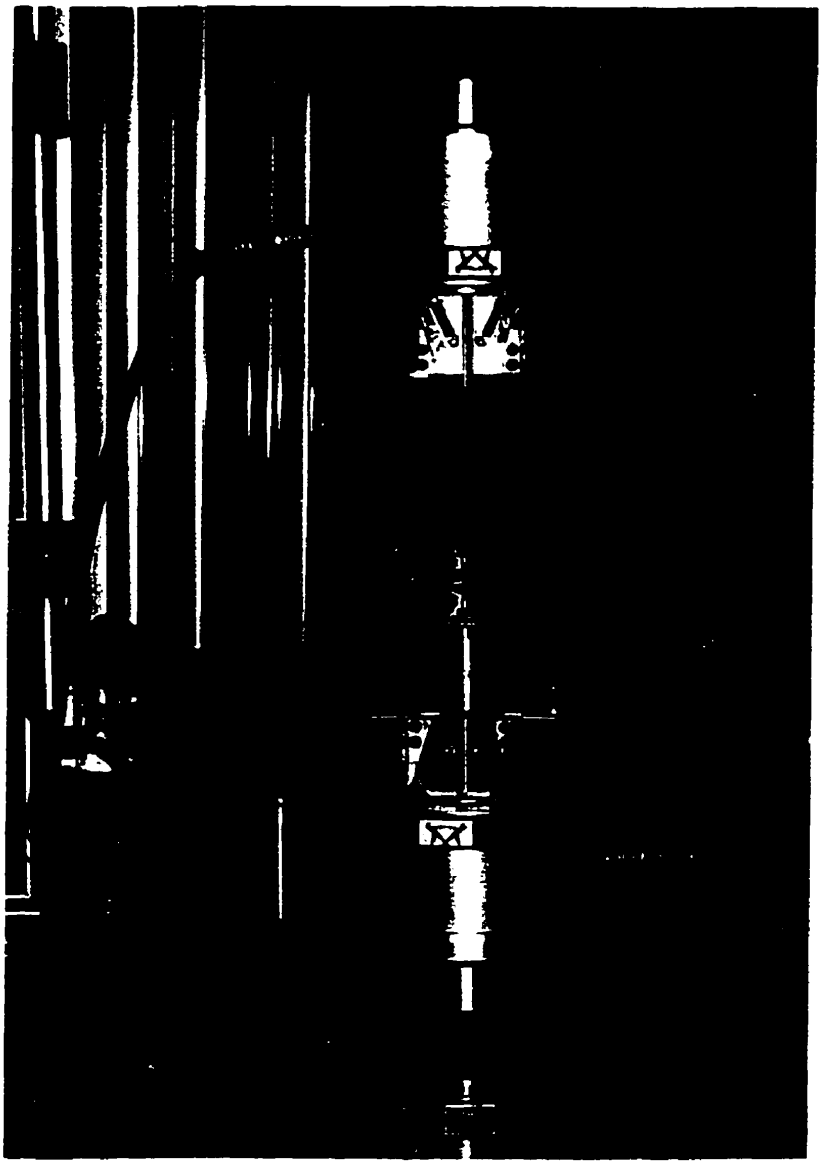

Figure 2.11: Low-cycle fatigue test setup

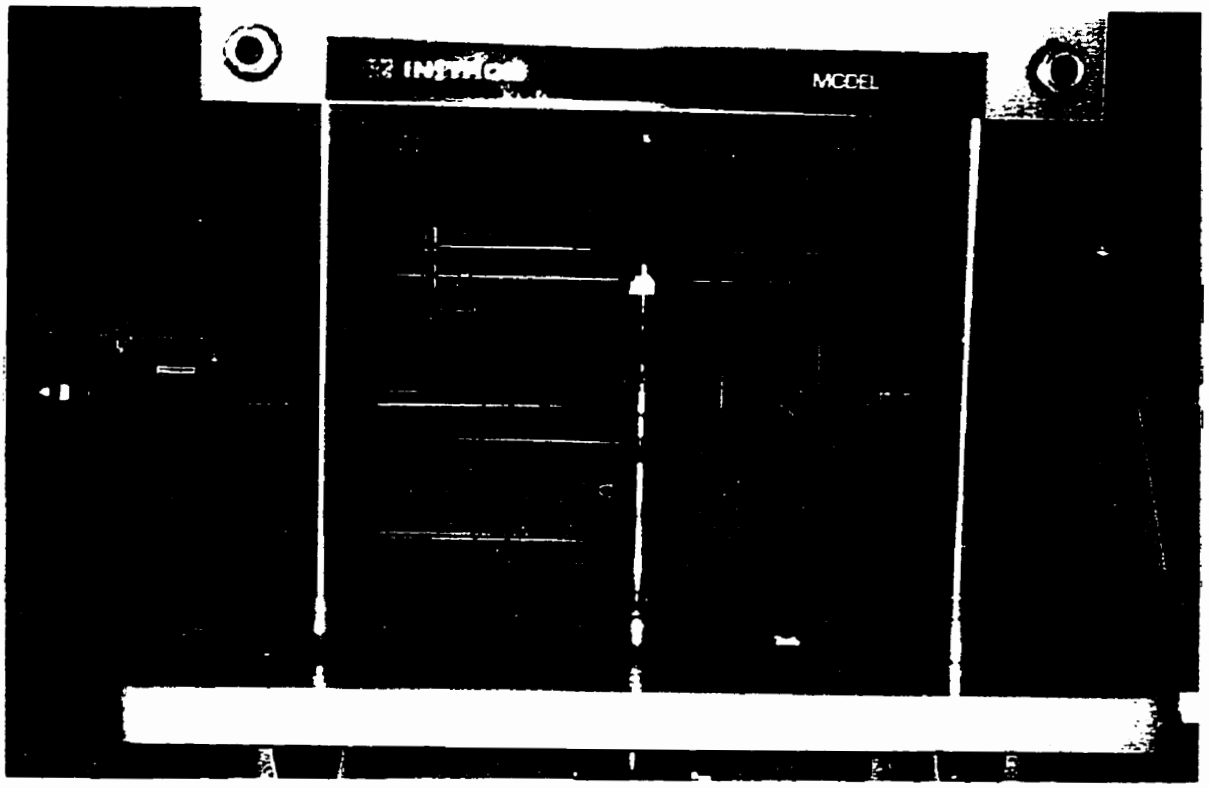

Figure 2.12: High-cycle fatigue test setup

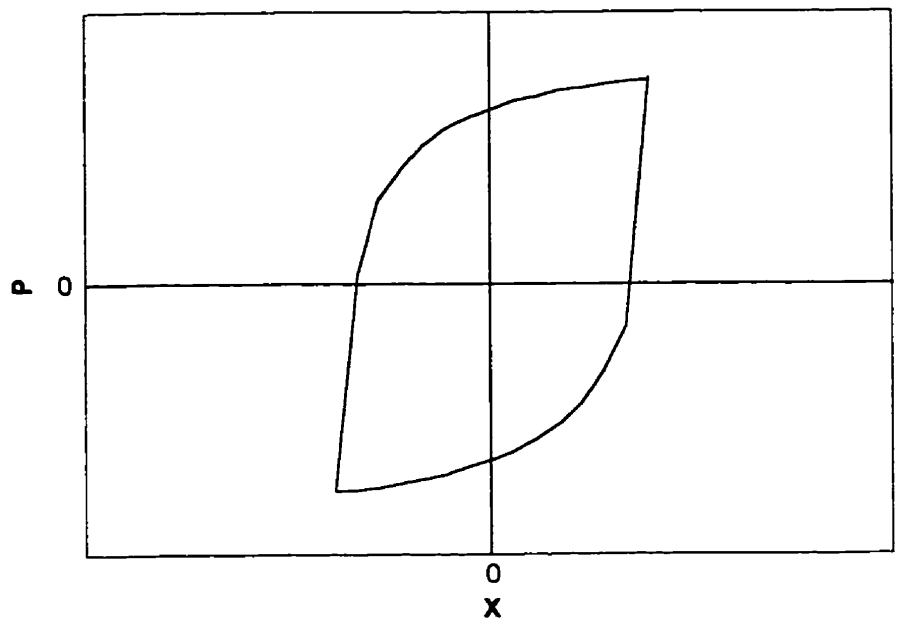

Figure 2.13: Load-deflection, $(P - X)$, hysteresis loop

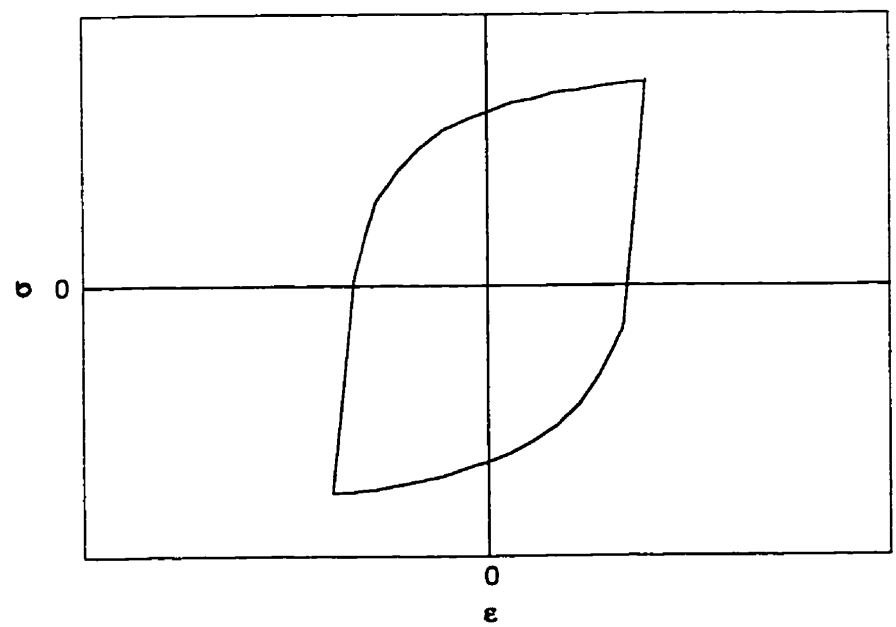

Figure 2.14: Stress-strain, $(\sigma - \varepsilon)$, hysteresis loop

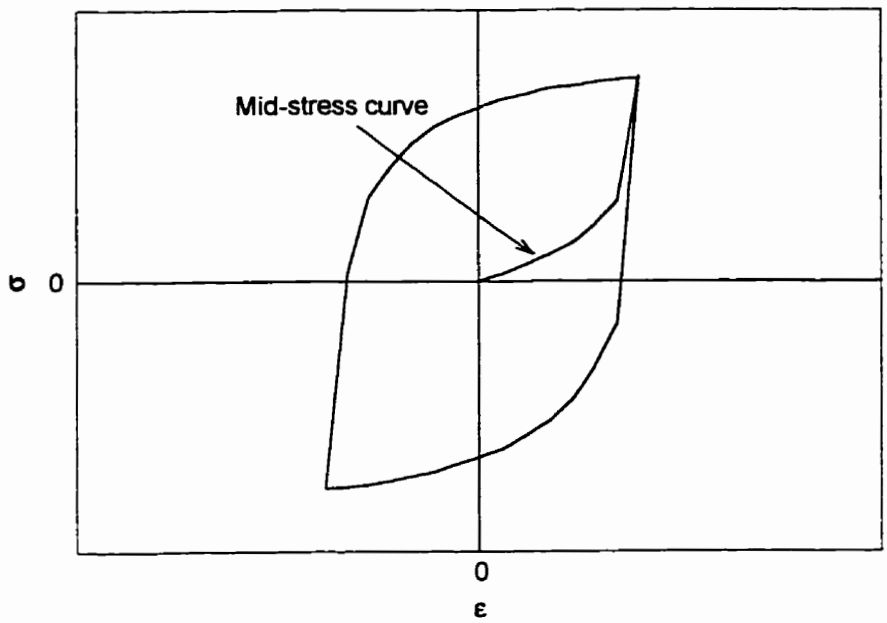

Figure 2.15: Mid-stress curve

3 Results and Discussion

In this chapter, the results of the experimental work are presented and discussed. For comparison purposes, the fatigue properties of CuZnAl determined in this study are compared with those of steel, aluminum and CuZnAl reported in the literature.

3.1 Tension Tests

The stress-strain curves from the tension tests of the austenitic CuZnAl alloy samples are shown in Figure 3.1. The ultimate tensile strength, S_u and the strain at fracture, ε_f, are given in Table 3.1. The stress-strain curves for each individual sample showing the calculation of S_u and ε_f are given in Appendix A. The modulus of elasticity, E, of the samples were measured from the LCF tests. The LCF test machine had the capability to measure the modulus of elasticity values accurately before the start of each LCF test. The measured modulus of elasticity values of austenitic CuZnAl are given in Table 3.2. The modulus of elasticity for the austenitic CuZnAl was determined to be 120000 MPa. The ultimate strength of the austenitic CuZnAl alloy is in the range between 351 - 427 MPa. The highest recorded strain at failure, 9.5%, occurred in sample AT4. Towards the point of failure, no appreciable necking of the specimen occurred. Observation of the four stress-strain curves in Figure 3.1 show that they are not similar. This is because the strain rates used in the four tests were different. All other test variables were held constant. Sample AT2, which had the highest rate of deformation, failed at the lowest ultimate strain. The stress-strain curve for sample AT3 shows an unloading portion because the sample was unloaded after 8% in order to prevent the specimen strain from exceeding the strain capability of the extensometer. Hence sample AT3 was not tested to failure. The fracture surface of sample AT4 is shown in Figure 3.27.

The stress-strain curves from the tension tests of the martensitic CuZnAl alloy are plotted in Figure 3.2. Samples MT1 - MT3 were all tested at the same strain rate and have

similar stress-strain relationships. A summary of the test results are given in Table 3.3. The ultimate strength varied from 548 MPa to 660 MPa. The strain at failure of the martensitic samples varied between 2.14 - 2.8%. The modulus of elasticity of martensitic CuZnAl, measured during the LCF tests, are given in Table 3.4. The average modulus of elasticity was determined to be 90000 MPa. No observable necking occurred in any of the specimens before failure. The fracture surface of sample MT1 is shown in Figure 3.28.

The material properties of austenitic and martensitic CuZnAl are compared in Table 3.5. Figure 3.3 shows the stress-strain curves for samples AT3 and MT1. The austenitic alloy is much stiffer compared to the martensitic alloy as indicated by the higher modulus of elasticity values. However, the martensitic alloys show much higher ultimate strengths than the austenitic CuZnAl alloys. The austenitic CuZnAl alloys, which failed at strain of up to 9%, show much more ductility compared to the martensitic alloys which failed at about 2.5% strain. From the tension test data it was not attempted to measure the yield stress or 0.2% proof stress. This is because in SMA the yield stress or 0.2% proof stress is not the stress at which significant plastic flow by slip occurs, rather the stress necessary to induce martensite (austenitic SMA) or re-orient existing martensite (martensitic SMA) under the action of the applied load (Melton et al., 1979b).

3.2 Stress and Strain Cycling Tests

Figure 3.4 shows the stress-strain curve of sample ASC1 which was strain-cycled to 1% strain and unloaded. A residual strain of 0.125% remains in the sample. On the second strain cycle to 1% strain the residual strain is reduced to about 0.09%. The strain cycling curves do not show well defined stress levels at which martensite forms and reversion to austenite occurs. Not all shape memory alloys have well defined pseudoelastic stress-strain curve as shown in Figure 1-1. For shape memory alloys without well defined pseudoelastic stress strain curves, the transformation stress levels can be determined by a method proposed by Pops and Ridley (1970). In this method the stress, where deviation from linearity on the stress-strain curve occurs, corresponds to the onset of martensitic transformation. Using this method the stress to induce martensite, σ^{P-M}, is measured at

62 MPa while the stress at which reverse transformation occurs, σ^{M-P}, was measured to be 30 MPa in the first cycle. In the second strain cycle σ^{P-M} was measured at 55 MPa which is slightly lower than that measured in the first cycle. Hysteresis curves for sample ASC2, cycled to 0.5% strain, is shown in Figure 3.5. In the first cycle, σ^{P-M} is measured at 48 MPa while σ^{M-P} is measured at 30 MPa. The σ^{P-M} and σ^{M-P} values are both lower at 40 MPa and 20 MPa respectively, in the second strain cycle. Figure 3.6 shows the hysteresis curves for sample ASC2 which was strain cycled to 0.8% strain following strain cycling to 0.5%. Once again a small residual strain remains after the first cycle but in the subsequent cycles no residual strain is observed. The σ^{P-M} and σ^{M-P} values are 32 MPa and 28 MPa respectively in the first cycle to 0.8%, however, they decrease to 30 MPa and 24 MPa in the second cycle. The hysteresis curves show the superelastic behavior of the austenitic CuZnAl alloy. The area enclosed by the loading and unloading curves is a measure of the energy dissipation which accompanies the creation and annihilation of stress-induced martensite. It is evident from Figures 3.4, 3.5 and 3.6 that the area within the hysteresis loops decrease with increasing number of strain cycles. This is due to the decrease in transformation stress levels with increasing number of strain cycles. This is an indication that there could be a degradation of the superelastic property with increasing number of strain cycles.

The stress-strain curves from the stress cycling experiments of the martensitic CuZnAl alloy (samples MSC1, MSC2 and MSC3) are shown in Figures 3.7 - 3.9. The martensitic alloy was stress cycled rather than strain cycled because the strain recovery with each strain cycle was very small compared to the austenitic alloy. Unlike the austenitic CuZnAl samples, the residual strain in the first cycle is much larger. In subsequent stress cycles there is complete strain recovery due to the reorientation of martensite.

3.3 Low-Cycle Fatigue Tests

The data recorded during these tests include the total axial strain amplitude, ε_a,

the stress range, $\Delta\sigma$, and the number of cycles to failure, N_f. The total axial strain amplitude can be expressed as

$$\varepsilon_a = \frac{\Delta\varepsilon_t}{2} \tag{3.1}$$

where $\Delta\varepsilon_t$ = total strain range.

The total axial strain amplitude can be further broken down into its separate elastic and plastic components:

$$\frac{\Delta\varepsilon_t}{2} = \frac{\Delta\varepsilon_e}{2} + \frac{\Delta\varepsilon_p}{2} \tag{3.2}$$

where: $\Delta\varepsilon_e$ = elastic-strain range

$\Delta\varepsilon_p$ = plastic-strain range

Using Hooke's law, the elastic-strain range, $\Delta\varepsilon_e$, can be calculated by the relationship

$$\Delta\varepsilon_e = \frac{\Delta\sigma}{E} \tag{3.3}$$

Using the result of equation 3.3, the total axial strain amplitude can be expressed as

$$\frac{\Delta\varepsilon_t}{2} = \frac{\Delta\sigma}{2E} + \frac{\Delta\varepsilon_p}{2} \tag{3.4}$$

where E is the modulus of elasticity. By rearranging equation 3.4, the plastic strain amplitude can be calculated as follows:

$$\frac{\Delta\varepsilon_p}{2} = \frac{\Delta\varepsilon_t}{2} - \frac{\Delta\sigma}{2E} \tag{3.5}$$

Modulus of elasticity values used in the calculation of the plastic strain amplitude were measured before the start of each LCF test by the LCF test machine and are given in Tables 3.2 and 3.4. The LCF test machine measured the modulus of elasticity values by

applying a cyclic load of 500 N to each sample. The low-cycle fatigue results for the austenitic CuZnAl are shown in Table 3.6. Samples were successfully tested between total strain amplitudes of 0.3% and 1%. Specimen buckling occurred when a strain amplitude of 2% was applied due to specimen slenderness. Sample ALCF3 was not tested to failure. It was tested up to 48001 cycles which was very much greater than LCF region $\left(N_f < 10^4\right)$ (ASM Handbook, 1992). The LCF test results for the martensitic CuZnAl alloy are summarized in Table 3.7. In the case of the martensitic alloys, tests were carried out with strain amplitudes of up to 1%. Tests with higher strain amplitudes were not successful due to specimen buckling. The calculated LCF parameters for the austenitic and martensitic CuZnAl alloys are given in Tables 3.8 and 3.9 respectively and the hysteresis curves of the samples at half-life are shown in Appendix B. The average stress amplitude for sample ALCF6 obtained from the LCF software program appears to be incorrect. For this reason, sample ALCF6 is left out of computations involving the stress amplitude. However, sample ALCF6 follows the strain-life trend set by the other samples, as shown in Figure 3.18. For this reason it was decided to include sample ALCF6 in the strain-life analysis.

The cyclic stress response curves for austenitic and martensitic CuZnAl are shown in Figures 3.10 and 3.11 respectively. The average stress amplitude, $\frac{\Delta\sigma}{2}$, of each cycle is plotted against the number of cycles to failure. At all strain levels tested, the austenitic CuZnAl shows cyclic hardening within the first 10 cycles. Following the hardening during the first few cycles, the alloy shows cyclic stability up to fracture. The martensitic CuZnAl samples showed gradual cyclic hardening up to the point of fracture. The degree of hardening at any particular strain amplitude, $H_{\Delta\varepsilon_t/2}$, was calculated using the following relationship (Prasad et al., 1996):

$$H_{\Delta\varepsilon_t/2} = \frac{(\Delta\sigma/2)_m - (\Delta\sigma/2)_1}{(\Delta\sigma/2)_1} \times 100 \qquad (3.6)$$

For the austenitic CuZnAl alloy, $(\Delta\sigma/2)_1$ is taken as the average stress amplitude of the

first cycle and $(\Delta\sigma/2)_m$ as the average stress amplitude level attained after initial hardening. In the case of martensitic CuZnAl, $(\Delta\sigma/2)_m$ is the average stress amplitude level just before fracture and $(\Delta\sigma/2)_1$ is taken as the average stress amplitude of the first cycle. The degree of hardening for both materials are included in Tables 3.8 and 3.9. The austenitic alloy shows a moderate cyclic hardening of 9.5 - 18.6% with the degree of hardening increasing with increased total strain amplitude. The extent of cyclic hardening in the martensitic alloy was large and varied, from 33% to 176%. The cyclic hardening of 176% was observed in sample MLCF2 which was tested at a total strain amplitude of 0.5%. However, sample MLCF1 which was also tested at a total strain amplitude of 0.5%, hardened by 50%. Excluding the cyclic hardening of sample MLCF2, it is observed that, for martensitic CuZnAl cyclic hardening decreases with increasing total strain amplitude, which is in contrast to the cyclic hardening behavior exhibited by austenitic CuZnAl.

The cyclic stress-strain data of both alloys are analyzed in terms of the power law relationship

$$(\Delta\sigma/2)_{0.5N_f} = K'(\Delta\varepsilon_p/2)_{0.5N_f}^{n'} \tag{3.7}$$

where $(\Delta\sigma/2)_{0.5N_f}$ and $(\Delta\varepsilon_p/2)_{0.5N_f}$ are the cyclic stress and plastic strain amplitudes at half life, K' is the cyclic strength coefficient, and n' is the cyclic work hardening exponent. The stress amplitude, $(\Delta\sigma/2)_{0.5N_f}$, and plastic strain amplitude, $(\Delta\varepsilon_p/2)_{0.5N_f}$, are plotted logarithmically in Figures 3.12 and 3.13. Lines are drawn through the data points using regression analysis to determine the values of the cyclic stress-strain constants. The values of K' and n' derived from the analysis are tabulated in Table 3.10. The cyclic strength coefficient and cyclic work hardening exponent of the austenitic CuZnAl alloy is shown to be twice that of the martensitic alloy. For both materials, the cyclic strain hardening exponent falls in the range, 0.10 - 0.25, reported for most metals (Bannantine et al., 1990).

It was shown in equation (3.4) that the total axial strain amplitude can be expressed in terms of the elastic and plastic strain amplitudes. The elastic and plastic strain ampli-

tudes can be simplified further using the Coffin-Manson law and Basquin relationship respectively. The Coffin-Manson law is an empirical relation showing that the plastic strain amplitude - number of reversals ($\frac{\Delta\varepsilon_p}{2}$-$2N_f$) data can be linearized on log-log coordinates. The Coffin-Manson law can be expressed as:

$$\frac{\Delta\varepsilon_p}{2} = \varepsilon_f'(2N_f)^c \tag{3.8}$$

where $\frac{\Delta\varepsilon_p}{2}$ is the plastic strain amplitude, $2N_f$ is the number of reversals to failure, ε_f' is the fatigue ductility coefficient and c is the fatigue ductility exponent. The fatigue ductility coefficient and the fatigue ductility exponent are considered to be fatigue properties of a material. The fatigue ductility coefficient and the fatigue ductility exponent are respectively the intercept on the plastic strain amplitude axis at $2N_f$=1, and the slope of the best fit line on a plot of the plastic strain amplitude as a function of the number of reversals to failure. For most metals, the fatigue ductility coefficient is approximately equal to true fracture ductility, ε_f, while the fatigue ductility exponent, c, varies between -0.5 to -0.7 (Bannantine et al., 1990). The Basquin relationship is an empirical relationship showing that the stress amplitude at half life - number of reversals to failure ($\left(\frac{\Delta\sigma}{2}\right)_{0.5N_f}$-$2N_f$) can be linearized on log-log coordinates. The Basquin relationship can be expressed as:

$$\left(\frac{\Delta\sigma}{2}\right)_{0.5N_f} = \sigma'_f(2N_f)^b \tag{3.9}$$

where σ'_f is the fatigue strength coefficient and b is the fatigue strength exponent (Basquin's exponent). The fatigue strength coefficient and the fatigue strength exponent are considered to be fatigue properties of a material. σ'_f and b are respectively the intercept on the stress amplitude at half life axis at $2N_f$=1, and the slope of the best fit line on a plot of the stress amplitude as a function of the number of reversals to failure. For most metals, the fatigue strength coefficient is approximately equal to true fracture strength, σ_f,

while the fatigue strength exponent, b, varies between -0.05 and -0.12 (Bannantine et al., 1990). Substituting the results of the Coffin-Manson law and Basquin relationship into equation (3.4), the total strain amplitude, $\frac{\Delta\varepsilon_t}{2}$, can be expressed as:

$$\frac{\Delta\varepsilon_t}{2} = \sigma'_f(2N_f)^b + \varepsilon_f'(2N_f)^c \tag{3.10}$$

Coffin-Manson plots for austenitic and martensitic CuZnAl are shown on Figure 3.14 and 3.15 respectively. The values of ε_f' and c are given in Table 3.11. The value of ε_f' for austenitic CuZnAl is higher than ε_f obtained from the tension tests. The fatigue ductility exponent, c, for austenitic CuZnAl is -0.59 and falls within the range of values reported for normal metals, i.e. $-0.5 < c < -0.7$ (Bannantine et al., 1990). For martensitic CuZnAl, the fatigue ductility coefficient and fatigue ductility exponent are determined to be 5.29 and -0.93 respectively. The value of ε_f' is much higher than ε_f and the value of c, -0.93, is lower than the value reported for most metals.

The $\left(\frac{\Delta\sigma}{2}\right)_{0.5N_f}$-$2N_f$ (Basquin relationship) plots for austenitic and martensitic CuZnAl are shown in Figures 3.16 and 3.17 respectively. The line through the data in both plots is obtained by linear regression analysis. Values of σ'_f and b determined using equation (3.8) for both alloys are tabulated in Table 3.11. The fatigue strength coefficient, σ'_f, of austenitic CuZnAl is almost double the value of σ_f measured during monotonic tensile tests while the value of b is in the higher end of the range reported for most metals, i.e. $-0.05 < b < -0.12$. In the case of martensitic CuZnAl, the value of σ'_f is much closer to the value of σ_f and the value of b is also in the higher end of the range reported for most metals. Values of K' and n' were also derived from the following relationships

$$K' = \frac{\sigma'_f}{(\varepsilon'_f)^{b/c}} \tag{3.11}$$

$$n' = \frac{b}{c} \tag{3.12}$$

and are included in Table 3.10. These values are in good agreement with those derived using equation (3.6).

$\frac{\Delta\varepsilon_t}{2}$-$2N_f$ plots for austenitic and martensitic CuZnAl are shown in Figures 3.18 and 3.19 respectively. The lines through the data points is the best fit line drawn through the average values of $2N_f$ for each total strain amplitude value.

3.4 High-Cycle Fatigue Tests

The results of the HCF test program for austenitic CuZnAl alloys are shown in Table 3.12 and the S-N curve shown in Figure 3.21. The data in Figure 3.21 is fitted with a line using regression analysis. Sample AHCF3 is not included in the analysis. At a stress amplitude of 300 MPa, sample AHCF3 showed a considerable amount of plastic strain (see stress-strain curves shown in Appendix C) and failed in less than 10000 cycles and therefore was excluded from the HCF analysis. In the regression analysis to determine the best fit line, the stress amplitude is treated as the independent variable and the cycles to failure, N, as the independent variable. The line obtained by regression analysis can be expressed by the following equation:

$$\log N = 15.524 - 4.358 \log \sigma_a \qquad ,r^2 = 0.9418 \tag{3.13}$$

where r is the correlation coefficient. The fracture surface of sample AHCF1 is shown in Figure 3.29.

The HCF test results for the martensitic CuZnAl alloy are presented in Table 3.13 with the samples in the order that they were tested. The first sample, MHCF1, was tested at a stress amplitude of 200 MPa. The test had to be stopped after the completion of 163,566 cycles as the specimen failed at the bottom threaded grip section. Then sample MHCF2 was tested at 200 MPa. Once again the test had to be stopped after 225,054 cycles due to failure of the specimen at the top threaded grip section. Following these failures in

the threaded grip sections, it was decided to redesign the test specimens as it was suspected that the threaded section root cross-sectional area to gage section cross-sectional area was not large enough to induce fracture in the gage section of the fatigue specimens. The specimen gauge diameter was reduced to 3.75 mm resulting in a threaded section root cross-sectional area to gage section cross-sectional area ratio of 1.75. The original specimen design resulted in a threaded section root area to gage area ratio of 1.5. The redesigned specimens didn't necessarily solve the problem as five of the redesigned specimens failed in the threaded section while only four redesigned specimens failed in the gage section as desired. Another reason for the failures in the threaded section could be as a result of re-threading of the specimens several times unlike the austenitic high-cycle fatigue specimens. The re-threading was needed following heat treatment and after gage diameter reduction. The re-threading could have led to narrowing of the cross-section (by cutting into the material) at the grip section, resulting in stress concentrations in the threaded sections of the specimens. The S-N curve for the martensitic CuZnAl alloy is shown in Figure 3.22. Samples MHCF7 and MHCF8 are excluded from the analysis as they experienced large amounts of plastic strain as evidenced from the stress-strain curves shown in Appendix C. Once again, in obtaining the best fit line, the stress amplitude is treated as the independent variable and the cycles to failure, N, as the independent variable. The line obtained by regression analysis can be expressed by the following equation:

$$\log N = 18.052 - 5.423 \log \sigma_a \qquad ,r^2 = 0.84 \tag{3.14}$$

where r is the correlation coefficient. The fracture surface of sample MHCF4 is shown in Figure 3.30.

The fatigue strength at $N = 10^6$ of austenitic and martensitic alloys are calculated to be 153 and 167 MPa respectively. These values are very much less than the 270 MPa reported for CuZnAl (AMT, 1995). As expected, Figure 3.23 clearly shows the superior fatigue properties of the martensitic CuZnAl alloy over the austenitic alloy at all stress levels tested except at stress levels between 200 and 275 MPa. This is because the curves compared in Figure 3.23 are the average values of the test results. Comparison of the test data in Tables 3.10 and 3.11 indicate that some of the martensitic samples had superior

fatigue properties in the stress range between 200 and 275 MPa. Also, premature failure took place in most of the martensitic HCF samples when they failed in the threaded section. The HCF fatigue properties of austenitic and martensitic CuZnAl are also compared to those of 1045 steel and 2024-T4 aluminum in Figure 3.23. The 1045 steel and 2024-T4 aluminum have much better fatigue behavior than both CuZnAl alloys. The short fatigue lives of austenitic and martensitic CuZnAl could be the result of inter-granular cracking (Melton et al., 1979) or residual deformation resulting from the martensite reorientation and reversion (Delaey et al., 1979).

3.5 Material Damping Properties

The specific damping capacity, D, and loss coefficient, η, due to plastic deformation and superelasticity were quantified using the methods described in Section 2.3.5 and Appendix D. The hysteresis curves for quantifying damping due to plastic deformation were obtained from the LCF tests and are given in Appendix B. Damping due to superelastic CuZnAl was quantified from the hysteresis curves generated during the strain cycling experiments of austenitic CuZnAl. These curves are given in Figures 3.4 - 3.6. The calculated values of D and η are tabulated in Tables 3.14 - 3.16. The loss coefficient due to plastic deformation is plotted as a function of the strain amplitude for austenitic and martensitic CuZnAl in Figure 3.24. They both exhibit a non-linear increase in damping with increasing total strain amplitude. Austenitic CuZnAl shows a 40% higher loss coefficient due to plastic deformation compared to the martensitic alloy at a total strain amplitude of 1%. The loss coefficient, due to superelastic behavior of austenitic CuZnAl, as a function of the cycling strain is shown in Figure 3.25. A non-linear increase in the loss coefficient with increasing cycling strain is observed. A comparison of the loss coefficients due to superelasticity with loss coefficients due to plastic deformation, shows that the damping due to superelasticity is about 5 times smaller. However, the exploitation of damping associated with plastic deformation is restricted by the short fatigue lives resulting from the corresponding non-recoverable plastic deformation.

Sample	$\dot{\varepsilon}$, (S^{-1})	S_u (MPa)	e_f (%)
AT1	5.75×10^{-5}	395	6.48
AT3*	1.0×10^{-4}	> 427	> 8.6
AT4	2.0×10^{-4}	385	9.5
AT2	4.0×10^{-4}	351	2.76

* Specimen not tested to failure

Table 3.1: Summary of austenitic CuZnAl tensile test results

Sample	E, (MPa)
ALCF2	120000
ALCF3	120000
ALCF4	120000
ALCF5	120000
ALCF6	120000

Table 3.2: Modulus of elasticity of austenitic CuZnAl measured during the LCF tests

Sample	$\dot{\varepsilon}$, (S^{-1})	S_u (MPa)	e_f (%)
MT1	2.0×10^{-4}	660	2.8
MT2	2.0×10^{-4}	548	2.14
MT3	2.0×10^{-4}	656	2.48

Table 3.3: Summary of martensitic tensile test results

Sample	E, (MPa)
MLCF1	50000
MLCF2	90000
MLCF7	100000
MLCF8	90000
MLCF9	90000

Table 3.4: Modulus of elasticity of martensitic CuZnAl measured during the LCF tests

Material (Sample)	S_u (MPa)	e_f (%)	E (MPa)
Austenitic CZA (AT3)	> 427	> 8.6	120000
Martensitic CZA (MT1)	660	2.8	90000

Table 3.5: Comparison of austenitic and martensitic material properties

Sample	$\frac{\Delta\varepsilon_t}{2}$,%	N_f
ALCF2	0.5	3663
ALCF3	0.3	48001*
ALCF4	1	425
ALCF5	0.5	8491
ALCF6	0.75	1099

* Specimen did not fail, test stopped

Table 3.6: Summary of LCF test results for austenitic CuZnAl

Sample	$\frac{\Delta\varepsilon_t}{2}$,%	N_f
MLCF1	0.5	2713
MLCF2	0.5	6504
MLCF7	0.3	44557
MLCF8	1	1142
MLCF9	1	779

Table 3.7: Summary of LCF test results for martensitic CuZnAl

Sample	$\frac{\Delta\varepsilon_t}{2}$,%	$\left(\frac{\Delta\sigma}{2}\right)_{0.5N_f}$, MPa	$\frac{\Delta\varepsilon_p}{2}$,%	$H_{\Delta\varepsilon_t/2}$,%	$2N_f$
ALCF3	0.3005	299.70	0.0335	9.5	96002
ALCF2	0.501	441.25	0.1465	10.3	7326
ALCF5	0.501	436.77	0.149	15.1	16982
ALCF6	0.752	296.31	0.4145	-	2198
ALCF4	1.0015	532.01	0.577	18.6	850

Table 3.8: Austenitic CuZnAl low-cycle fatigue cyclic data

Sample	$\frac{\Delta\varepsilon_t}{2}$, %	$\left(\frac{\Delta\sigma}{2}\right)_{0.5N_f}$, MPa	$\frac{\Delta\varepsilon_p}{2}$, %	$H_{\Delta\varepsilon_t/2}$, %	$2N_f$
MLCF7	0.3	301.01	0.0125	89	89114
MLCF1	0.5035	365.25	0.135	50.2	5426
MLCF2	0.5035	441.11	0.0915	176	13008
MLCF8	1.0	519.52	0.497	46	2284
MLCF9	1.003	464.82	0.499	33	1558

Table 3.9: Martensitic CuZnAl low-cycle fatigue cyclic data

	Cyclic stress-strain constants [equation (3.6)]		Cyclic stress-strain constants [equation (3.9)]	
Material	K', MPa	n'	K', MPa	n'
Austenitic CuZnAl	1580	0.203	1488	0.197
Martensitic CuZnAl	961	0.128	915	0.118

Table 3.10: Cyclic stress-strain constants of CuZnAl alloys

Material	Fatigue ductility constants [equation (3.7)]		Fatigue strength constants [equation (3.8)]	
	ε'_f $(\varepsilon_f)^*$	c	σ'_f, MPa	b
Austenitic CuZnAl	0.36 (0.12)	-0.59	1218	-0.116
Martensitic CuZnAl	5.29 (0.04)	-0.93	1114	-0.11

* ε_f true strain to fracture under monotonic tensile loading.

Table 3.11: Fatigue life constants of CuZnAl alloys

Sample	σ_a, MPa	N_f
AHCF1	200	289548
AHCF3	300	245
AHCF4	250	168119
AHCF5	275	52068
AHCF6	150	1082451
AHCF7	275	90736

Table 3.12: Summary of HCF results for austenitic CuZnAl

Sample	Diameter(mm)	σ_a, MPa	N_f
MHCF1	4.11	200	163566*
MHCF2	4.09	200	225054*
MHCF6	4.05	200	276470*
MHCF3	3.74	150	2550995*
MHCF4	3.49	250	168400
MHCF5	3.73	250	152741*
MHCF7	3.71	300	28849
MHCF8	3.73	300	18390
MHCF9	3.77	200	447684*
MHCF10	3.80	250	213355*
MHCF11	3.75	275	159928
MHCF12	3.67	150	1816538*

* specimen failed in the threaded grip section

Table 3.13: Summary of HCF test results for martensitic CuZnAl

Sample	$\frac{\Delta\varepsilon_t}{2}$,%	D, $(10^6)\frac{N \cdot m}{m^3}$	η
ALCF3	0.3005	0.097	0.035
ALCF2	0.501	1.12	0.13
ALCF5	0.501	1.26	0.16
ALCF6	0.752	1.63	0.246
ALCF4	1.0015	5.97	0.326

Table 3.14: Damping properties of austenitic CuZnAl via LCF testing

Sample	$\frac{\Delta\varepsilon_t}{2}$,%	D, $(10^6)\frac{N \cdot m}{m^3}$	η
MLCF7	0.3	0.076	0.027
MLCF1	0.5035	0.785	0.124
MLCF2	0.5035	0.761	0.115
MLCF8	1.0	3.87	0.242
MLCF9	1.003	3.41	0.24

Table 3.15: Damping properties of martensitic CuZnAl via LCF testing

Sample	Cycling Strain,%	D, $(10^6)\frac{N \cdot m}{m^3}$	η
ASC2	0.5	0.11	0.04
ASC2	0.8	0.26	0.055
ASC1	1.0	0.42	0.06

Table 3.16: Damping properties of superealstic CuZnAl

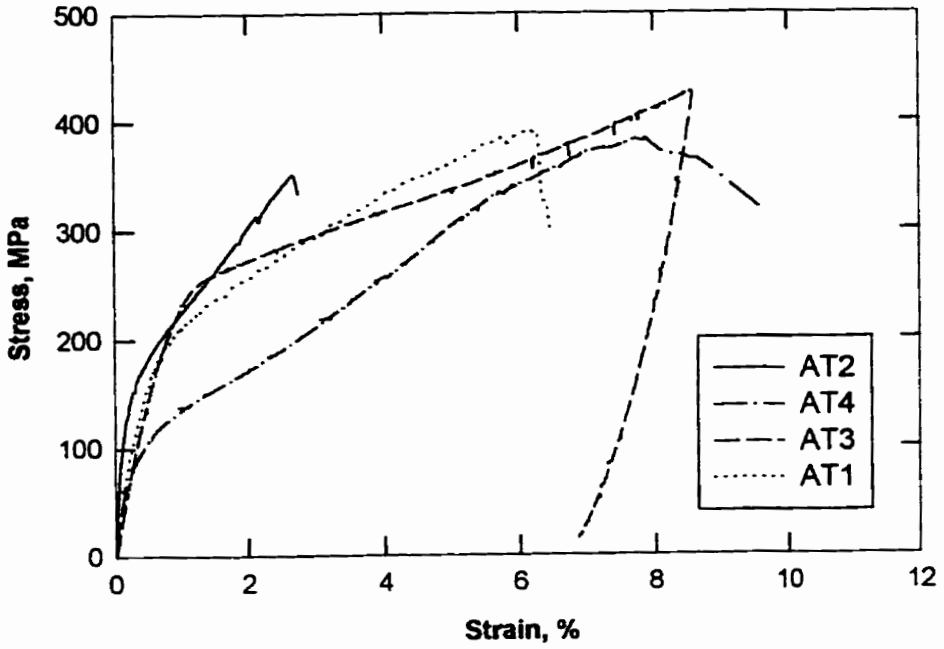

Figure 3.1: Stress-strain curves of austenitic CuZnAl

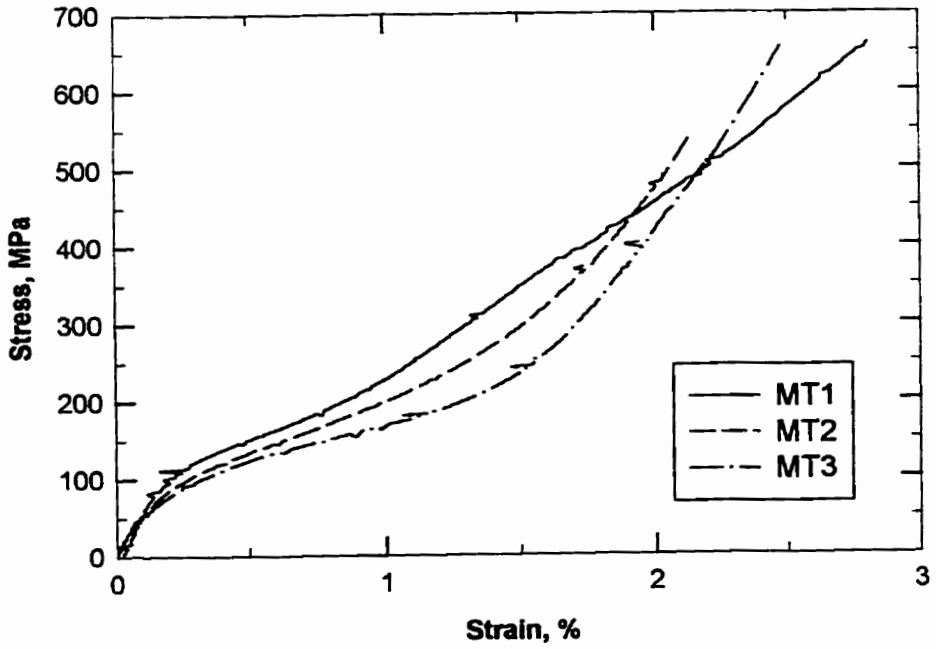

Figure 3.2: Stress-strain curves of martensitic CuZnAl

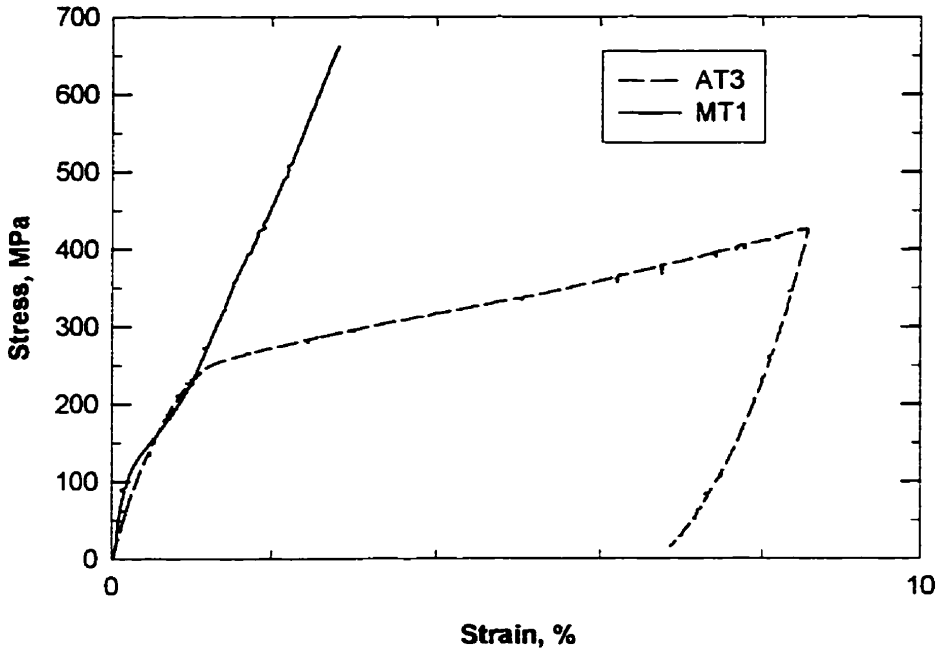

Figure 3.3: Stress-strain curves austenitic and martensitic CuZnAl

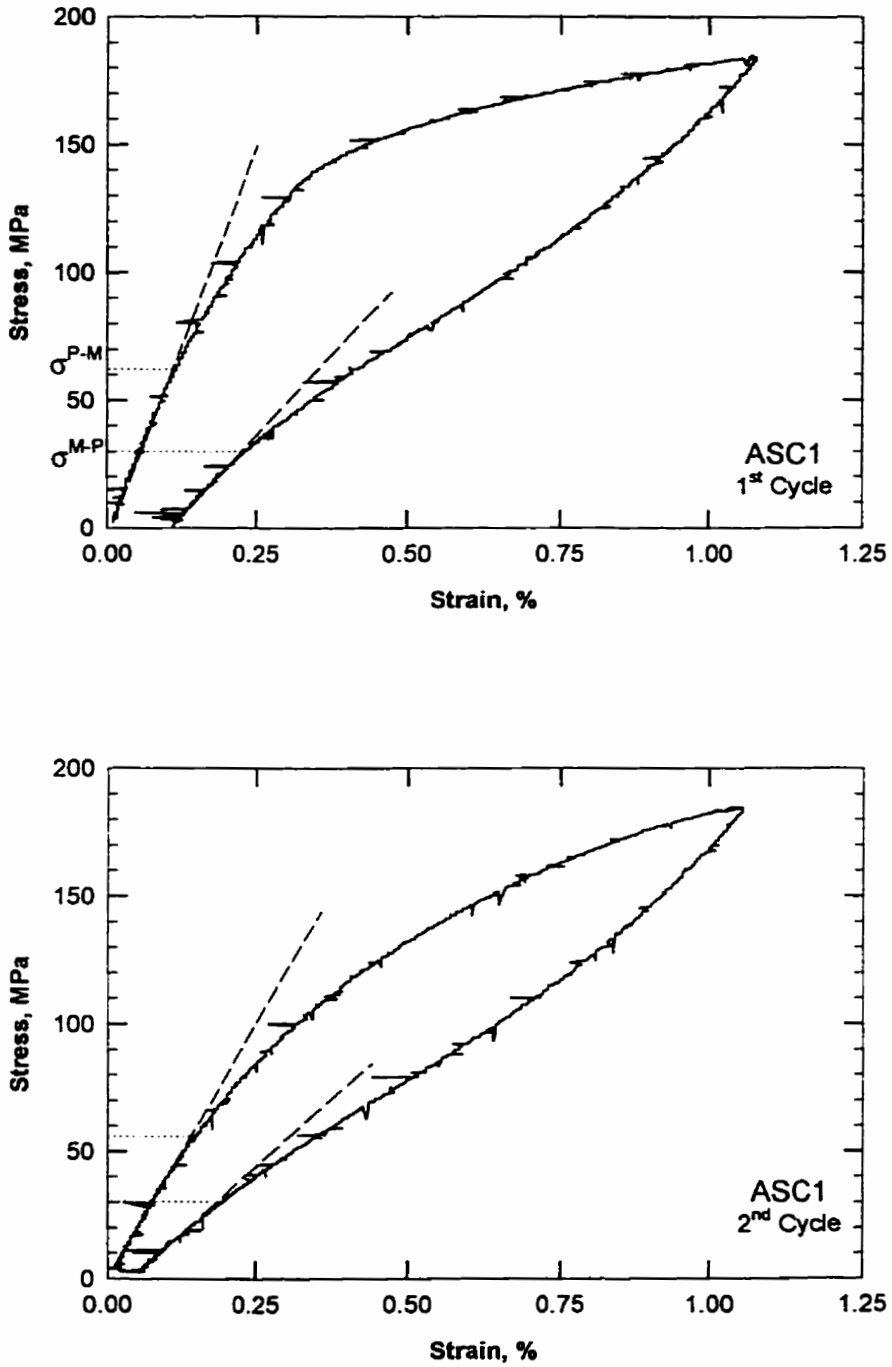

Figure 3.4: Two strain cycles to 1.0% strain for austenitic CuZnAl showing superelastic behavior (sample ASC1)

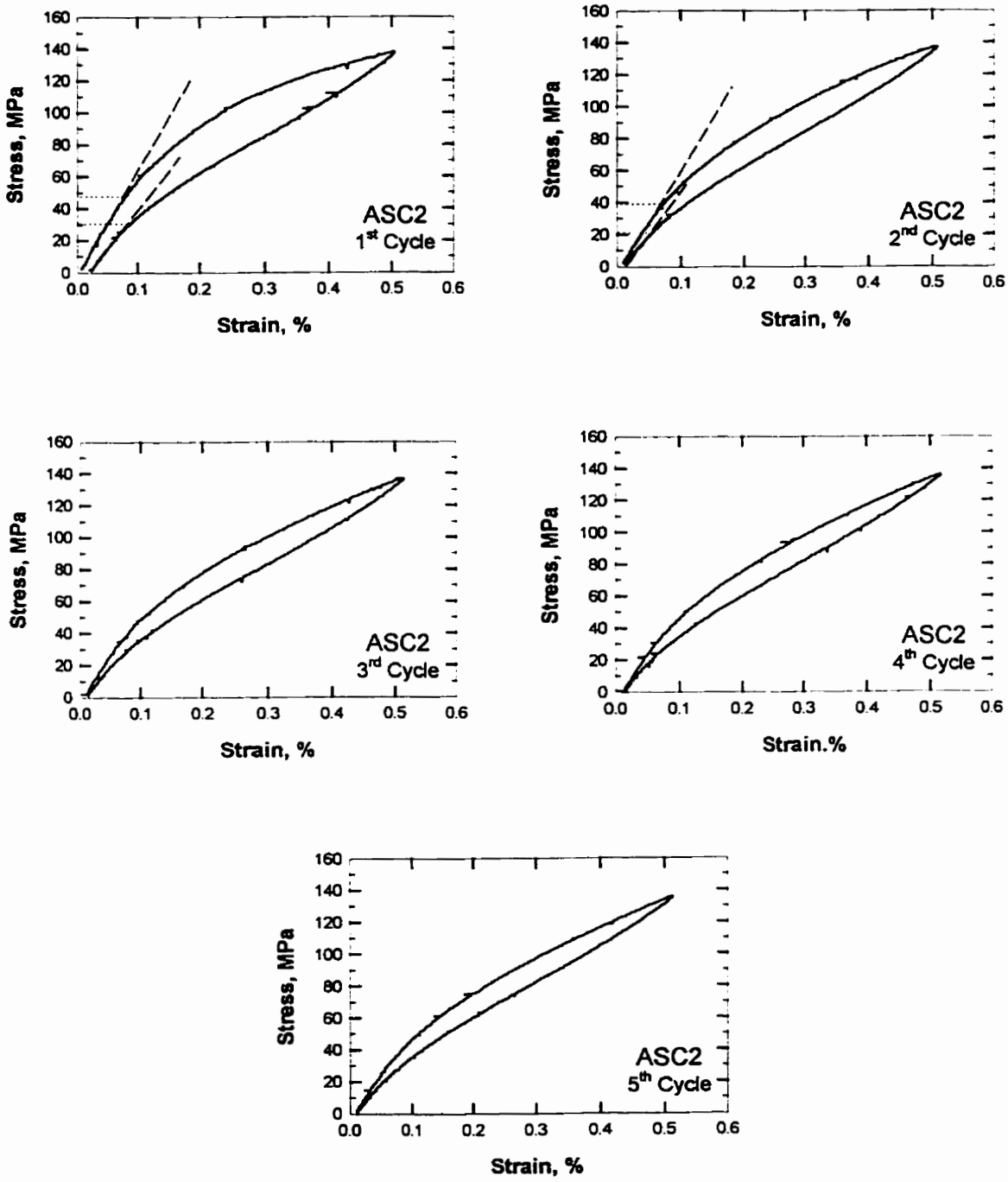

Figure 3.5: Five strain cycles to 0.5% strain for austenitic CuZnAl showing superelastic behavior (sample ASC2)

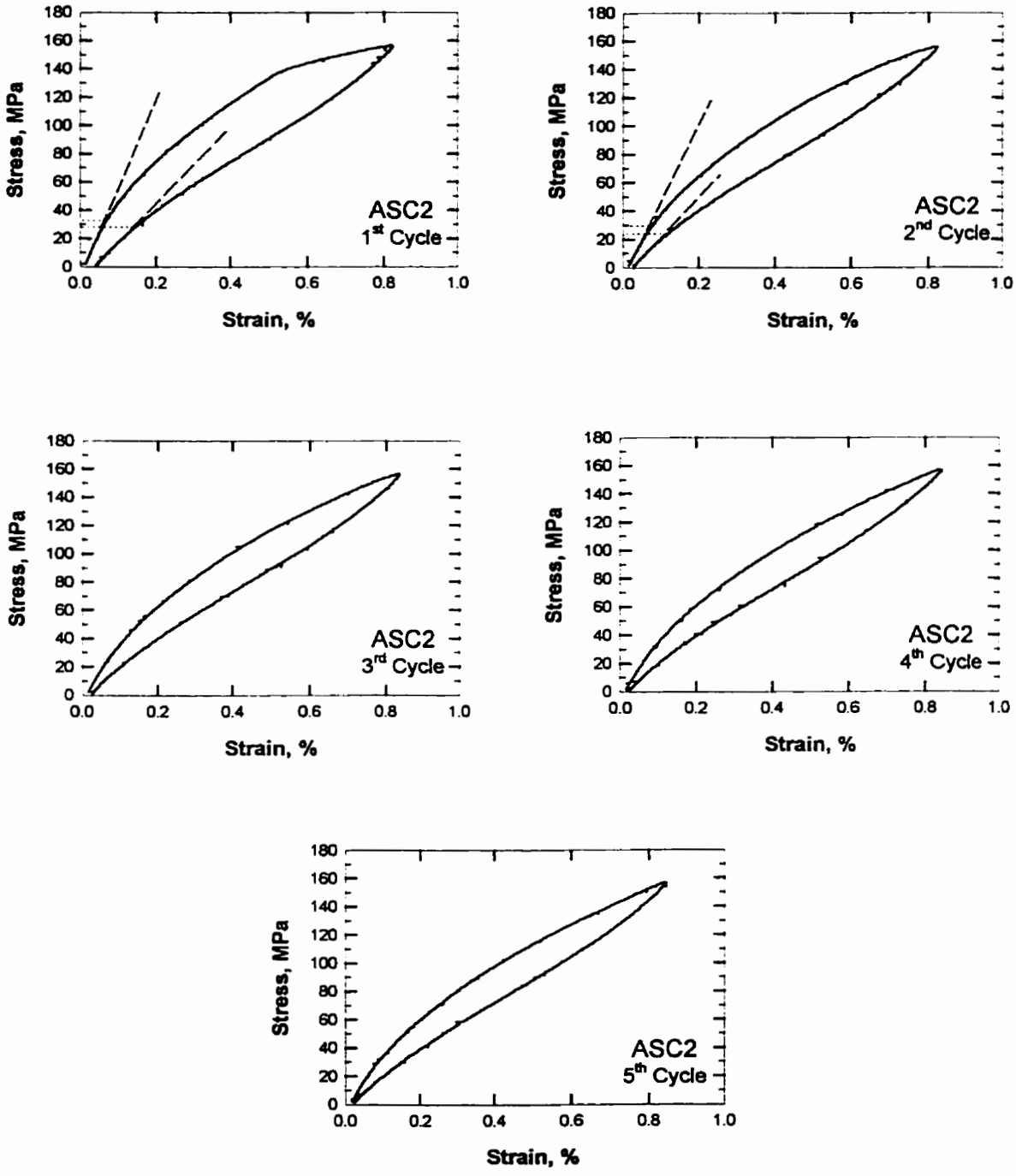

Figure 3.6: Five strain cycles to 0.8% strain for austenitic CuZnAl showing superelastic behavior (sample ASC2)

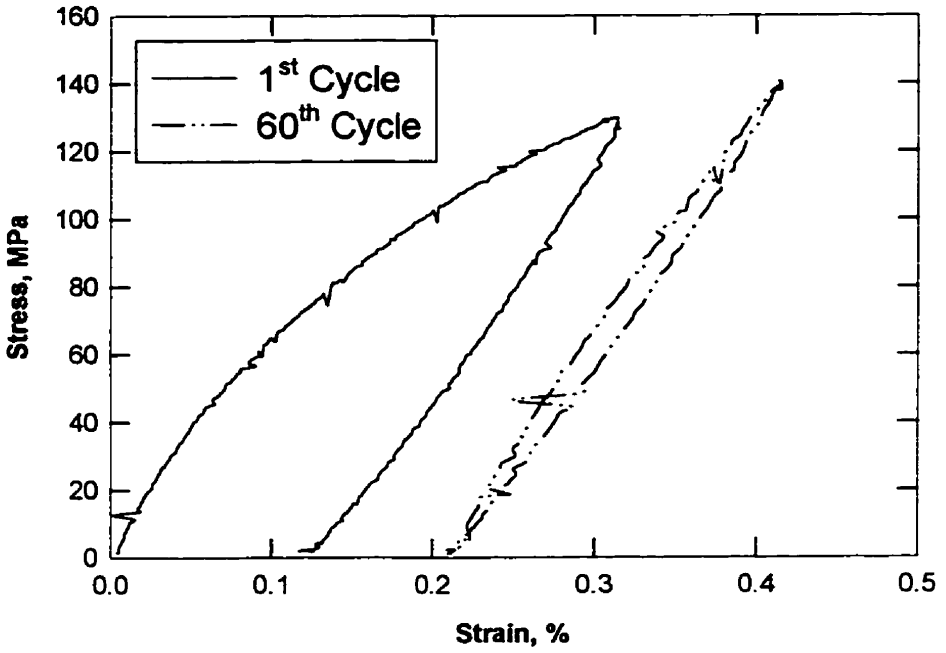

Figure 3.7: Strain cycling to 0.3% followed by stress cycling, martensitic CuZnAl (sample MSC1)

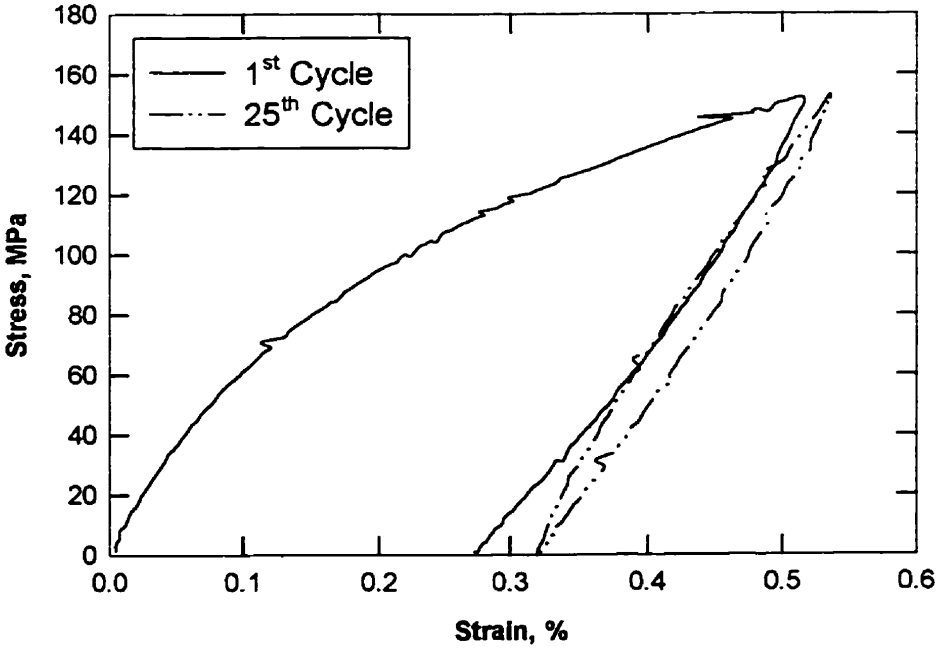

Figure 3.8: Strain cycling to 0.5% followed by stress cycling, martensitic CuZnAl (sample MSC2)

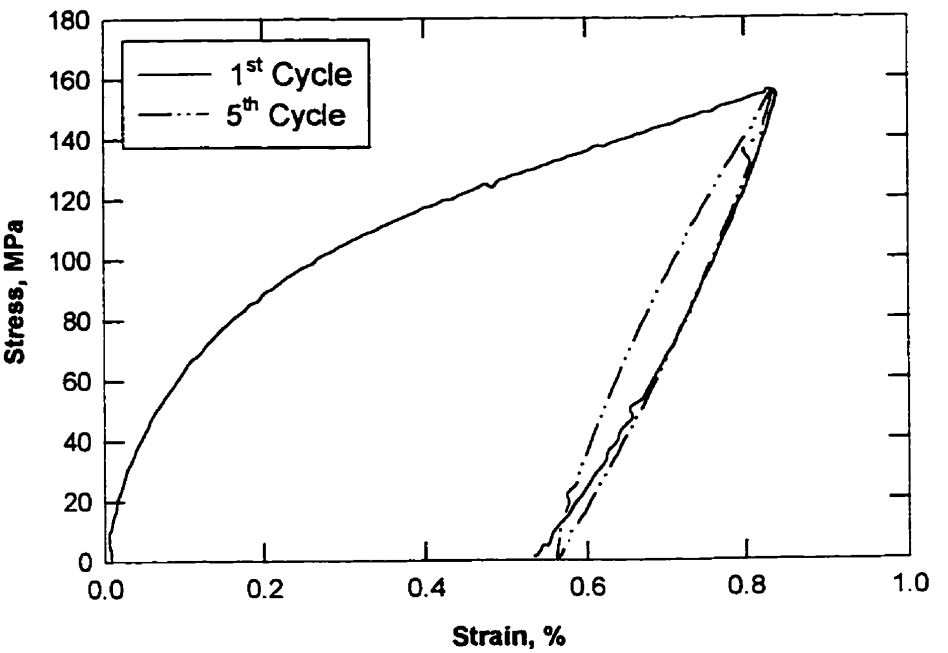

Figure 3.9: Strain cycling to 0.8% followed by stress cycling, martensitic CuZnAl (sample MSC3)

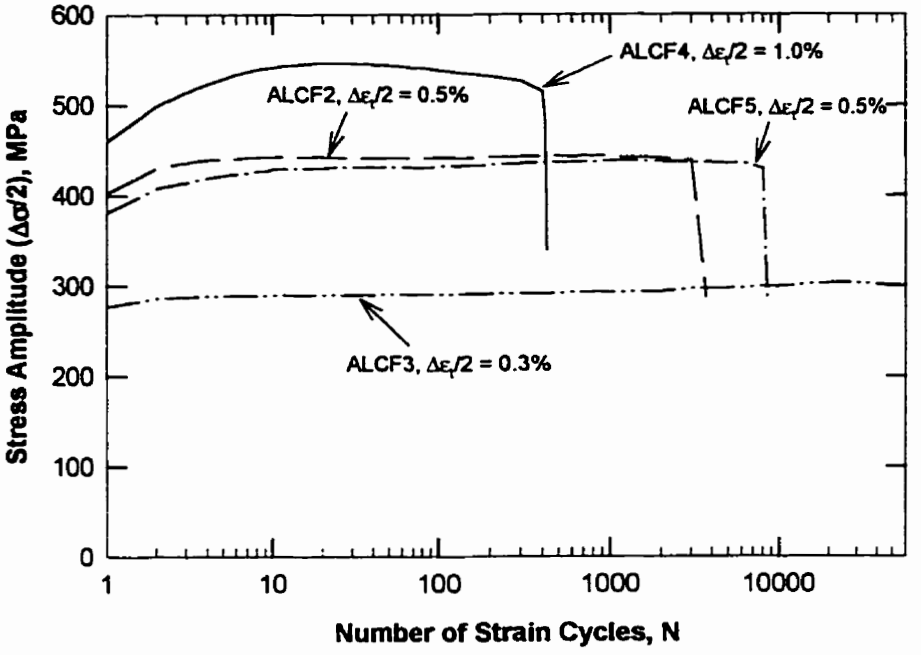

Figure 3.10: Cyclic stress response curves of austenitic CuZnAl showing variation of $\Delta\sigma/2$ with the number of strain cycles

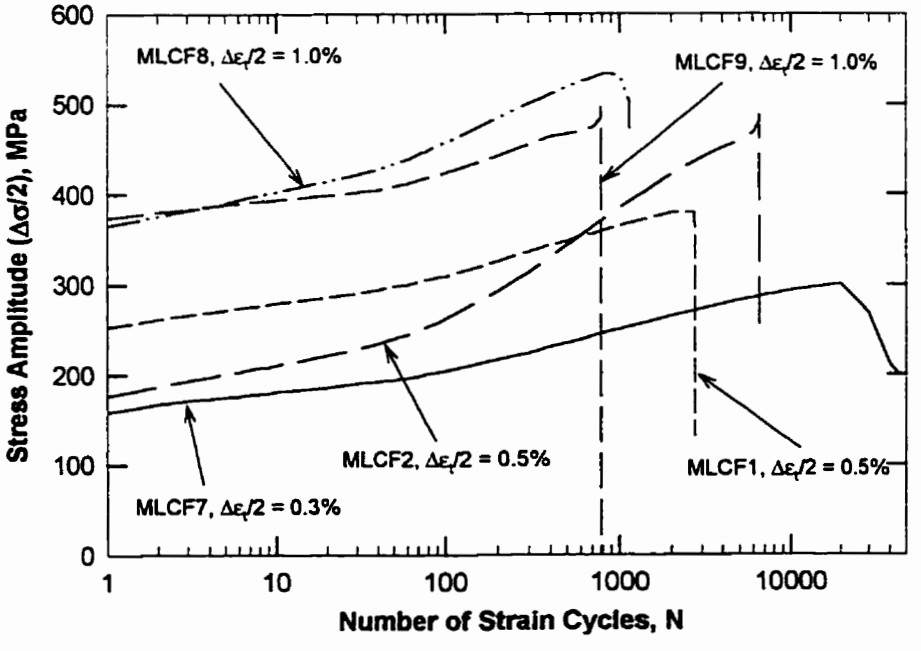

Figure 3.11: Cyclic stress response curves of martensitic CuZnAl showing variation of $\Delta\sigma/2$ with the number of strain cycles

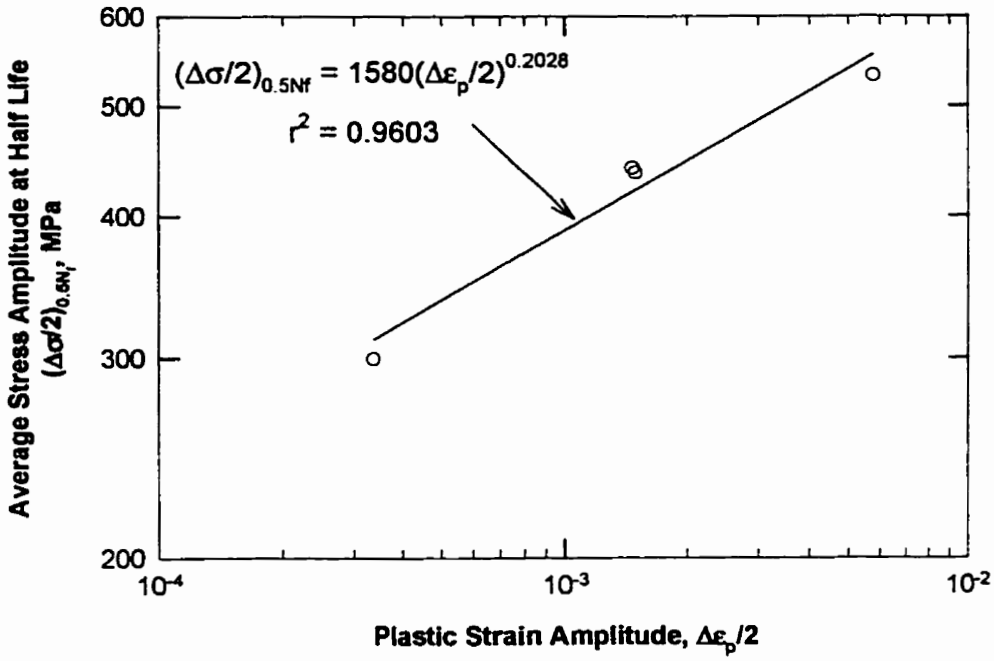

Figure 3.12: Variation of the average stress amplitude at half life with corresponding plastic strain for austenitic CuZnAl

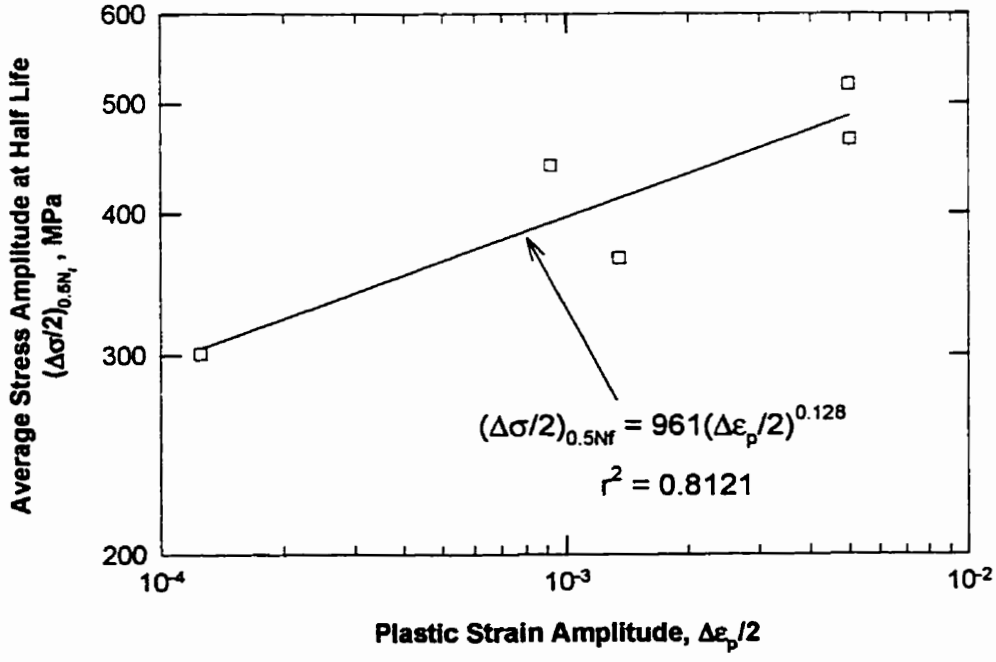

Figure 3.13: Variation of the average stress amplitude at half life with corresponding plastic strain for martensitic CuZnAl

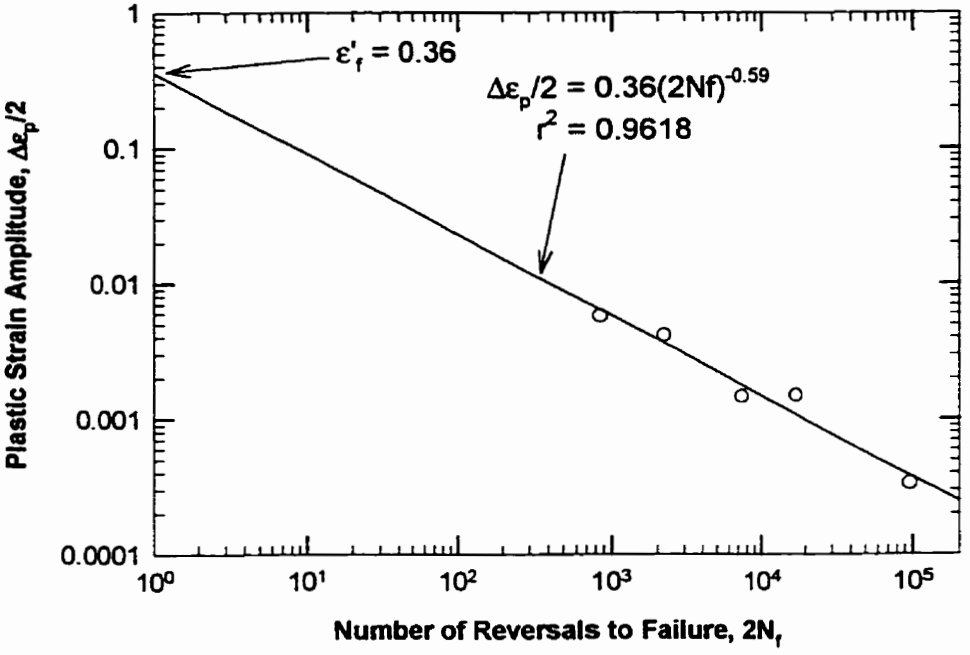

Figure 3.14: Coffin-Manson plot of austenitic CuZnAl

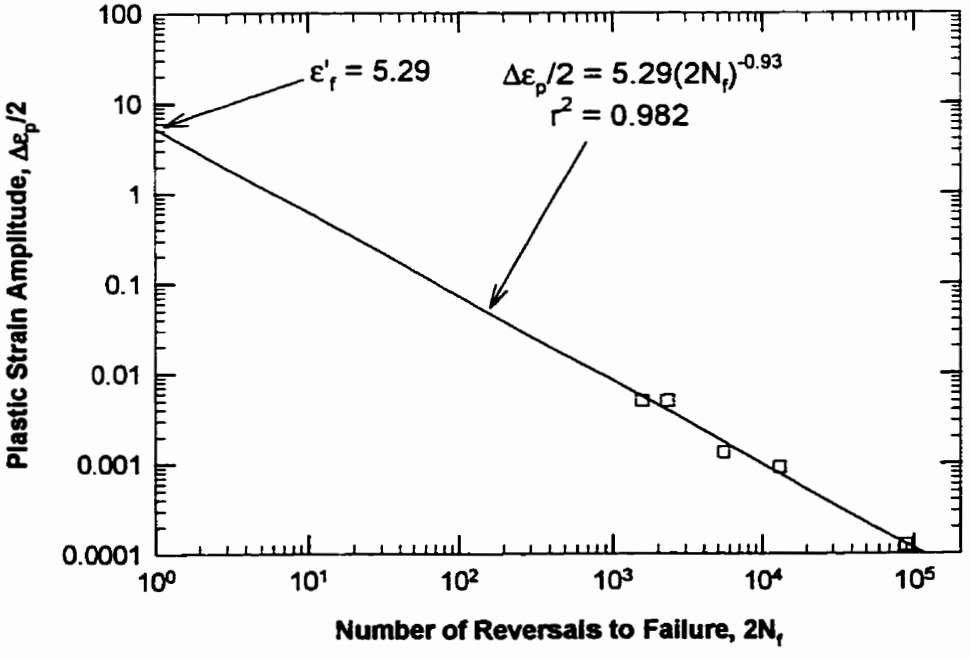

Figure 3.15: Coffin-Manson plot of martensitic CuZnAl

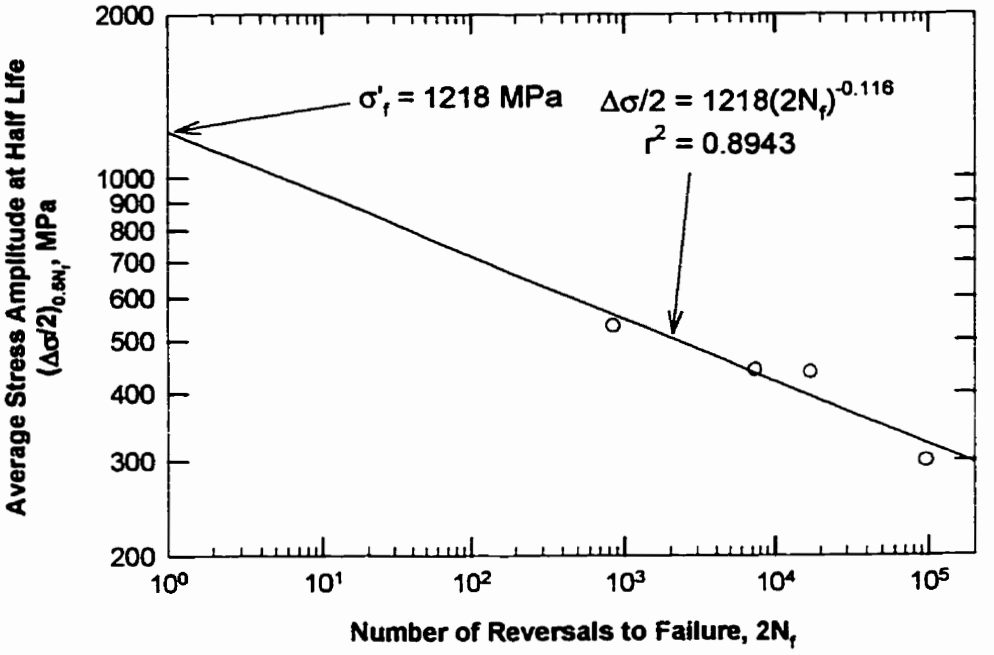

Figure 3.16: Variation of low-cycle fatigue with $\Delta\sigma/2$ shown on log-log basis for austenitic CuZnAl

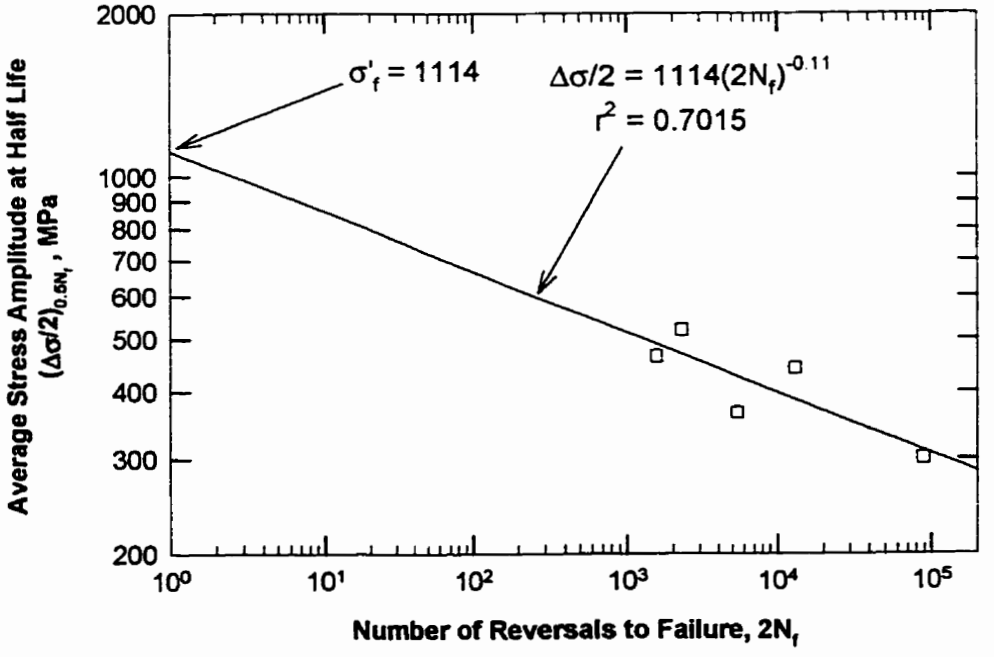

Figure 3.17: Variation of low-cycle fatigue with $\Delta\sigma/2$ shown on a log-log basis for martensitic CuZnAl

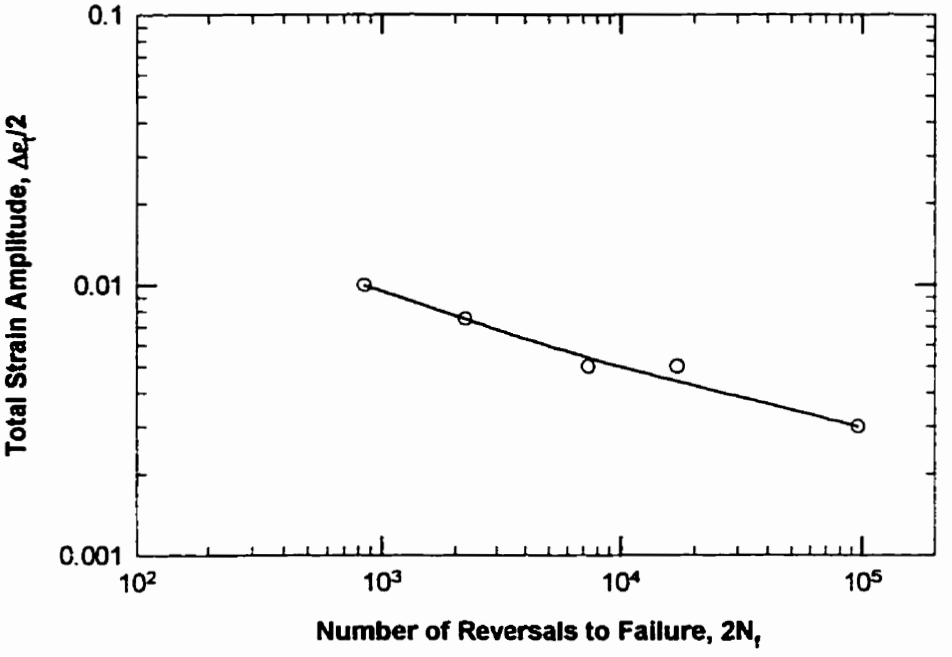

Figure 3.18: Total strain amplitude versus reversals to failure plot for austenitic CuZnAl

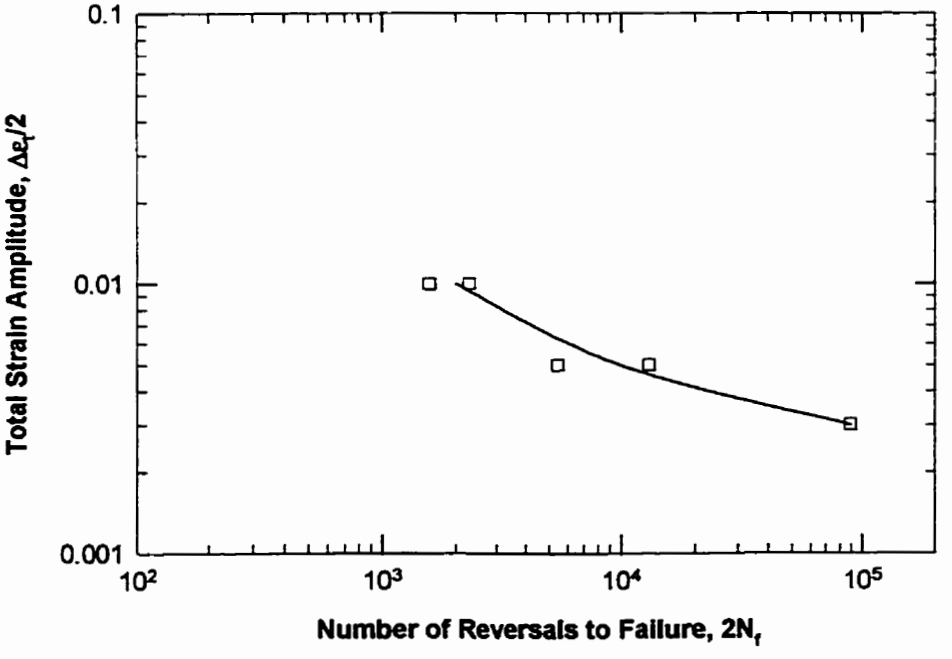

Figure 3.19: Total strain amplitude versus reversals to failure plot for martensitic CuZnAl

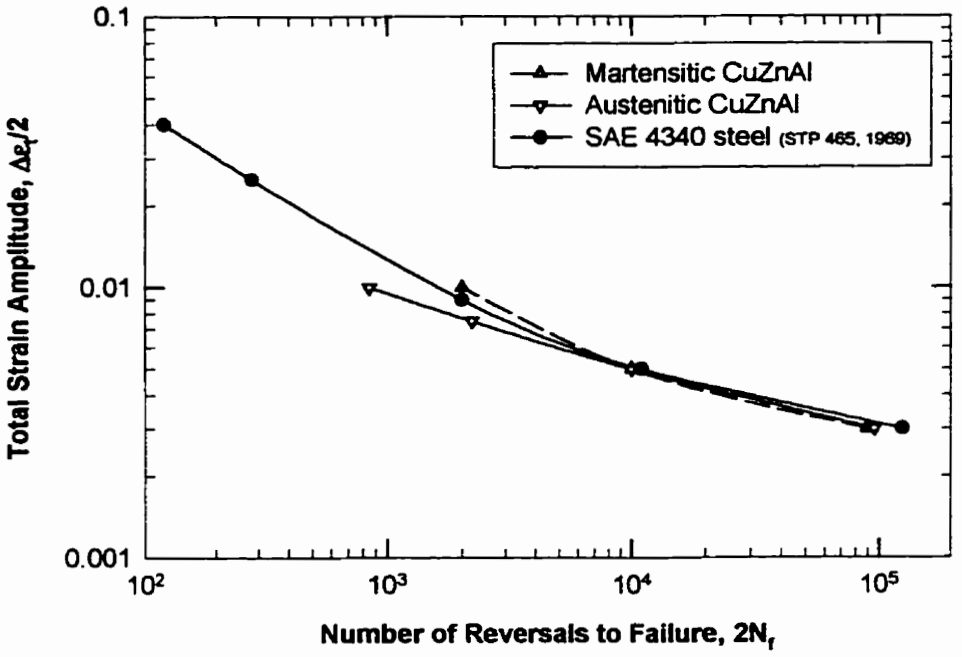

Figure 3.20: Comapring the behavior of CuZnAl to SAE 4340 steel in low-cycle fatigue

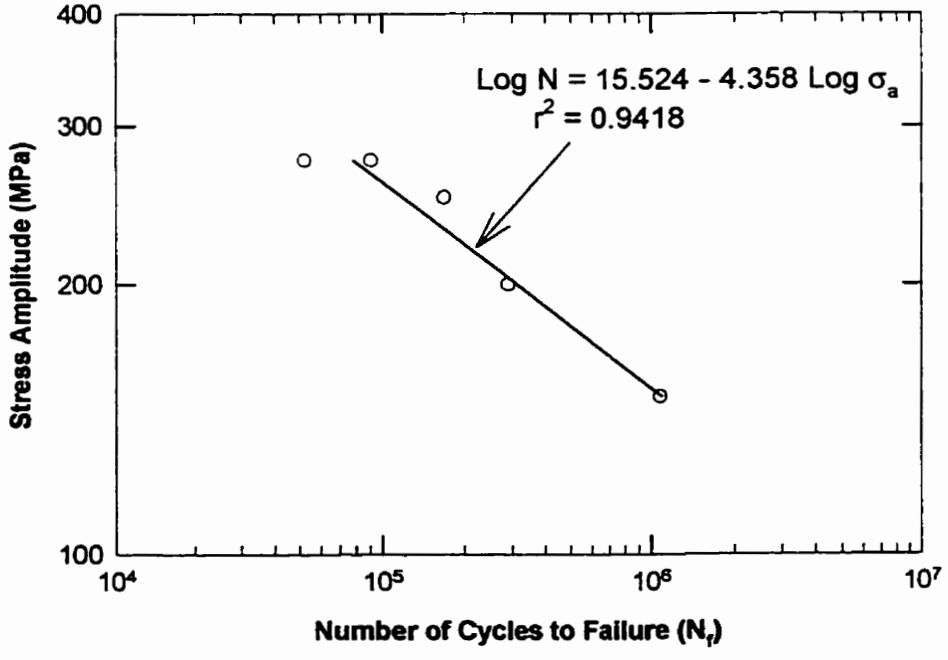

Figure 3.21: S-N curve of austenitic CuZnAl

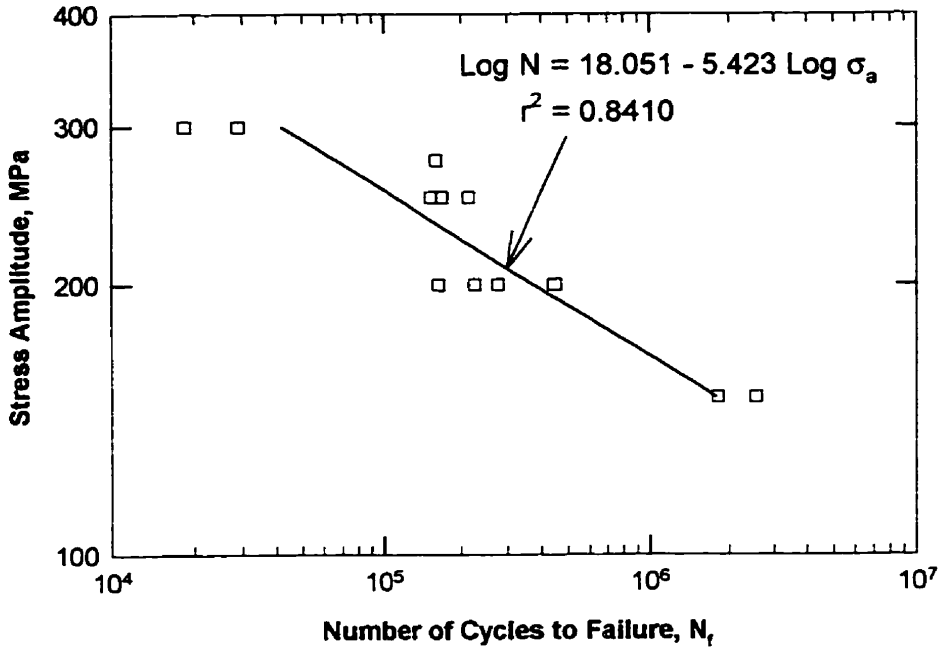

Figure 3.22: S-N curve of martensitic CuZnAl

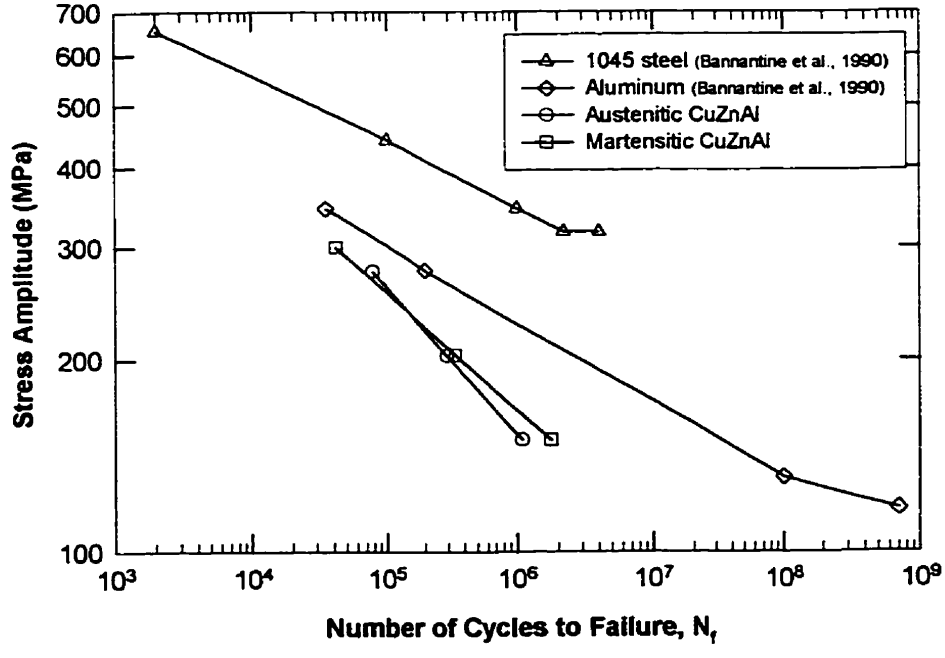

Figure 3.23: Comparison of S-N curves of CuZnAl, 1045 steel and 2024-T4 aluminum

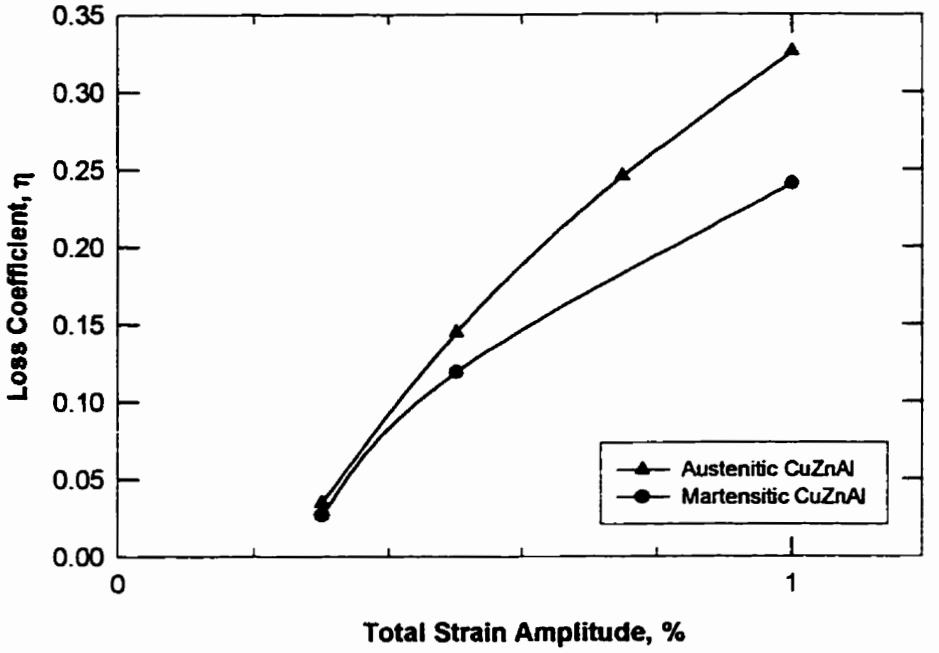

Figure 3.24: Loss coefficient as a function of strain amplitude as measured from LCF tests

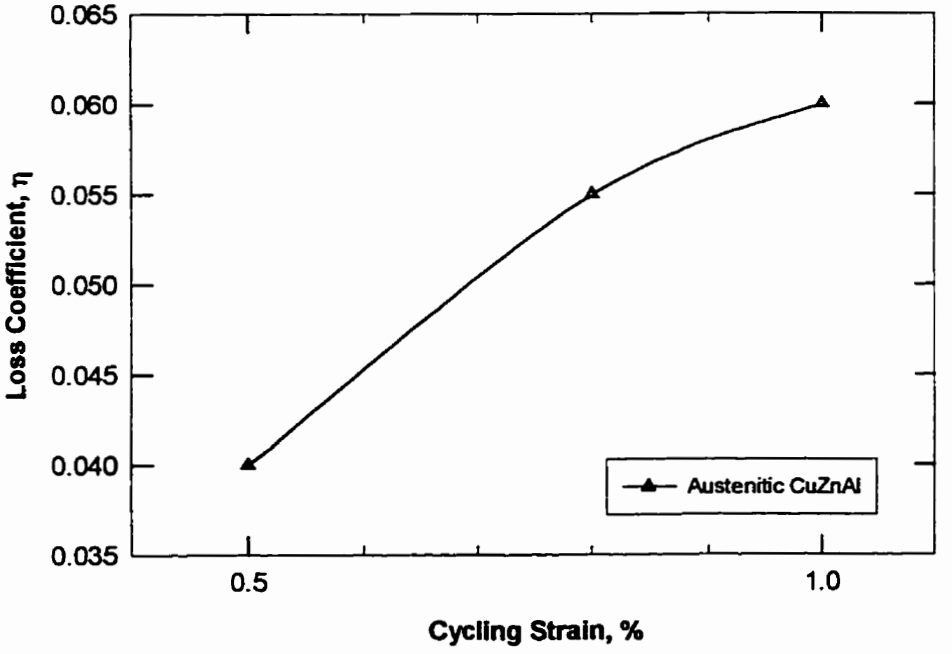

Figure 3.25: Loss coefficient as a function of cyclic strain for austenitc CuZnAl as measured from strain cycling

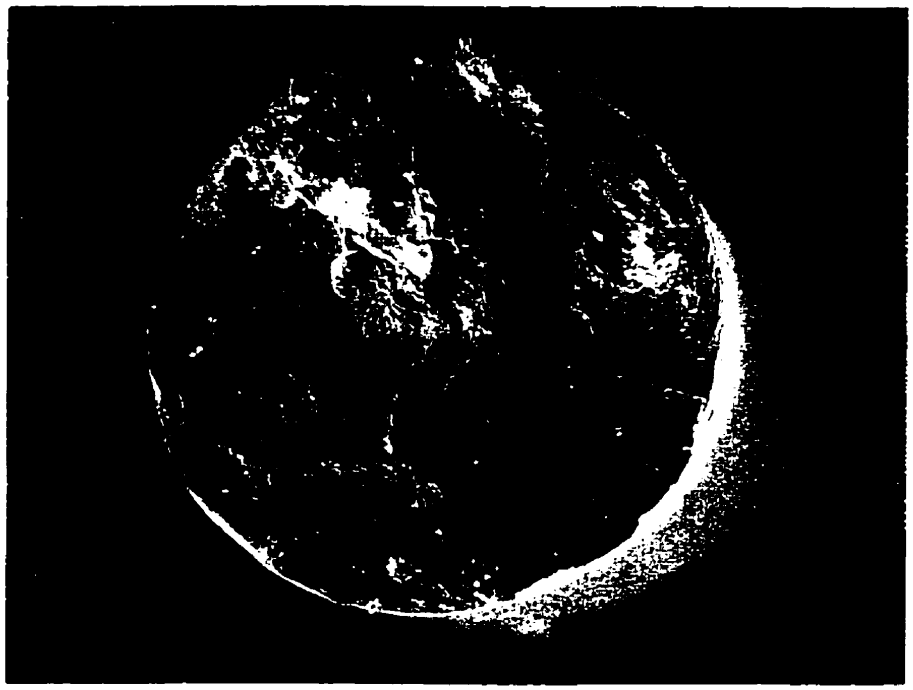

Figure 3.27: Fracture surface of sample AT4 (x20)

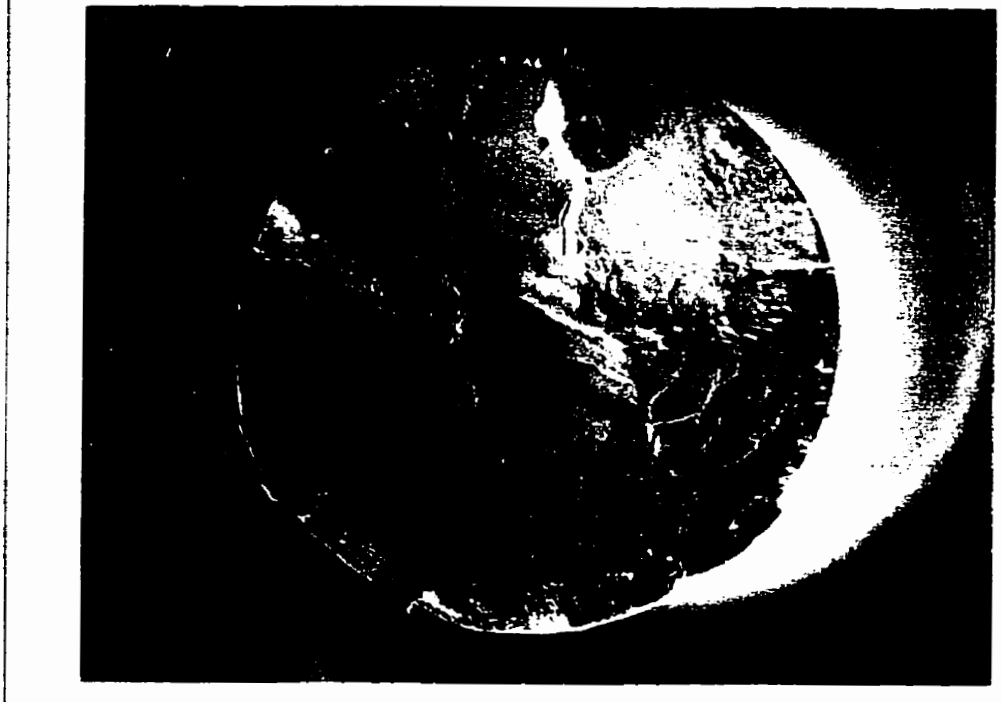

Figure 3.28: Fracture surface of sample MT1 (x20)

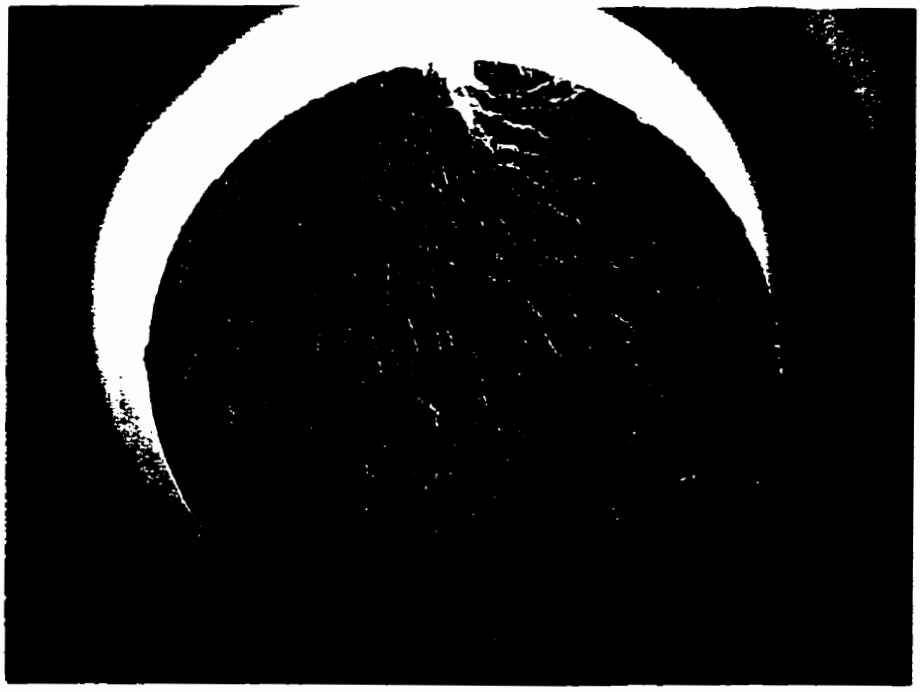

Figure 3.29: Fracture surface of sample AHCF1 (x20)

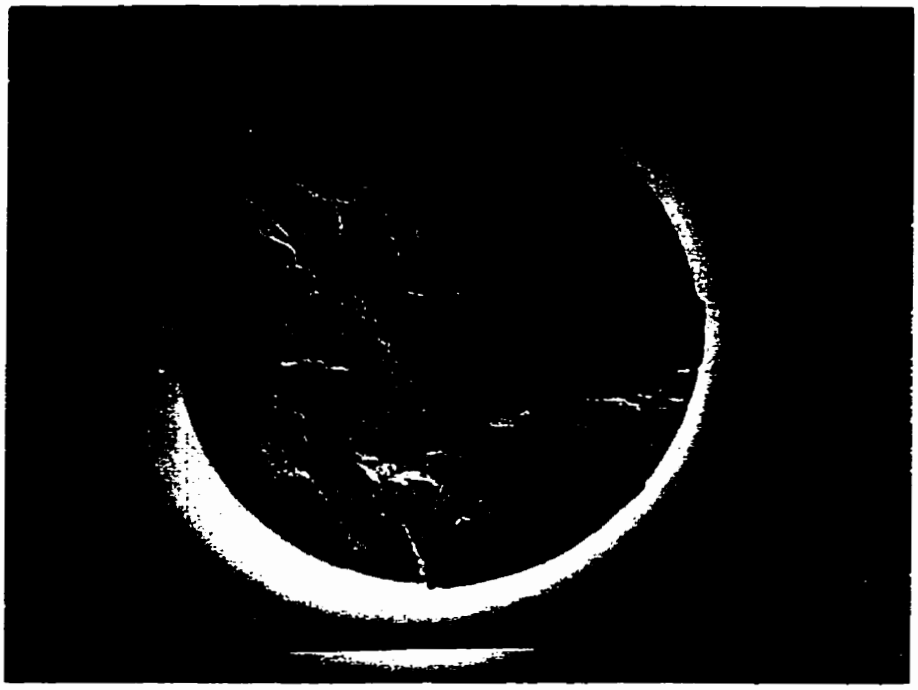

Figure 3.30: Fracture surface of sample MHCF4 (x20)

4 Conclusions

The mechanical and fatigue properties of austenitic and martensitic CuZnAl have been investigated through tensile, strain cycling, stress cycling, low- and high-cycle fatigue tests and damping energy measurements.

The tensile tests revealed that CuZnAl in the austenitic phase has a modulus of elasticity of 120000 MPa. This is 30% higher than the value measured for the martensitic alloy, 90000 MPa. The austenitic alloy also showed higher ultimate strains at failure. However, the martensitic alloy showed greater ultimate tensile strengths.

The superelastic behavior of austenitic CuZnAl was shown through strain cycling to strain levels of 0.5, 0.8, and 1.0%. In each case, after the first strain cycle, a small residual strain remains. However, with each subsequent cycle the strain recovery due to superelasticity was complete. Total strain recovery up to a strain level of 1% was achieved. It was also observed that the area within the hysteresis loops decreased with increasing number of strain cycles. This was due to the fact that the transformation stress levels, σ^{P-M} and σ^{M-P}, decreased with increasing strain cycles. This indicates a degradation of the superelastic effect with increasing numbers of strain cycles.

The cyclic stress response of the austenitic CuZnAl was characterized by cyclic hardening within the first 10 cycles followed by cyclic stability up to the point of fracture. For the martensitic CuZnAl, cyclic hardening occurred from the first cycle with the process accelerating towards the point of failure. The cyclic strength coefficient, K', and the cyclic work hardening exponent, n', calculated for austenitic CuZnAl alloy was almost double the values calculated for the martensitic CuZnAl. Both alloys exhibited linear Coffin-Manson plots. However, e'_f is not equal to e_f for either alloy. The constants of the stress amplitude-fatigue life power law relationship, namely σ'_f and b, are similar for both alloys. A total strain amplitude - reversals to failure plot shows a similarity in the

behavior of austenitic and martensitic CuZnAl compared to that of steel.

The high-cycle fatigue behavior of martensitic CuZnAl is better than that of austenitic CuZnAl despite experiencing premature failure in some martensitic HCF test samples. The fatigue strength at $N = 10^6$ of martensitic and austenitic CuZnAl are, respectively, 167 MPa and 153 MPa. However, the fatigue lives of both CuZnAl alloys tested compares poorly with the high-cycle fatigue behavior of steel and aluminum.

The loss coefficient versus total strain amplitude plot shows the non-linear damping behavior of CuZnAl due to plastic deformation. Loss coefficient due to superelasticity is also shown to be non-linear with increasing cycling strain. The damping due to plastic deformation of austenitic CuZnAl is greater than that of martensitic CuZnAl. Although the loss coefficient due to plastic deformation of austenitic CuZnAl is five times greater than that due to superelasticity, its application is limited by the reduced fatigue lives resulting from plastic deformation. As a result the damping associated with superelasticity shows promise in damping applications.

Recommendations for future studies:

1. A test program be conducted in which CuZnAl and commonly used materials, steel and aluminum, are subjected to similar test programs to obtain a clearer picture of their comparative behavior.

2. If CuZnAl is to be used for its high damping capacity in a structure, employing CuZnAl as a high stress bearing member is not recommended as it has been shown experimentally that CuZnAl has a lower modulus of elasticity and high-cycle fatigue properties compared to steel. It is however recommended that a composite be made with CuZnAl being embedded in the matrix, to take advantage of the damping capacity due to superelasticity of austenitic CuZnAl. Further studies should be carried out in the area of fatigue and damping of CuZnAl embedded composites to quantify the behavior of such systems.

3. Only large diameter ASTM standard test specimens should be used in testing programs. The use of relatively small diameter samples in this study was due to the

fact that the material was supplied only in this size. Small diameter specimens are difficult to machine. Problems arising from machining cause specimen misalignment during testing. Small diameter specimens also buckle when tested at high stress or strain amplitudes.

4. It is recommended that the superelastic behavior of austenitic CuZnAl be observed under compressive loading conditions. Also, the strain cycling experiments of superelastic CuZnAl should be carried out till specimen failure occurs to get an estimate of the fatigue life due to strain cycling.

References

American Society for Testing and Materials. 1990. "ASTM E 8M Methods for Tension Testing of Metallic Materials," Philadelphia.

American Society for Testing and Materials. 1990. "ASTM E 466 Conducting Constant Amplitude Axial Fatigue Tests of Metallic Materials," Philadelphia.

American Society for Testing and Materials. 1990. "ASTM E 606 Standard Recommended Practice for Constant Amplitude Low Cycle Fatigue Testing" Philadelphia.

AMT. 1995. Sales Pamphlet of the Advanced Materials and Technologies Company.

ASM Handbook, Vol. 8 - Mechanical Testing, 1992.

Bannantine, J. A., Comer, J. J., and Handrock, J. L. 1990. "Fundamentals of Metal Fatigue Analysis," Prentice Hall, Englewood Cliffs, New Jersey.

Barrett, D.J. 1995. "A One-Dimensional Constitutive Model for Shape Memory Alloys." Journal of Intelligent Material Systems and Structures, Vol 6, May 1995.

Delaey, L., Jansesn, J., Van de Mosselaer, D., Dullenkopf, G., and Deruyttere A. 1978. "Fatigue Properties of Pseudoelastic Cu-Zn-Al Alloys." Scripta Mettalurgica, Vol. 12, pp. 373-376.

Dye, T.E. 1990. "An Experimental Investigation of the Behavior of Nitinol," MS thesis, Virginia Tech.

Ford D.S., and White, S.R. 1996. "Thermomechanical Behavior of 55Ni45Ti Nitinol." Acta Mater. Vol 44, No. 6, pp. 2295-2307.

Funakubo, H. (translated by J.B. Kennedy, Shape Memory Alloys, 1987, Gordon and Breach Science Publishers, New York.

Gandhi, M. V., and Thompson, B. S. 1992. "Smart Materials and Structures." Chapman and Hall.

Goel, A. P., "Fatigue Problems in Power Transmission Lines, Canadian Civil Engineer, February 1994.

Graesser, E. J., and Cozzarelli, F. A. 1991. "Shape Memory Alloys as New Materials for Aseismic Isolation." Journal of Engineering Mechanics, Vol. 117, No. 11, November.

Jalihal, P., Utku, S., and Wada, B. K. 1994. "Active Base Isolation in Buildings Subjected to Earthquake Excitation." Adaptive Structures and Composite Materials: Analysis and

Application. ASME. AD-Vol.45/MD Vol. 54. pp. 37 - 45.

Janssen, J., Follon, M., and Delaey, L. 1979. "The Fatigue Properties of Superelastic Cu-Zn-Al Alloys." Strength of Metals and Alloys, Proceedings of the International Conference, 5th, Aachen, Germany, Aug. 27 - 31, 1979. Published by Pergamon Press (Int Ser on the Strength and Fracture of Mater. and Sturct.), pp. 1125 - 1130.

Krishnan, R. V., Delaey, L., Tas, H., and Warlimont, H. 1974. "Thermoplasticity, Pseudoelasticity and the Memory Effects Associated with Martensitic Transformations." Part 2. Journal of Materials Science, Vol. 9, pp. 1536 - 1544.

Lazan, B. J. 1968. Damping of Materials and Members in Structural Mechanics. Pergamon Press.

Melton, K. N., and Mercier, O. 1979a. "Fatigue Life of CuZnAl Alloys", Scripta Metallurgica, Vol. 13, pp. 73-75.

Melton, K. N., and Mercier, O. 1979b. "Fatigue of NiTi Thermoelastic Martensites", Acta Metallurgica, Vol. 27, pp. 137-144.

Paine, J. S. N., and Rogers, C. A. 1994a. "Review of Multi-functional SMA Hybrid Composite Materials and their Applications." Adaptive Structures and Composite Materials: Analysis and Application. ASME. AD-Vol.45/MD Vol. 54. pp. 37 - 45.

Paine, J. S. N., and Rogers, C. A. 1994b. "Improved Impact Damage Resistance in Hybrid SMA Composite Materials", Proceedings, Smart Structures and Materials 1994 SPIE Conference, Feb. 14-18, 1994, Orlando, FL.

Pops, H., "Stress-Induced Pseudoelasticity in Ternary Cu-Zn Based Beta Prime Phase Alloys," Metallurgical Transactions, 1970, vol. 1, pp. 251-258.

Pops, H., and Ridley, N. 1970. "Influence of Aluminum on the Martensitic Transformation of Beta Phase CuZn Alloys." Metallurgical Transactions, Vol. 1, pp. 2653-2655.

Prasad, N.E., Malakondaiah, G., Kutumbarao, V.V., and Rama Rao, P. 1996. "In-plane Anisotropy in Low-Cycle Fatigue Properties of and Bilinearity in Coffin-Manson Plots for Quaternary Al-Li-Cu-Mg 8090 Alloy Plate." Material Science and Technology, July 1996, Vol. 12. pp. 563 - 577

Rodriguez, C., and Brown, L.C. 1975. "The Mechanical Properties of SME Alloys", Shape Memory Effects in Alloys, pp. 29 - 57. Plenum Press, N.Y., Ed. J Perkins.

Sakamoto, H., Kijima, Y., and Shimizu, K. 1982. "Fatigue and Fracture Characteristic of Polycrystalline Cu-Al-Ni Shape Memory Alloys," Transactions of the Japan Institute of Metals, Vol. 23, No. 10 (1982), pp. 585-594.

Schetky, L. McD., "Shape-Memory Alloys," Sci. American, Nov. 1979, vol. 241, pp. 74-82.

Schetky, L. M. 1990. "Shape Memory Alloy Applications in Space Systems." In Engineering Aspects of Shape Memory Alloys. Duerig et al. editors. Butterworth-Heinemann, England. pp 170 -177.

Shahin, A. R., Meckl, P. H., and Jones, J. D. 1994. "Vibration Control Using Shape Memory Alloy Wires". Adaptive Structures and Composite Materials: Analysis and Application. ASME. AD-Vol.45/MD Vol. 54. pp. 37 - 45.

STP 465, 1969. "Manual on Low Cycle Fatigue Testing," American Society for Testing and Materials, Philadelphia.

Wu, M.H., and Biermann, R.J. 1991. "Shape Memory Alloys." Metals Handbook, Volume 2, 10th Edition. ASM.

APPENDIX A

MECHANICAL PROPERTIES OF CuZnAl ALLOYS

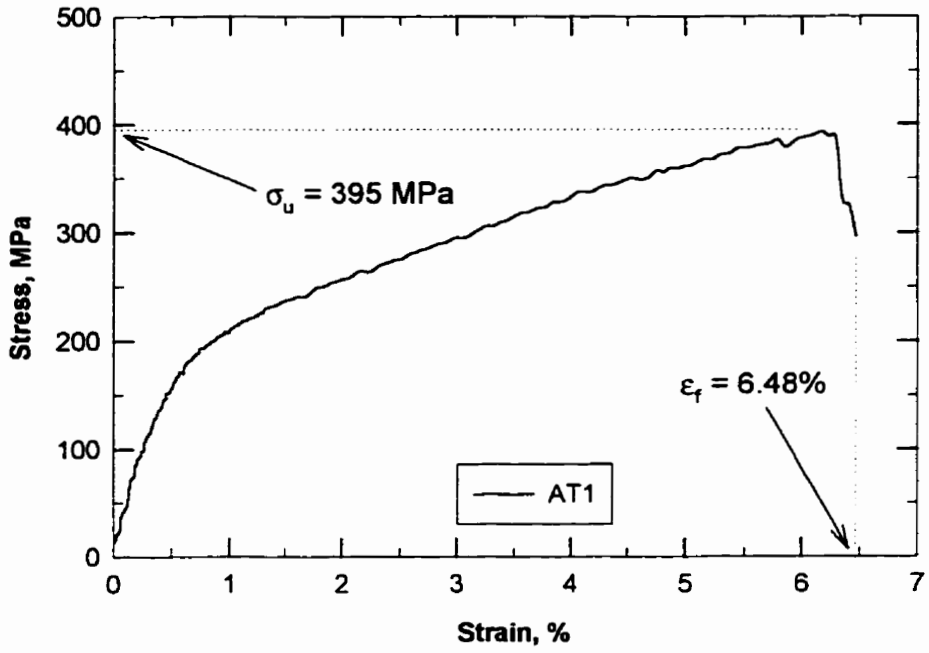

Figure A.1: Stress-strain curve of sample AT1

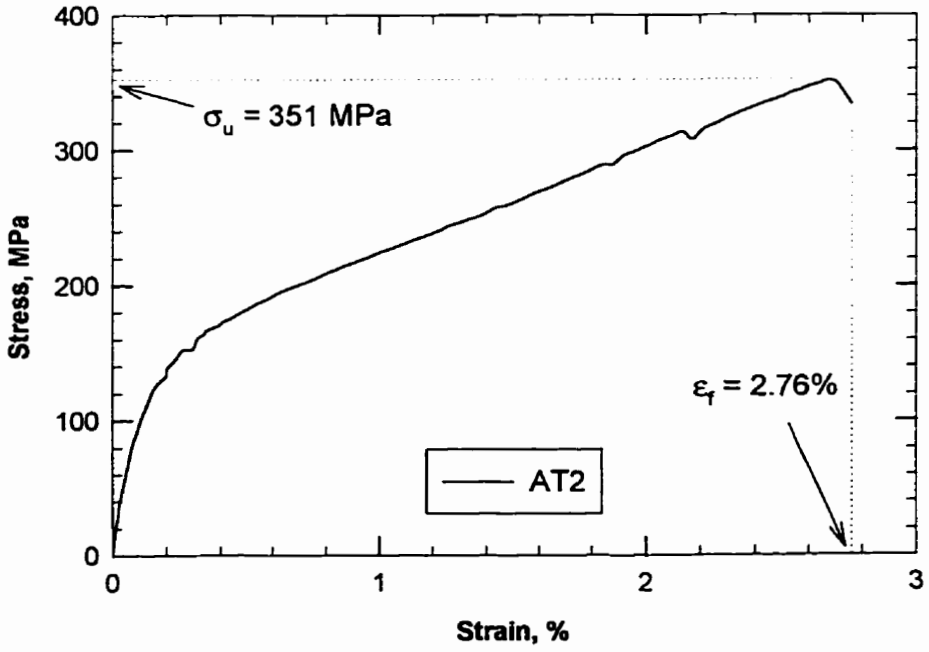

Figure A.2: Stress-strain curve of sample AT2

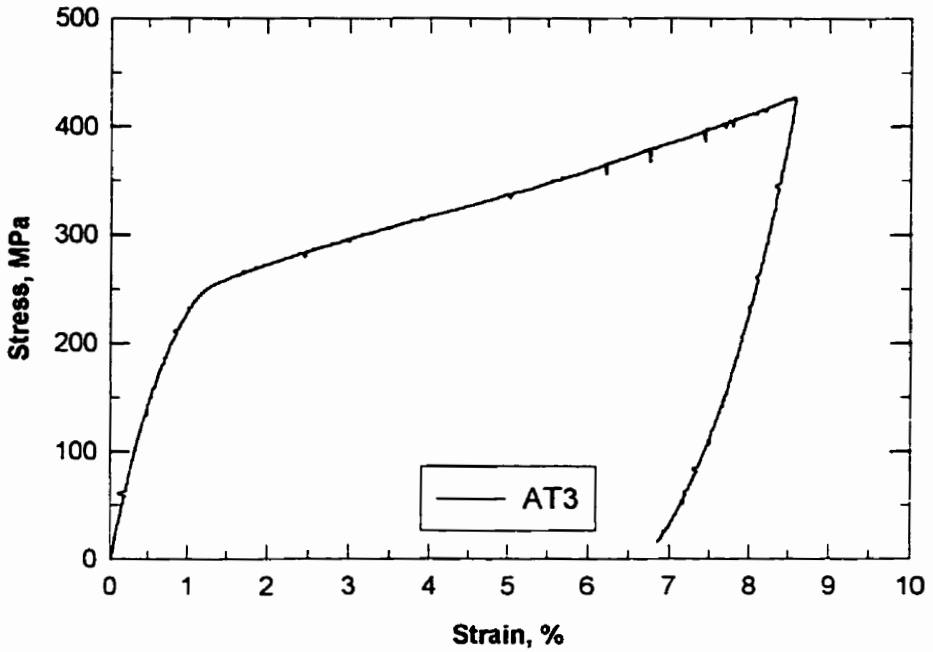

Figure A.3: Stress-strain curve of sample AT3

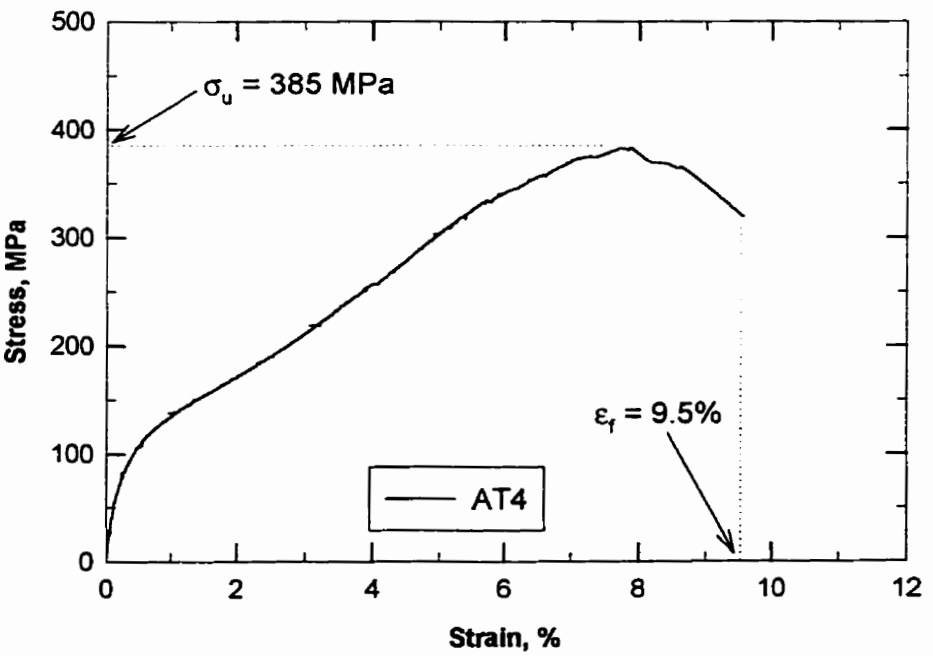

Figure A.4: Stress-strain curve of sample AT4

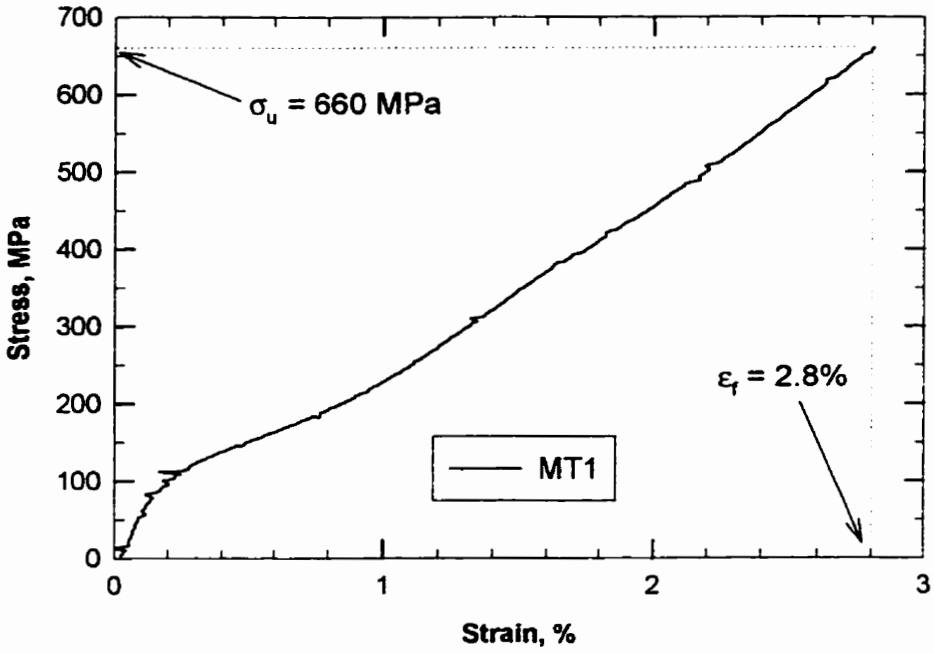

Figure A.5: Stress-strain curve of sample MT1

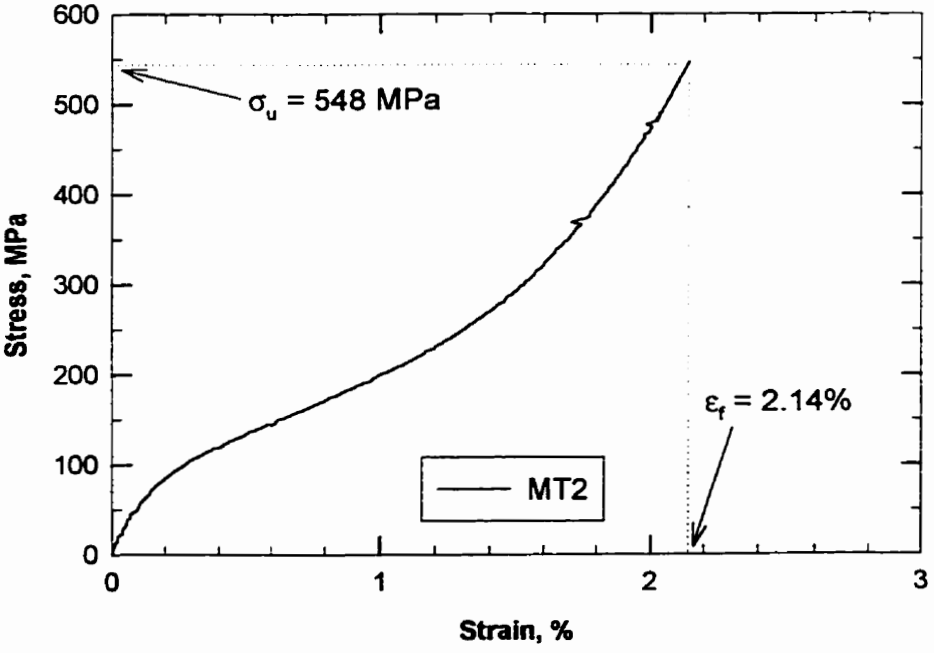

Figure A.6: Stress-strain curve of sample MT2

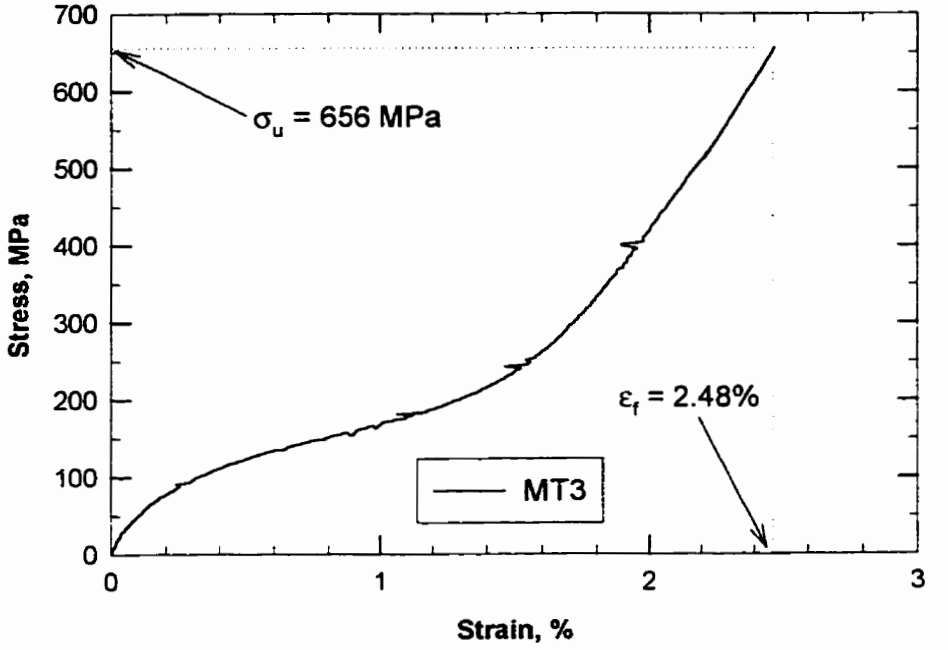

Figure A.7: Stress-strain curve of sample MT3

APPENDIX B

STRESS-STRAIN CURVES FROM THE LOW CYCLE FATIGUE TESTS

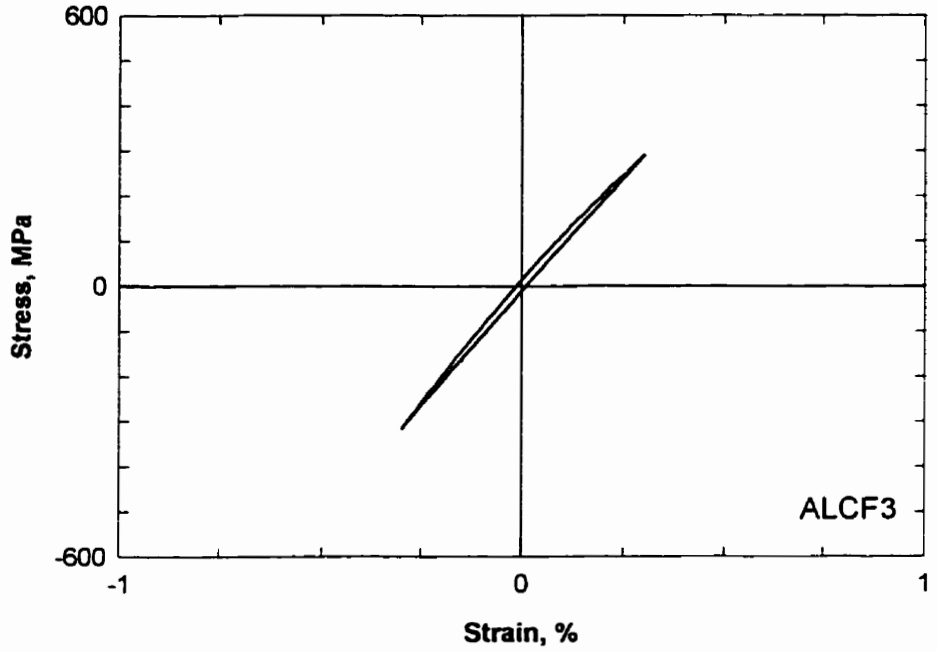

Figure B.1: Hysteresis loop of sample ALCF3 at N = 20000 cycles

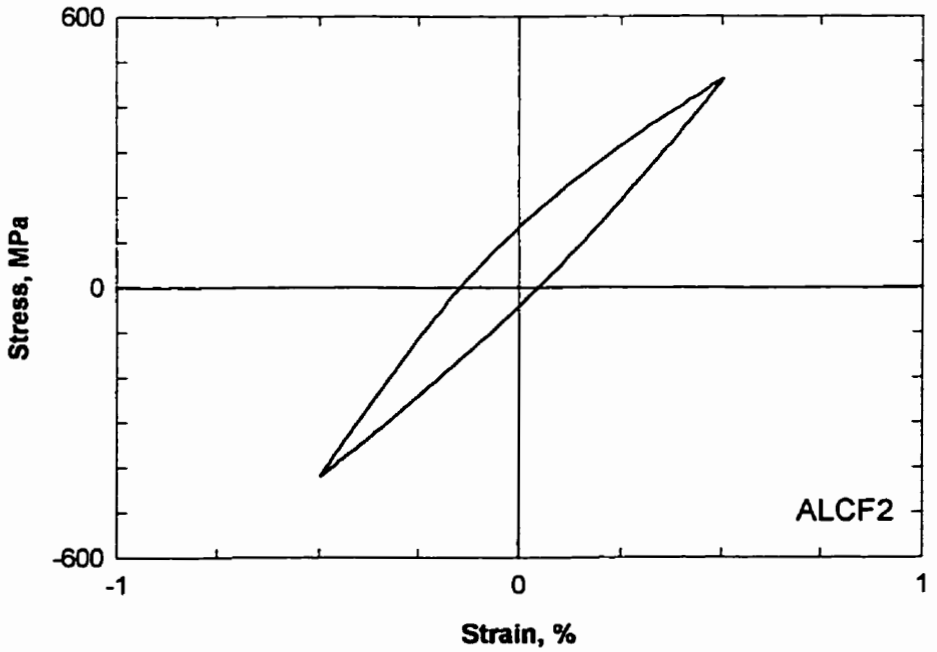

Figure B.2: Hysteresis loop of sample ALCF2 at N = 2000 cycles

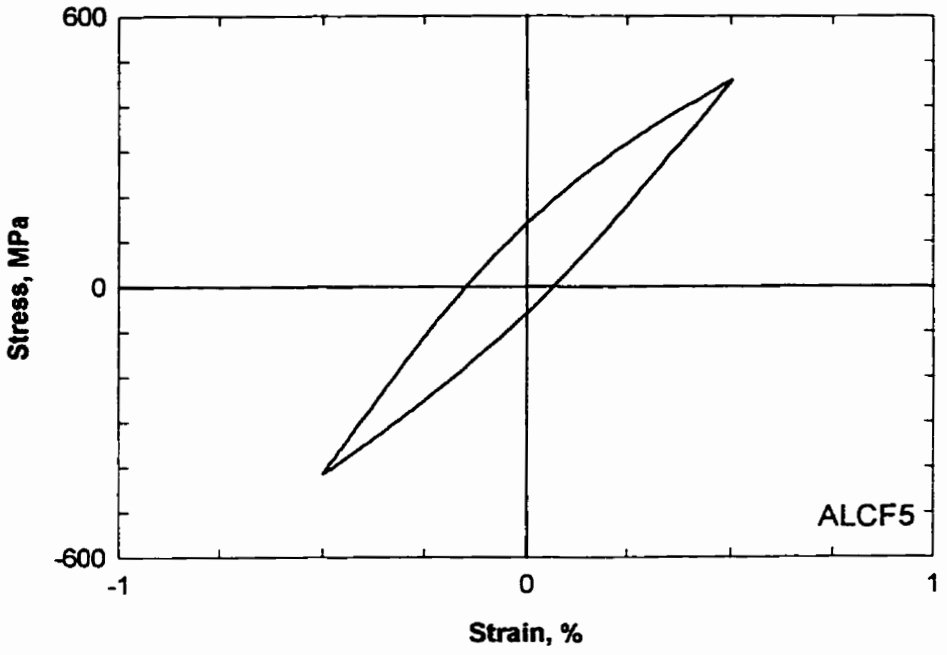

Figure B.3: Hysteresis curve of sample ALCF5 at N = 4000 cycles

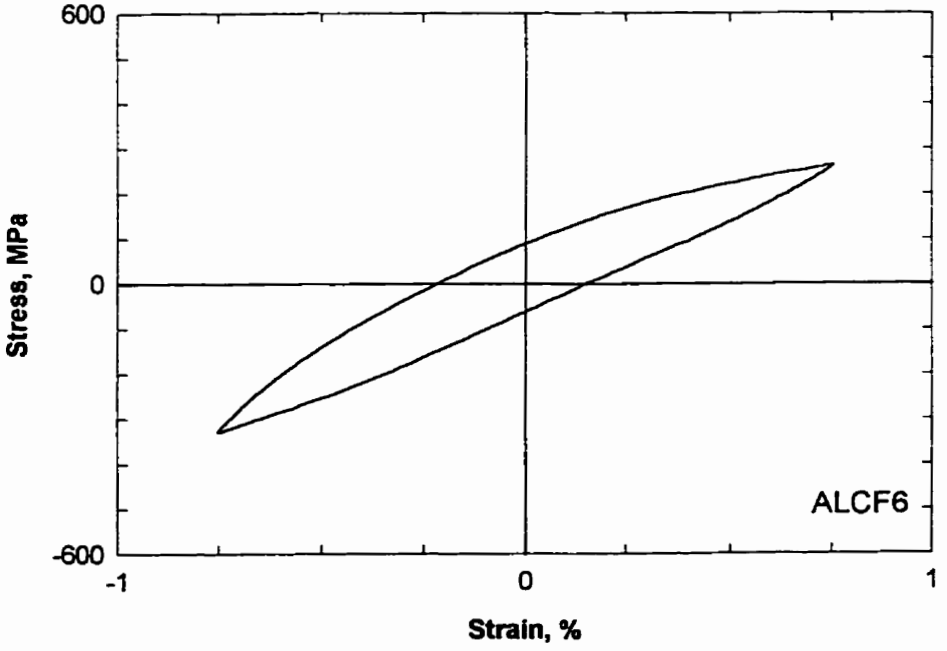

Figure B.4: Hysteresis curve of sample ALCF6 at N = 500 cycles

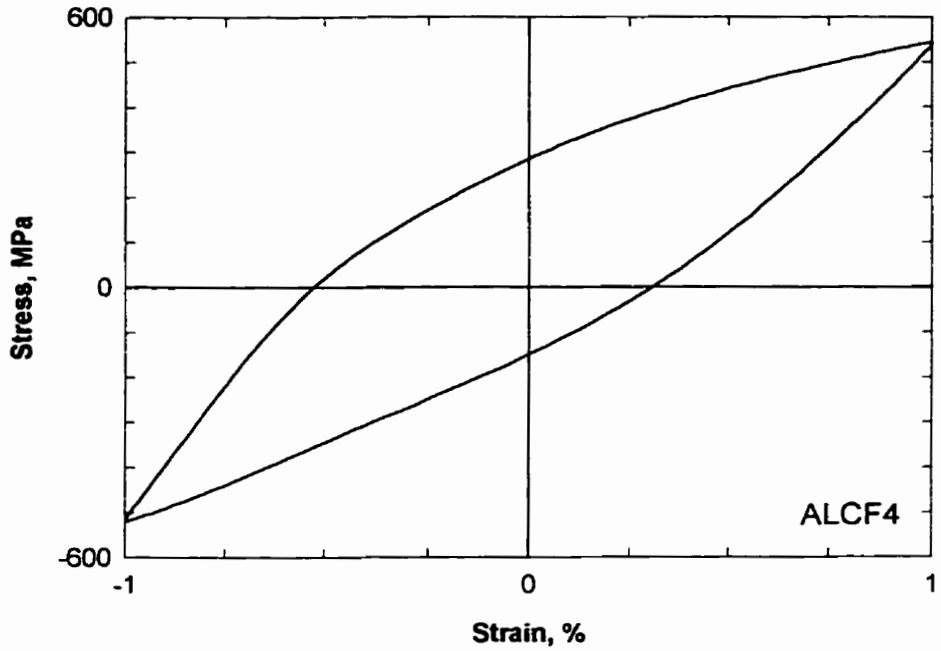

Figure B.5: Hysteresis curve of sample ALCF4 at N = 200 cycles

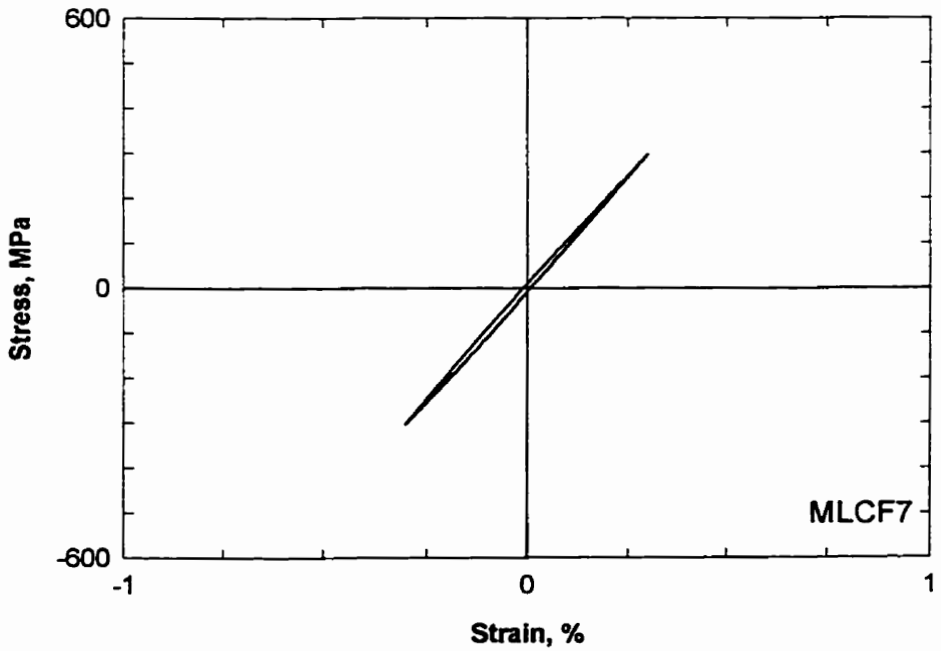

Figure B.6: Hysteresis curve of sample MLCF7 at N = 20000 cycles

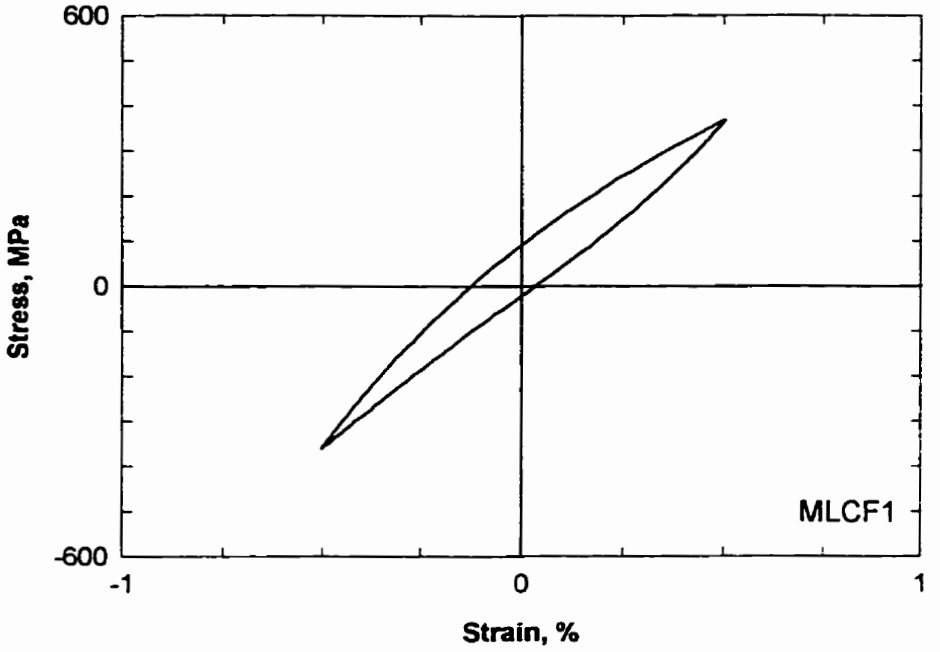

Figure B.7: Hysteresis curve of sample MLCF1 at N = 1000 cycles

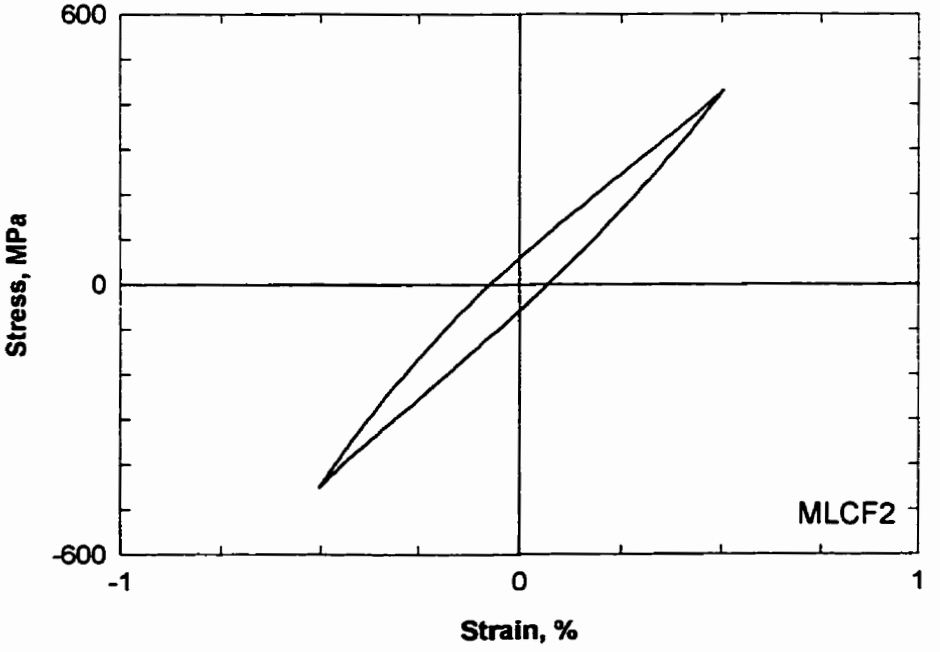

Figure B.8: Hysteresis curve of sample MLCF2 at N = 3000 cycles

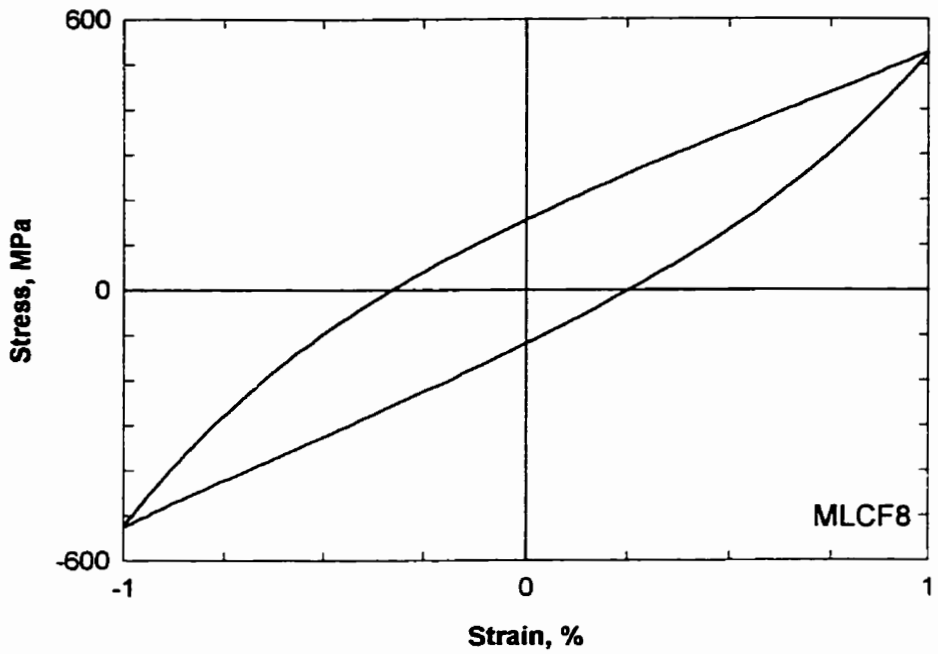

Figure B.9: Hysteresis curve of sample MLCF8 at N = 600 cycles

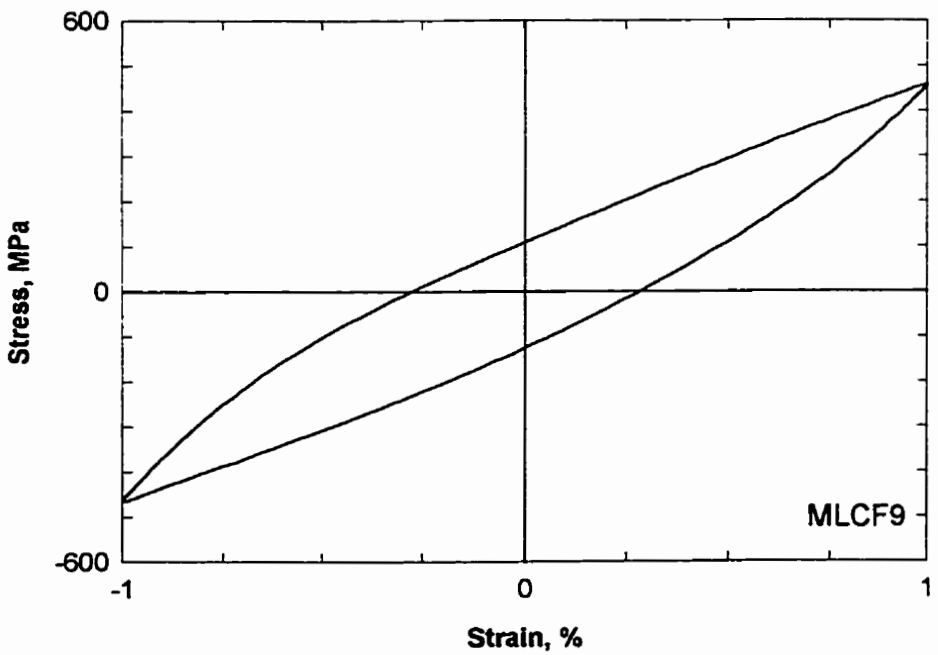

Figure B.10: Hysteresis curve of sample MLCF9 at N = 400 cycles

APPENDIX C

STRESS STRAIN CURVES FROM THE HIGH CYCLE FATIGUE TESTS

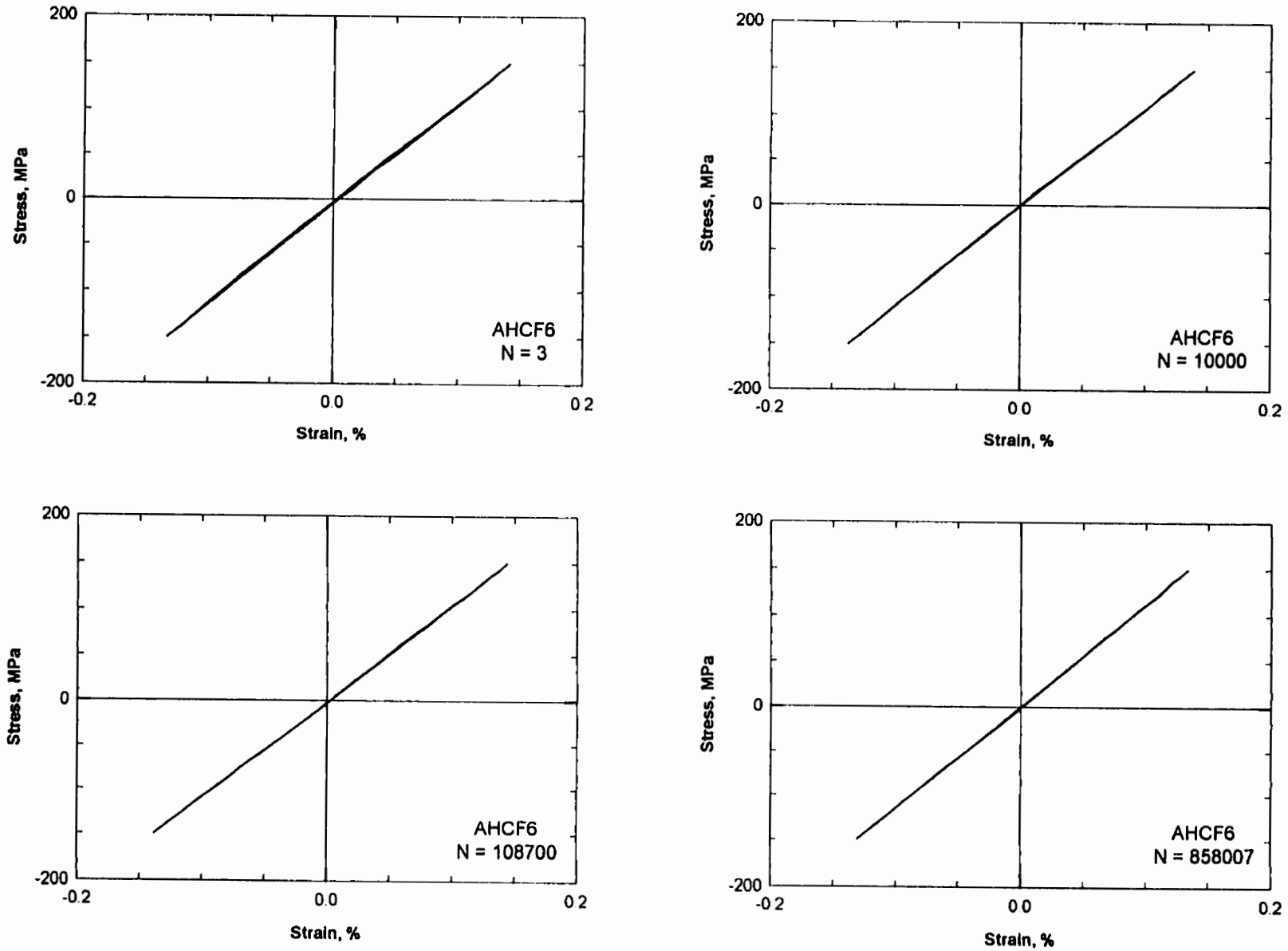

Figure C.1: Hysteresis curves for sample AHCF6 from the HCF experiments (Stress amplitude = 150 MPa)

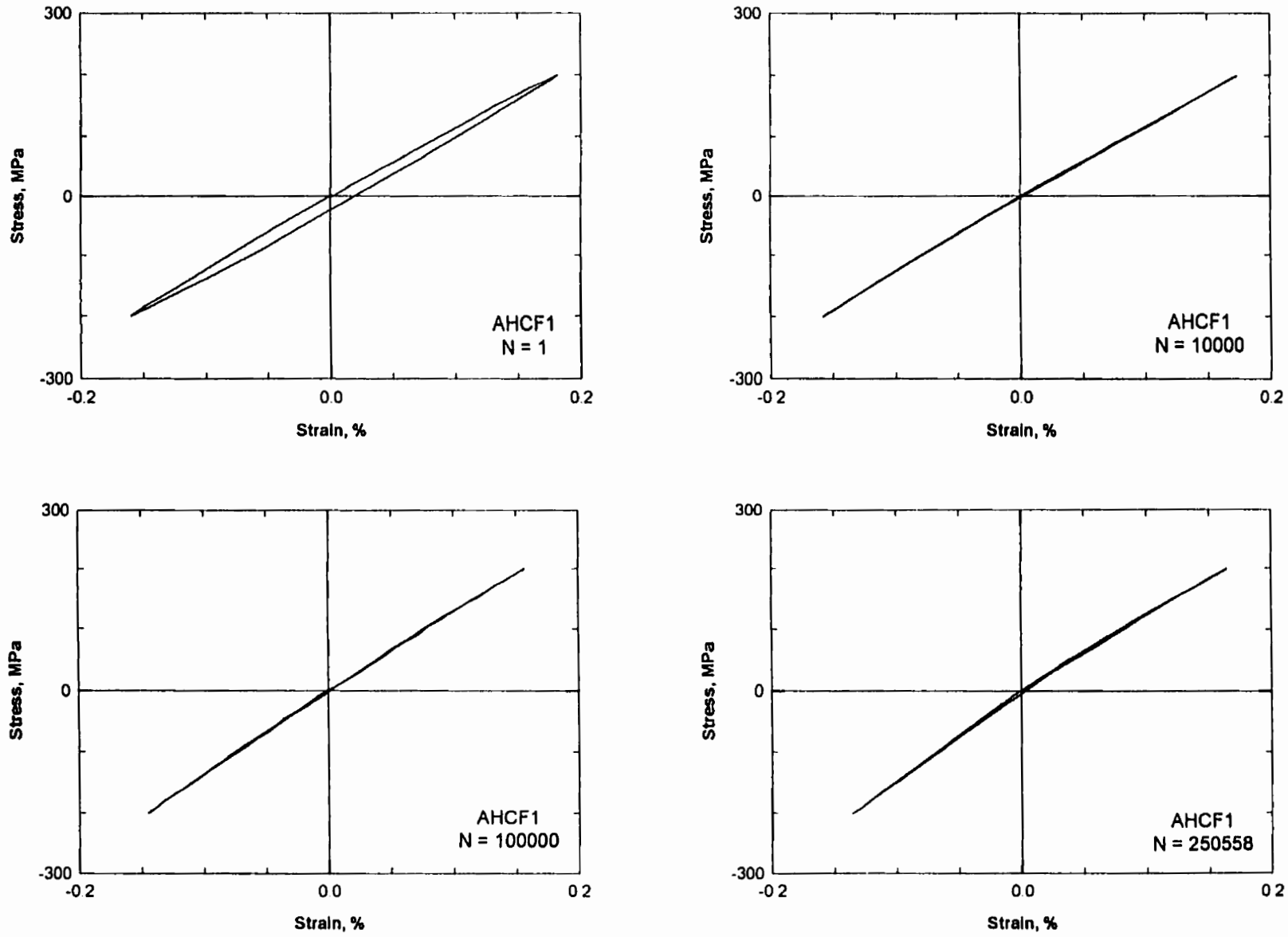

Figure C.2: Hysteresis curves for sample AHCF1 from the HCF experiments (Stress amplitude = 200 MPa)

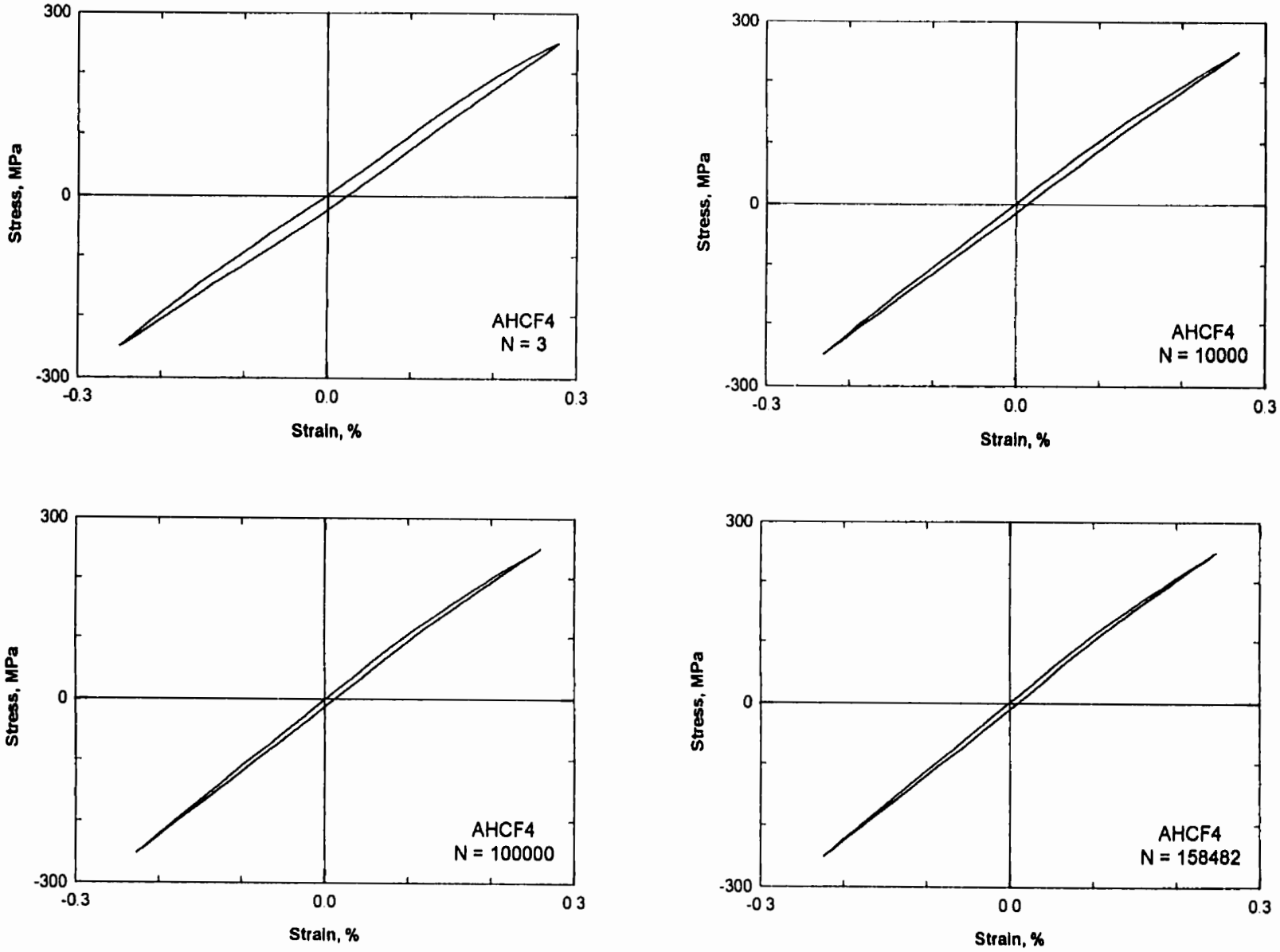

Figure C.3: Hysteresis curves for sample AHCF4 from the HCF experiments (Stress amplitude = 250 MPa)

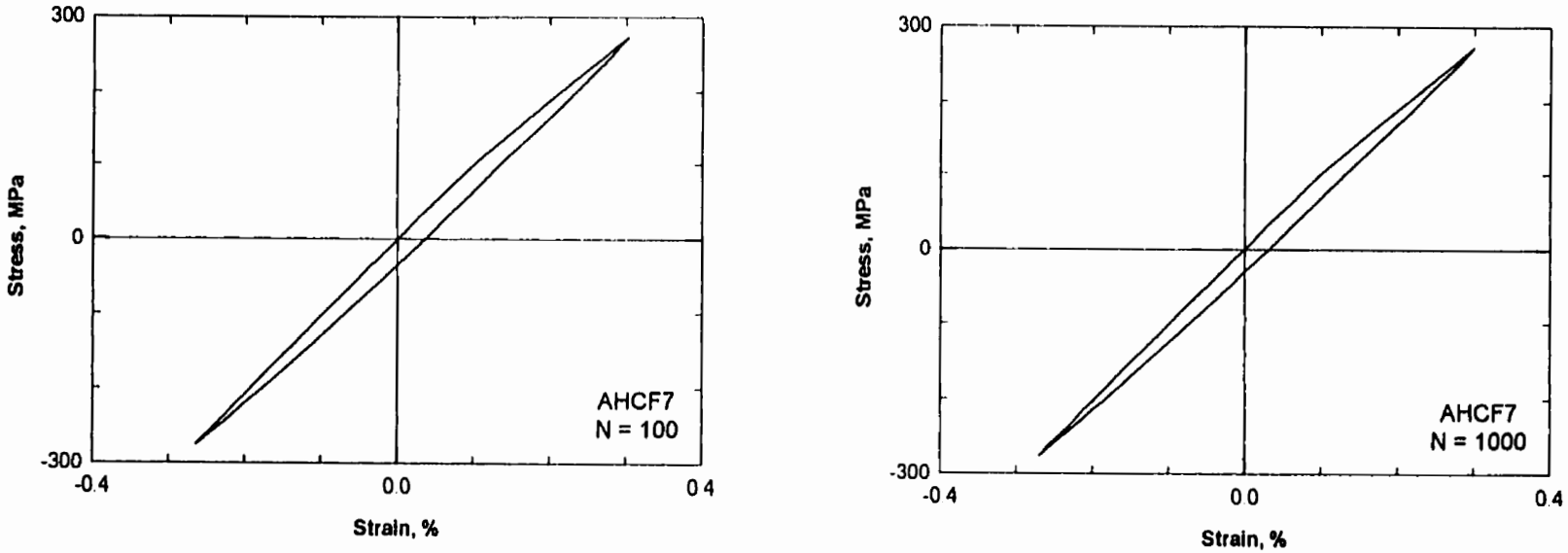

Figure C.4: Hysteresis curves for sample AHCF7 from the HCF experiments (Stress amplitude = 275 MPa)

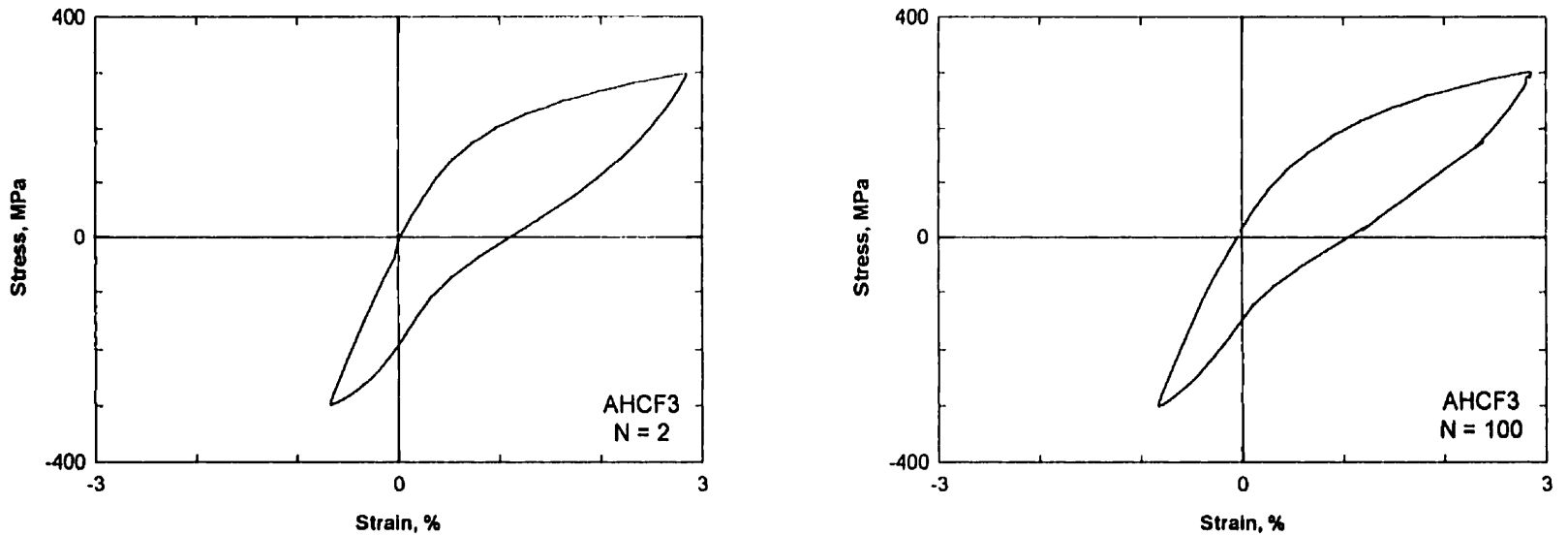

Figure C.5: Hysteresis curves for sample AHCF3 from the HCF experiments (Stress amplitude = 300 MPa)

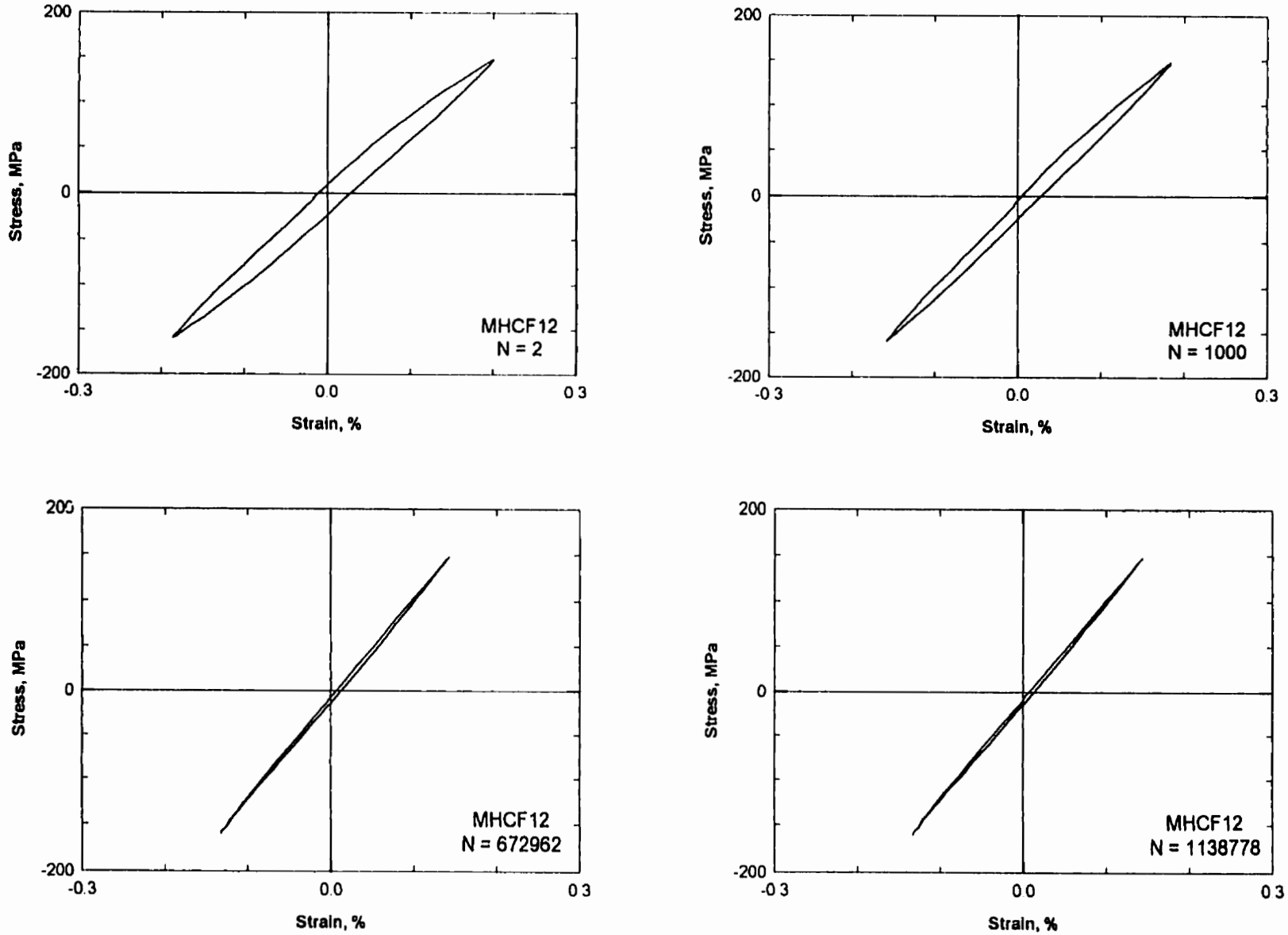

Figure C.6: Hysteresis curves for sample MHCF12 from the HCF experiments (Stress amplitude = 150 MPa)

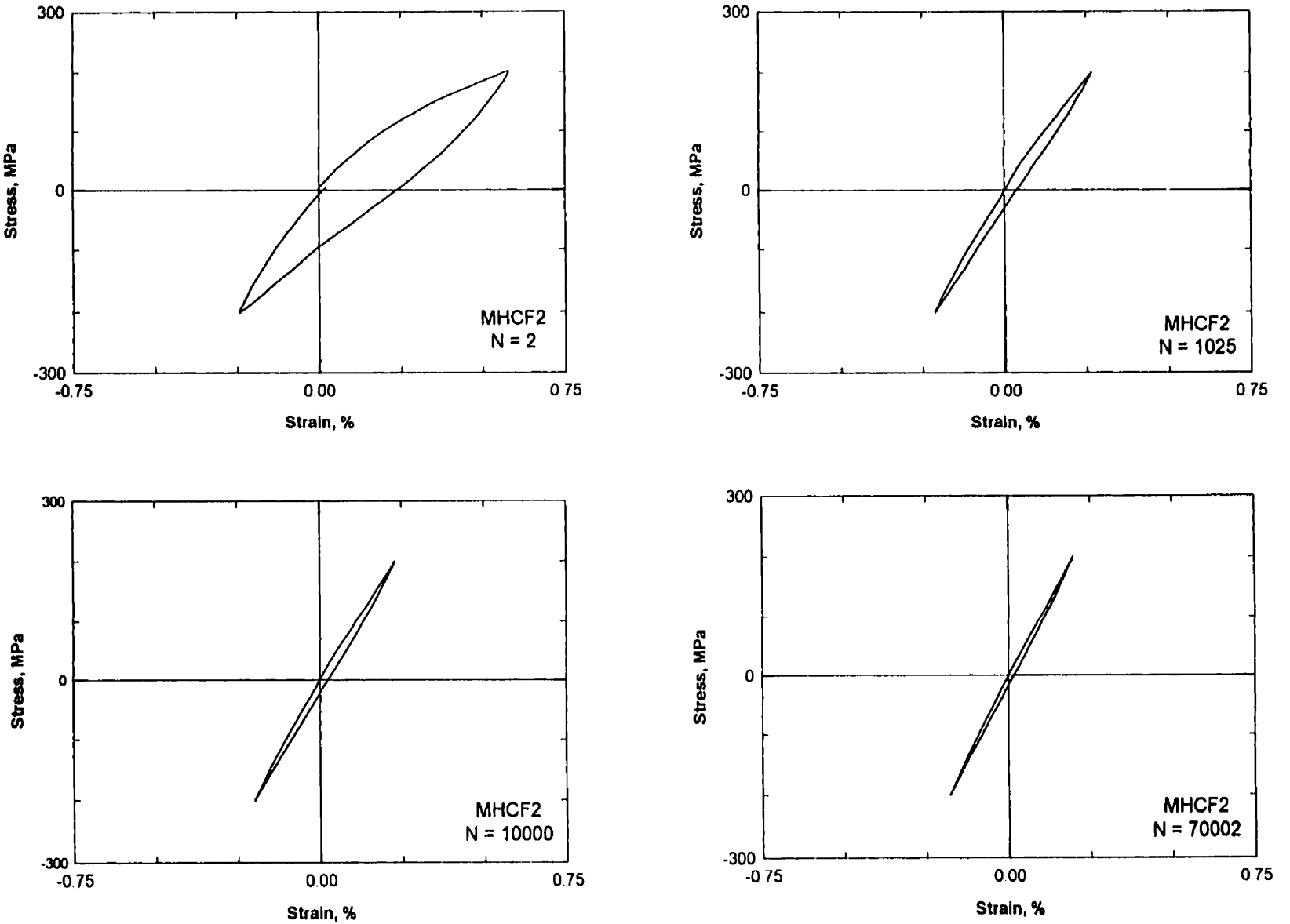

Figure C.7: Hysteresis curves for sample MHCF2 from the HCF experiments (Stress amplitude = 200 MPa)

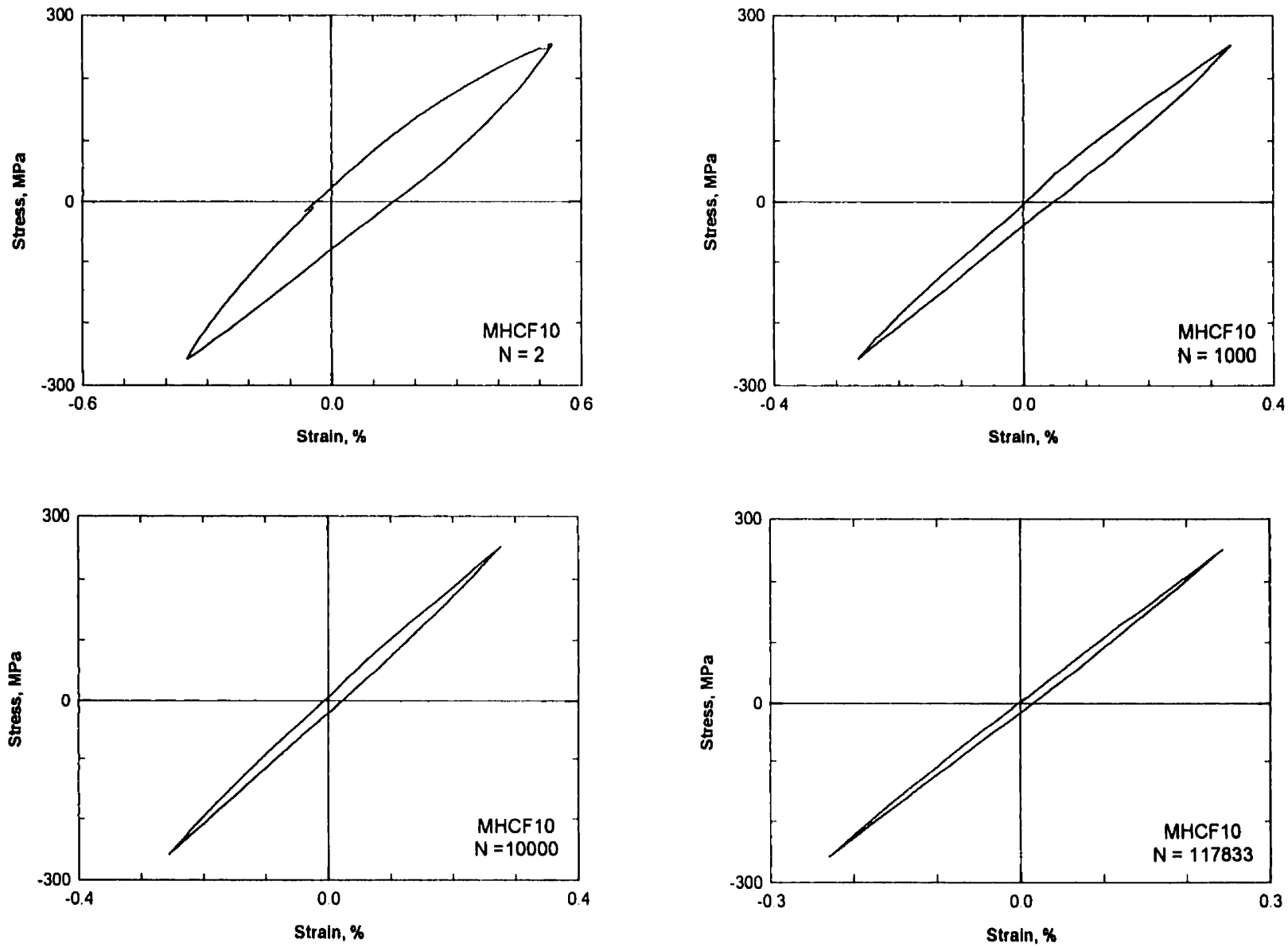

Figure C.8: Hysteresis curves for sample MHCF10 from the HCF experiments (Stress amplitude = 250 MPa)

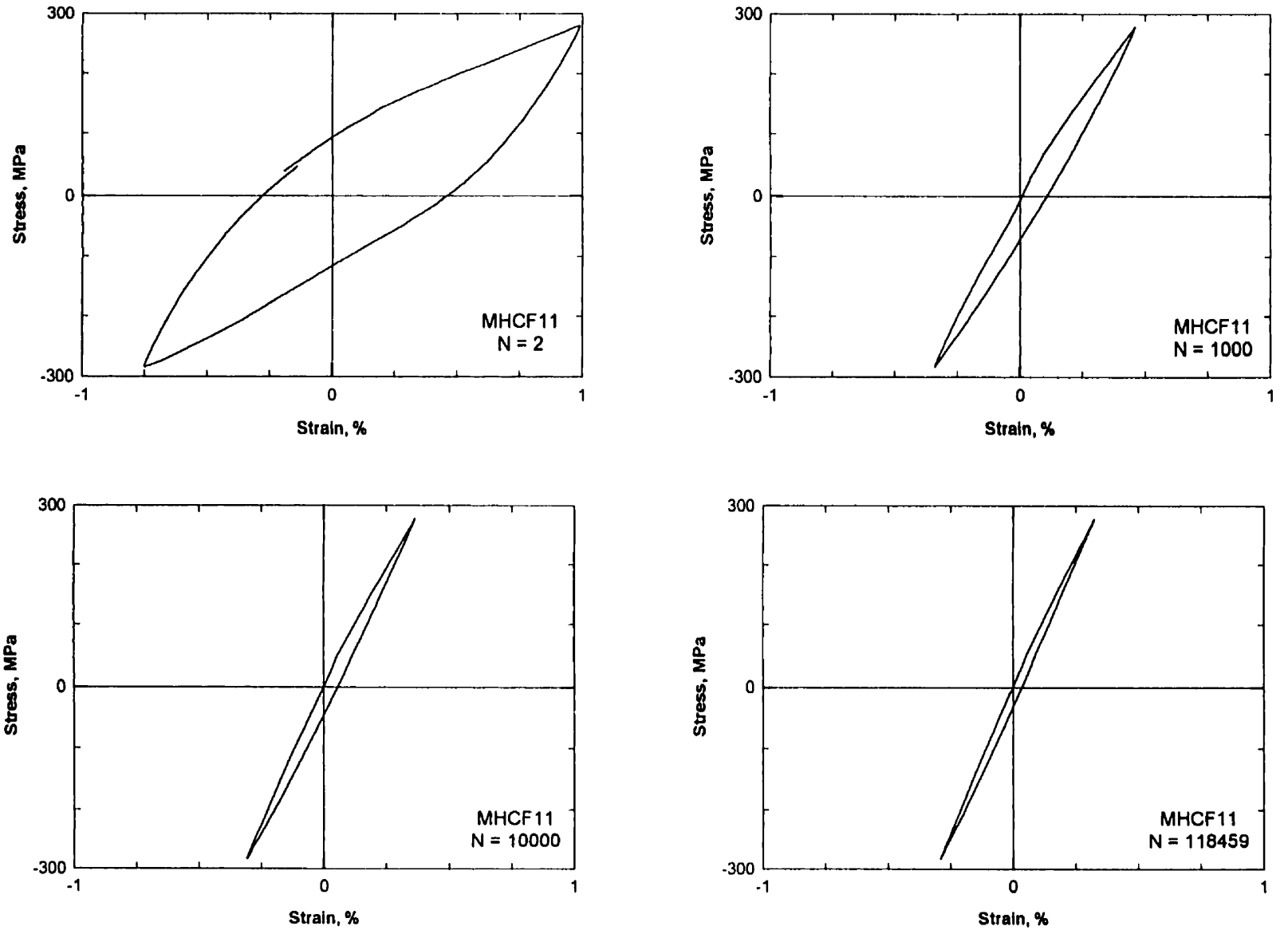

Figure C.9: Hysteresis curves for sample MHCF11 from the HCF experiments (Stress amplitude = 275 MPa)

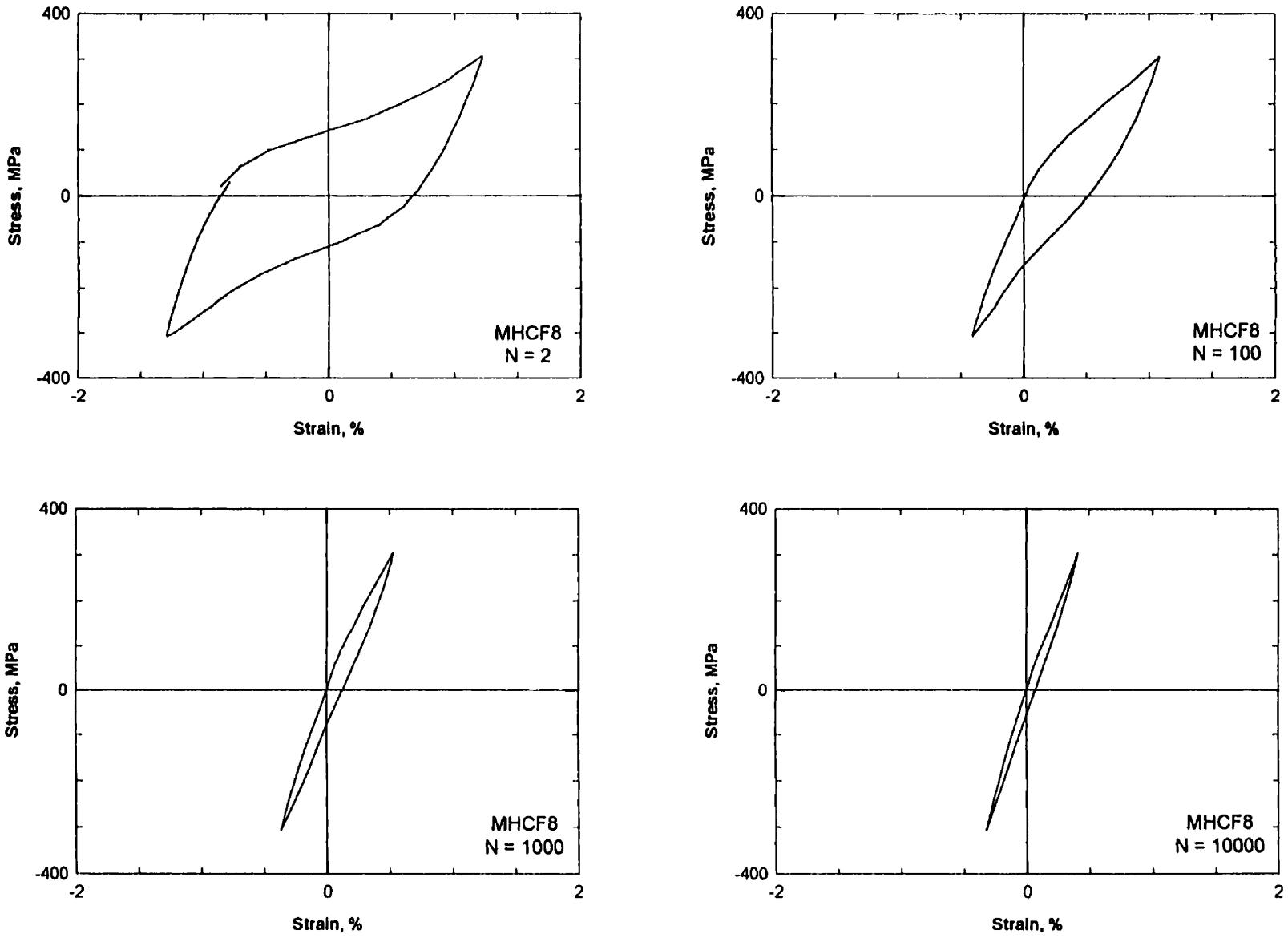

Figure C.10: Hysteresis curves for sample MHCF8 from the HCF experiments (Stress amplitude = 300 MPa)

APPENDIX D

MEASUREMENT OF DAMPING PROPERTIES

This appendix shows the calculation of the energy absorbed by Sample ALCF4 during one cycle of low-cycle fatigue loading. The hysteresis loop of sample ALCF4 at half life is shown in Figure D4.1. The hysteresis loop data points were divided into top and bottom halves as shown in Figures D4.2 and D4.3. Each of the halves were fitted with fourth order polynomials having the following equations:

$$y_t = -35.2x^4 + 138.7x^3 - 241.5x^2 + 394.3x + 288.7 \qquad \text{(D.1)}$$

$$y_b = 10.7x^4 + 85.3x^3 + 147.8x^2 + 447.3x - 148.9 \qquad \text{(D.2)}$$

where y represents the stress in MPa and x represents the strain in %.

The specific damping capacity, D, is equal to the area enclosed within the hysteresis loop. The area within the hysteresis loop is equal to the area enclosed by the top and bottom halves. Therefore the specific damping capacity was calculated as:

$$D = \int_{-1}^{1} y_t dx - \int_{-1}^{1} y_b dx \qquad \text{(D.3)}$$

where $\int_{-1}^{1} y_t dx$ is calculated as

$$\int_{-1}^{1} (-35.2x^4 + 138.7x^3 - 241.5x^2 + 394.3x + 288.7)\, dx = 403 \qquad \left(100 \times \frac{Nmm}{mm^3 cycle}\right)$$

$$= 4.03 \qquad \frac{Nmm}{mm^3 cycle}$$

and $\int_{-1}^{1} y_b dx$ is calculated as

$$\int_{-1}^{1} (10.7x^4 + 85.3x^3 + 147.8x^2 + 447.3x - 148.9)\,dx = -195 \qquad \left(100 \times \frac{Nmm}{mm^3 cycle}\right)$$

$$= -1.95 \qquad \frac{Nmm}{mm^3 cycle}$$

Because the curve fitting took place on a stress-strain plot with the stress having units of MPa and the strain having units of % strain the area calculated from such a plot has the units of $100 \times \frac{Nmm}{mm^3 cycle}$. The area under a hysteresis plot with stress in MPa and strain in $\frac{mm}{mm}$ will have the units $\frac{Nmm}{mm^3 cycle}$. Therefore, the specific damping capacity (or the energy absorbed per cycle) is:

$$D = 4.03 - (-1.95) = 5.98 \qquad \frac{Nmm}{mm^3}$$

The unit strain energy, U, is equal to the area between the mid stress curve and the strain axis, Figure D.4. The mid stress curve was fitted with a fourth order polynomial approximation as shown in Figure D.5. The equation of the polynomial is given below:

$$y_{mid} = -12.25x^4 + 112x^3 - 46.85x^2 + 420.79x + 69.87 \qquad \text{(D.4)}$$

Therefore, the unit strain energy is calculated as

$$U = \int_0^1 y_{mid}\,dx \qquad \text{(D.5)}$$

where $\int_0^1 y_{mid}\,dx$ is calculated as

$$\int_0^1 (-12.25x^4 + 112x^3 - 46.85x^2 + 420.79x + 69.87)\,dx = 291.3 \qquad \left(100 \times \frac{Nmm}{mm^3 cycle}\right)$$

$$= 2.91 \qquad \frac{Nmm}{mm^3 cycle}$$

The loss coefficient, η, is calculated using the values of D and U calculated above.

$$\eta = \frac{D}{2\pi U} = \frac{5.97}{2\pi(2.91)} = 0.326$$

In calculating the unit strain for the superelastic CuZnAl, the mid stress curve was calculated using the same approach used for the LCF samples.

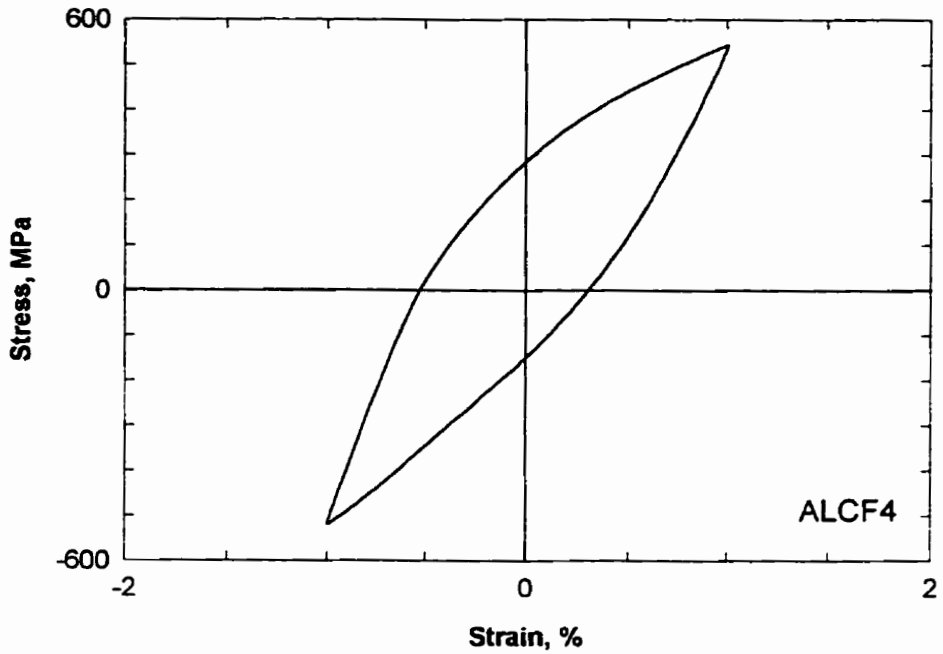

Figure D4.1: Hysteresis loop of sample ALCF4 at half-life

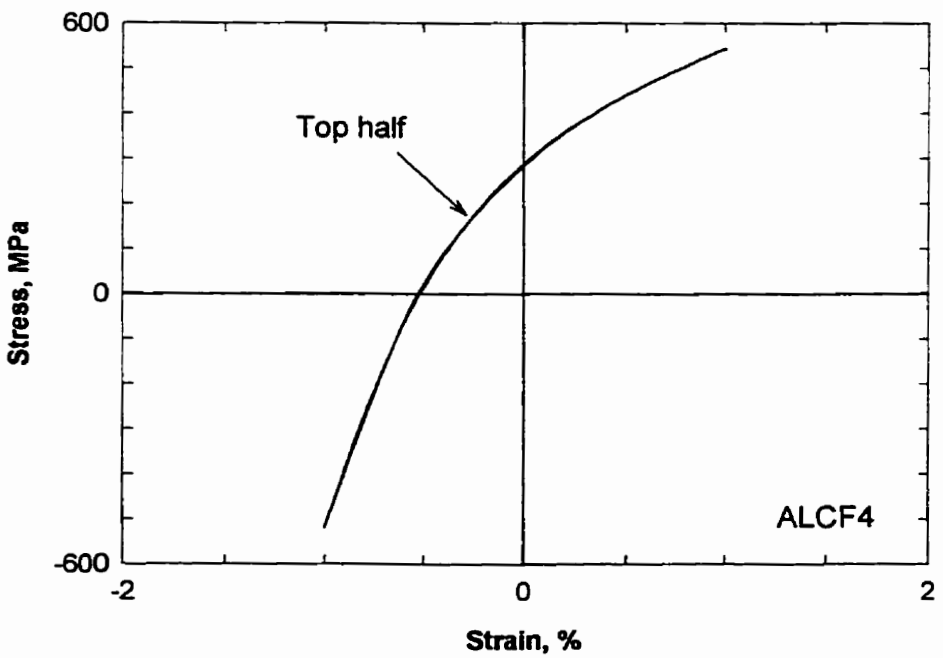

Figure D4.2: Figure showing the top half of the hysteresis loop shown in Figure D4.1 along with the polynomial approximation of the top half

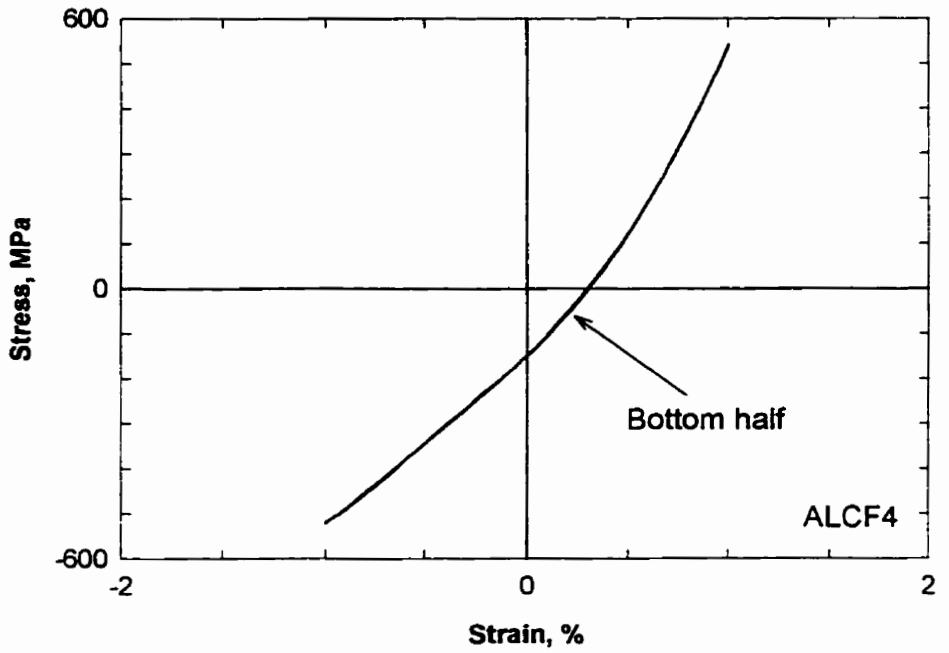

Figure D4.3: Figure showing the bottom half of the hysteresis loop shown in Figure D4.1 along with the polynomial approximation of the bottom half

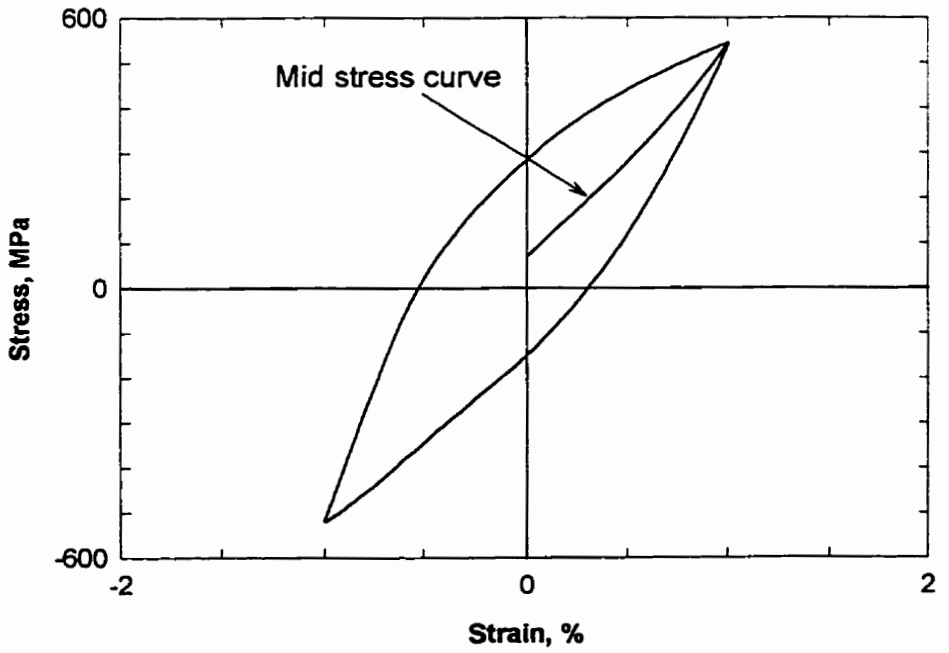

Figure D4.4: Mid stress curve compared to the hysteresis curve

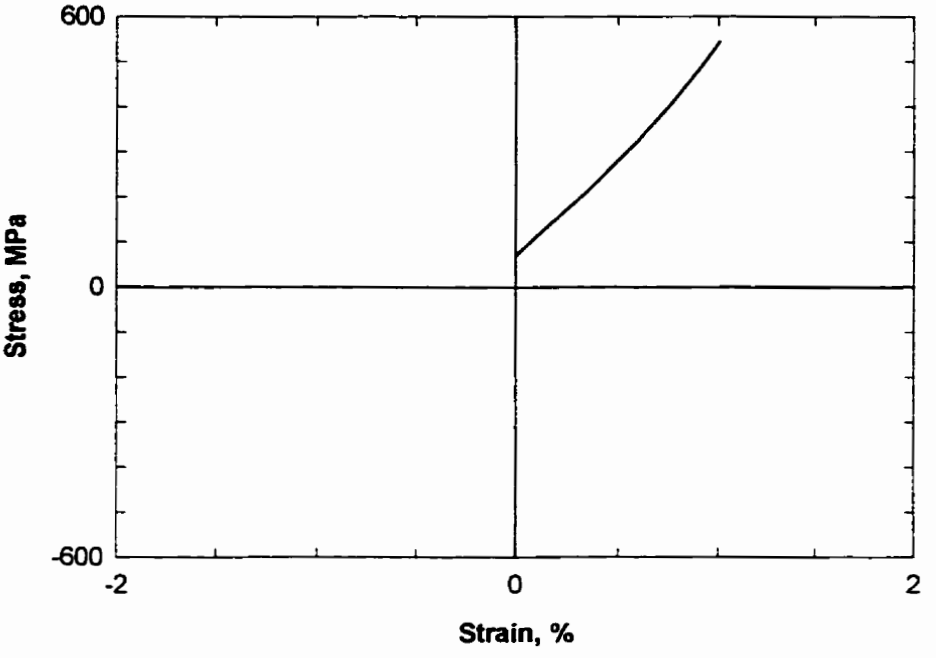

Figure D4.5: Mid stress curve and polynomial approximation

IMAGE EVALUATION
TEST TARGET (QA–3)

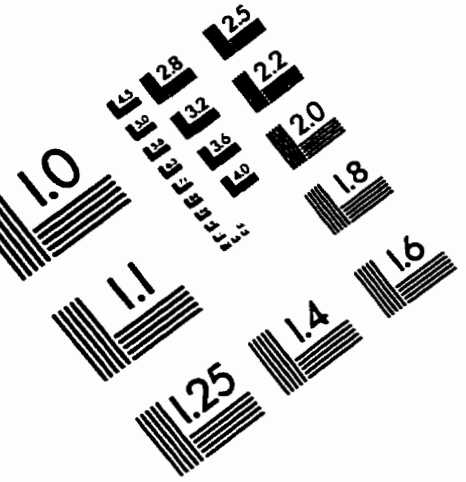

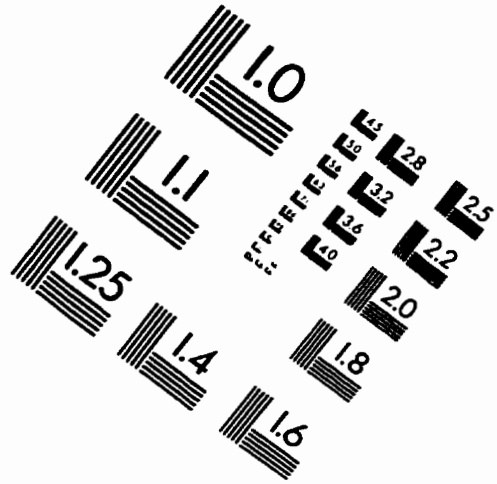

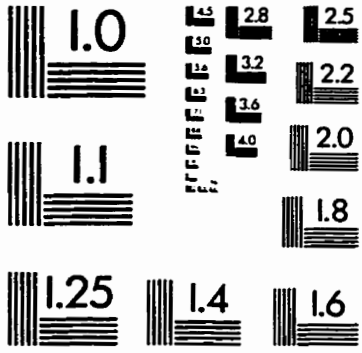

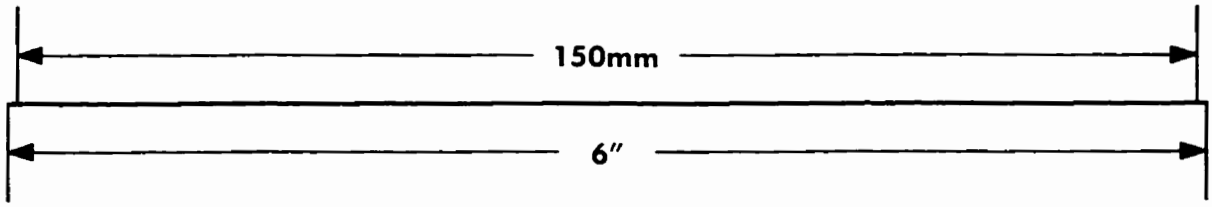

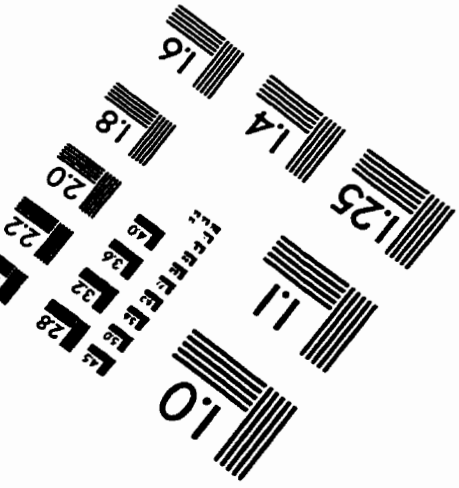

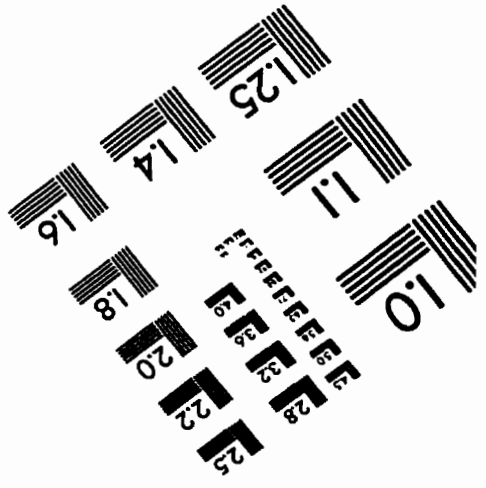

APPLIED IMAGE, Inc
1653 East Main Street
Rochester, NY 14609 USA
Phone: 716/482-0300
Fax: 716/288-5989